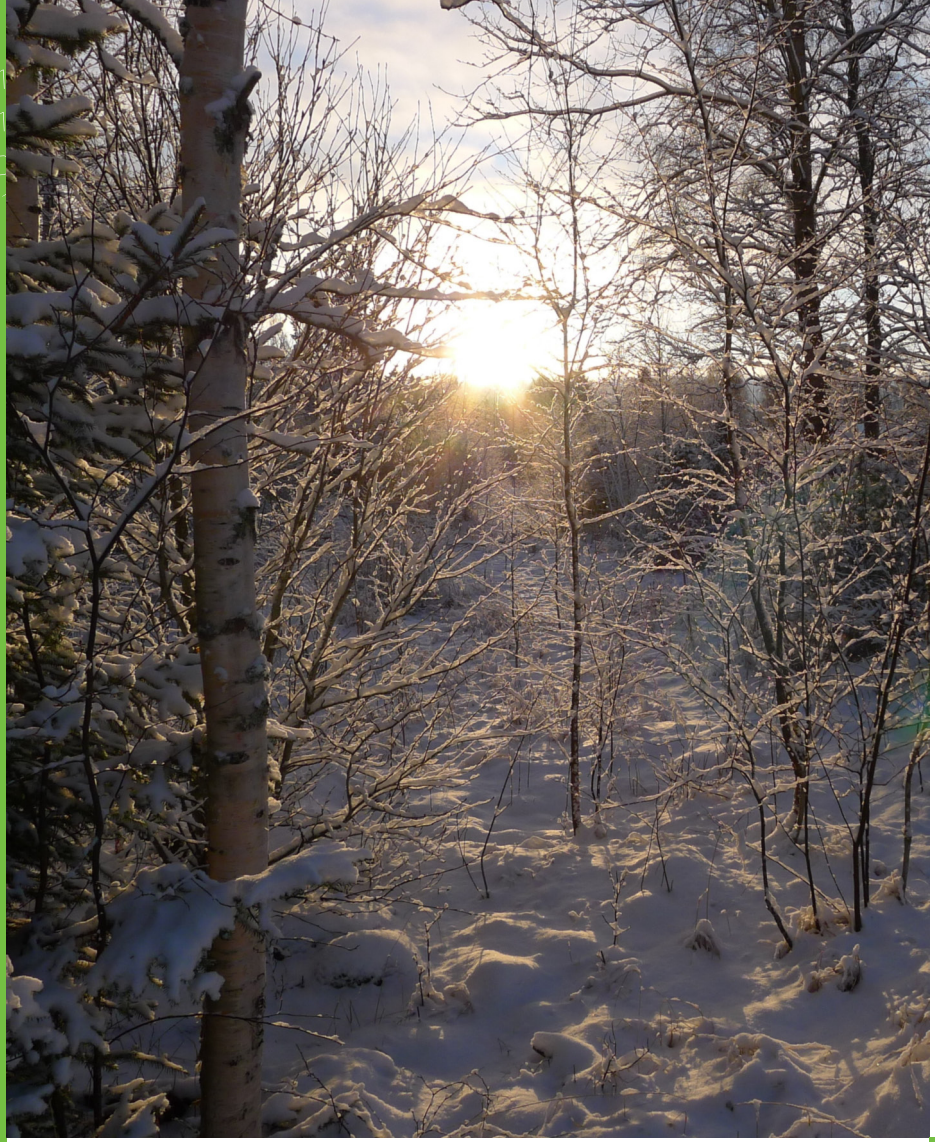

SCIENCE • TECHNOLOGY • RESEARCH HIGHLIGHTS • VISIONS •

Dissertation
112

Improved durability and reduced system complexity of solid oxide fuel cell systems

Olivier Thomann

VTT

VTT SCIENCE 112

Improved durability and reduced system complexity of solid oxide fuel cell systems

Olivier Thomann

A doctoral dissertation completed for the degree of Doctor of Science (Technology) to be defended, with the permission of the Aalto University School of Science, at a public examination held in the auditorium K213 at Aalto University on 09 December 2015 at 12 noon.

ISBN 978-951-38-8360-7 (Soft back ed.)
ISBN 978-951-38-8361-4 (URL: http://www.vttresearch.com/impact/publications)

VTT Science 112

ISSN-L 2242-119X
ISSN 2242-119X (Print)
ISSN 2242-1203 (Online)
http://urn.fi/URN:ISBN:978-951-38-8361-4

JULKAISIJA – UTGIVARE – PUBLISHER

Teknologian tutkimuskeskus VTT Oy
PL 1000 (Tekniikantie 4 A, Espoo)
02044 VTT
Puh. 020 722 111, faksi 020 722 7001

Teknologiska forskningscentralen VTT Ab
PB 1000 (Teknikvägen 4 A, Esbo)
FI-02044 VTT
Tfn +358 20 722 111, telefax +358 20 722 7001

VTT Technical Research Centre of Finland Ltd
P.O. Box 1000 (Tekniikantie 4 A, Espoo)
FI-02044 VTT, Finland
Tel. +358 20 722 111, fax +358 20 722 7001

Cover image: Olivier Thomann, 2012

Juvenes Print, Tampere 2015

Abstract

Solid oxide fuel cells (SOFCs) show great potential for clean and efficient power generation applications. However, their high cost is preventing their market entry. This dissertation focuses on solutions to increase the durability of SOFCs and to reduce the complexity of SOFC systems to drive their cost down.

Chromium poisoning of the cathode is a major issue limiting the durability of SOFCs. This issue is addressed by the development of a protective manganese-cobalt spinel coating for steel interconnects. Coated interconnects were characterised in SOFC relevant conditions and the results showed that the coating fulfilled its main requirements, which are: limitation of chromium transport from the interconnect to the cathode, protection against oxidation of the steel and low and stable area-specific resistance. Evidence was found that another source of chromium is the balance-of-plant (BoP) components upstream of the cathode, an issue which did not receive much attention in the literature. Therefore, a method for measuring chromium evaporation from BoP components was developed and validated on a stainless steel pipe.

SOFC systems based on natural gas commonly include a fuel processing subsystem for fuel steam reforming. The need for an external water source can be eliminating by recycling the steam-rich anode off-gas. Investigations were performed on a pre-reformer with a precious metal catalyst and it was found that adding an anode off-gas recycling loop had no detrimental effect on the activity of the catalyst and carbon formation could be avoided. Additionally, results showed the possibility to generate the hydrogen-containing gas needed to prevent the reoxidation of the anode catalyst during heat-up phase. The results permitted the implementation of an anode off-gas recycling loop in a 10 kW SOFC system. Additionally, the system was heated up without supplying any premixed hydrogen-containing gas, which enables to reduce the complexity of the system.

Finally, the durability of a stack can be improved by seal solutions with limited material interactions. A hybrid seal solution was developed by coating a compressible core with glass layers. The developed seal reduced the leak rate compared to a purely compressible seal. Material interactions were studied with a post-experimental investigation of an SOFC stack. Interactions were limited with the exception of evidence of increased oxidation at the steel/seal/air interface.

Overall, the solution was found to be promising and the obtained results led to the commercialisation of the developed seal solution by Flexitallic Ltd (UK) [1].

Keywords: Fuel cells, SOFC, chromium poisoning, anode off-gas recycling, system heat-up, seal, interconnect, material interactions

Preface

The work presented here has been carried out between 2010 and 2015 at VTT Technical Research Centre of Finland Ltd under the supervision of Professor Peter Lund from Aalto University. I would like to acknowledge financial support from VTT Technical Research Centre of Finland Ltd, the Fuel Cells and Hydrogen Joint Undertaking and Tekes – the Finnish Funding Agency for Innovation.

I am very thankful to my instructors, D. Sc Jari Kiviaho and D. Sc Olli Himanen. You have been of great support during this work and I enjoyed to have the opportunity to perform exciting research in a motivating environment. I am also grateful to Professor Peter Lund for the efficient supervision.

Additionally, I would like to thank D. Sc Markus Rautanen, D. Sc Matias Halinen, D. Sc Mikko Pihlatie, M. Sc Johan Tallgren, D. Sc Andreas Schuler, D. Sc Pekka Simell and M. Sc Risto Parikka. Our collaboration was absolutely essential to the realization of this work.

Additionally, I would like to express my gratitude to Kari Koskela, Juha Järvinen, Jorma Stick and Kai Nurminen. Without your practical, creative and efficient work, this work would have lasted decades. I thank also Kaija Luomanperä and Päivi Jokimies for the gas analysis.

The friends I made in Otaniemi were also of essential support to take my mind off my work when it was needed. Many thanks to Raphael, Florence, Michał, Emile and Melany.

I would like to thank Tuisku for her continuous support during the up and the down of this adventure. Lastly, a big thank for my family, particularly to my parents, Catherine and Matthias and to my grandparents, Leni and Hans, who were great support for my education and during my doctoral studies.

Espoo, August 2015

Olivier Thomann

Academic dissertation

Supervising professor	Professor Peter Lund Department of Applied Physics Aalto University School of Science Espoo, Finland
Thesis advisors	Doctor Jari Kiviaho Fuel Cells and Hydrogen Smart Industry and Energy Systems VTT Technical Research Centre of Finland Ltd Espoo, Finland
	Doctor Olli Himanen Fuel Cells and Hydrogen Smart Industry and Energy Systems VTT Technical Research Centre of Finland Ltd Espoo, Finland
Preliminary examiners	Professor Anke Hagen Department of Energy Conversion and Storage Technical University of Denmark Roskilde, Denmark
	Doctor Magali Reytier Hydrogen Production Laboratory French Alternative Energies and Atomic Energy Commision Grenoble, France
Opponent	Professor Massimo Santarelli DENERG -Dipartimento Energia Politecnico di Torino Torino, Italy

List of publications

This dissertation is based on the following original publications which are referred to in the text as Publications I–VI. The publications are reproduced with kind permission from the publishers.

I Thomann, O., Pihlatie, M., Rautanen, M., Himanen, O., Lagerbom, J., Mäkinen, M., Varis, T., Suhonen, T. & Kiviaho, J. Development and application of HVOF sprayed spinel protective coating for SOFC interconnects. Journal of Thermal Spray Technology 2013, Vol. 22, No. 5, pp. 631–639.

II Thomann, O., Pihlatie, M., Schuler, J.A., Himanen, O. & Kiviaho, J. Method for measuring chromium evaporation from SOFC balance-of-plant components. Electrochemical and Solid-State Letters 2012, Vol. 15, No. 3, pp. B35–B37.

III Halinen, M., Thomann, O. & Kiviaho, J. Effect of anode off-gas recycling on reforming of natural gas for solid oxide fuel cell systems. Fuel Cells 2012, Vol. 12, No. 5, pp. 754–760.

IV Halinen, M., Thomann, O. & Kiviaho, J. Experimental study of SOFC system heat-up without safety gases. International Journal of Hydrogen Energy 2014, Vol. 39, No. 1, pp. 552–561.

V Rautanen, M., Thomann, O., Himanen, O., Tallgren, J. & Kiviaho, J. Glass coated compressible solid oxide fuel cell seals. Journal of Power Sources 2014, Vol. 247, pp. 243–248.

VI Thomann, O., Rautanen, M., Himanen, O., Tallgren, J. & Kiviaho, J. Post-experimental analysis of a solid oxide fuel cell stack using hybrid seals. Journal of Power Sources 2015, Vol. 274, pp. 1009–1015.

Brief description of the content of the publications

Publication I: Protective coatings were applied on interconnect steel material by high velocity oxy-fuel spraying. The coated substrates were tested in long-term exposure tests to assess their high-temperature oxidation behaviour. Conductivity measurement showed that the coated substrate area-specific resistance was stable over time. Additionally, coated interconnect was used in a stack for 6000 hours and post-experimental analysis showed that the coating protected the interconnect from oxidation and exhibited adequate chromium retention.

Publication II: A method for measuring chromium evaporation from balance-of-plant components was developed. The volatile chromium was collected by air sampling through a denuder tube coated with sodium carbonate. Identification of the source of volatile chromium in an SOFC system is crucial for designing strategies to protect the cathode from chromium poisoning.

Publication III: The article focuses on the effect of anode off-gas recycling on the performance of a natural gas pre-reformer. Two scenarios were compared: one in which the pre-reformer was fed with a gas composition corresponding to the one found in an SOFC system equipped with an anode-off gas recirculation loop, and another corresponding to a system operated with steam-reformed natural gas. The reactor performance was higher using the anode-off gas recycling mode and carbon formation was not observed despite the use of conditions in which carbon formation is thermodynamically possible.

Publication IV: A heat-up strategy for an SOFC system was developed to eliminate the need for premixed protective gas cylinders. Firstly, the heat-up strategy was investigated in a pre-reformer test rig. It was found that oxygen inhibits reforming reactions at low temperatures and that this effect can be mitigated by the addition of hydrogen. The heat-up strategy was then successfully tested on a complete 10 kW SOFC system.

Publication V: Hybrid seals were developed by combining layers of compliant glass and Thermiculite 866 material. The hybrid seal combines the advantage of the compressible core material while the interfacial leak paths are blocked by the compliant glass layers. The hybrid seals exhibited very good performance even at compression stress as low as 0.1 MPa.

Publication VI: The article presents the findings of the post-experimental investigation of an SOFC stack. The stack included hybrid seals (compressive materials sandwiched between glass layers) and thin metallic interconnects (0.2 mm). The work included the investigation of the suitability of hybrid seals in an SOFC stack by measuring leak rate, analysing the ability of the seal to compensate for other component manufacturing tolerances, and material interactions between seals and interconnects. Overall, the hybrid seals used in combination with the thin interconnects were found to be effective solutions due to the low leak rate and limited material interactions.

Author’s contributions

For Publication I, the author actively took part in results discussions, data analysis and the writing. The author had the principal responsibility for performing the post-experimental analysis of the stack.

For Publication II, the author had the principal responsibility for the design, experiments, data analysis and writing.

For Publication III, the author contributed to results interpretation and participated actively in the writing.

For Publication IV, the author had the principal responsibility for the ex-situ pre-reformer part of the article and participated actively in the writing.

For Publication V, the author contributed to the ex-situ sealing experiments, to results discussions and participated in the writing.

For Publication VI, the author had the principal responsibility for post-experimental investigation, data analysis and writing.

Contents

List of abbreviations and symbols

Greek

ε_E	Voltage efficiency
ε_{FC}	Fuel cell efficiency
ε_{sys}	System fuel cell efficiency
ϵ_{th}	Thermodynamic efficiency
η_{act}	activation loss
η_{ohm}	ohmic loss
η_{conc}	concentration loss

Latin

ASR	Area-specific resistance
AOGR	Anode off-gas recycling
BoP	Balance-of-plant
BSE	Back-scattered electron
CTE	Coefficient of thermal expansion
DC	Direct current
E	Fuel cell operating voltage
$E°$	Reversible voltage at standard condition
E_{Nernst}	Nernst voltage
E_r	reversible voltage
EDS	Energy-dispersive X-ray spectroscopy
F	Faraday constant

G	Gibbs free energy
GHG	Greenhouse gas
GHSV	Gas hourly space velocity
HVOF	High velocity oxy-fuel
H	Enthalpy
I	Current
ICP-MS	Inductively coupled plasma mass spectrometry
LSM	Lanthanum manganite (La,Sr)MnO_3
LSC	(La,Sr)CoO_3
LSCF	(La,Sr)(Co,Fe)O_3
NG	Natural gas
NLPM	Normal litre per minute
NTP	Normal temperature and pressure
P_{AC}	Power supplied by the SOFC stack after conversion to AC
P_{aux}	Power demand of auxiliary devices
p_i	Partial pressure of gas
$\dot{Q}_{fuel}$	Fuel flow
$\dot{Q}_{H_2}^{cross}$	Hydrogen cross leak
$\dot{Q}_{Air}^{C,in}$	Cathode air inlet flow
R	Universal gas constant
RR	Recycling ratio
SEM	Scanning electron microscopy
SOFC	Solid oxide fuel cell
SR	Steam reforming
T	Temperature
t	Time
THT	Tetrahydrothiophene
V	Volume
$X_{H_2O}^{C,out}$	Steam molar fraction at the cathode outlet

YSZ	Yttria-stabilised zirconia
z	Electrons involved in the electrochemical reaction

1. Introduction

1.1 Background and motivation

The development of a sustainable energy system is one of the global challenges of our times. We need an energy system that fosters economic developments, while having a sustainable footprint on the environment. Emissions of pollution and resource consumption related to the energy sector have to be reduced to acceptable levels. Moreover, the human impact on climate change has been established [2] and significant efforts are being undertaken to curb greenhouse gas (GHG) emissions [3].

Technological developments can contribute to addressing the different challenges of our energy system. Public electricity and heat production accounted for 27% of GHG emissions in Europe in 2012 [4]. Electricity generation is presently dominated by fossil fuel-based generation, with about 50% of European electricity coming from fossil fuels in 2010 [5]). This sector is undergoing deep transformations because of the pressure to reduce the carbon-footprint of electricity, countries phasing out nuclear electricity or reducing its share, and tighter emission regulation on air pollution. Therefore, there is an important commercial potential for technologies that can contribute to increasing the electricity production efficiency and reducing its emissions in terms of pollution and GHG. Fuel cells are perceived to have an important role to play in the power generation in stationary, portable and transport applications due to their high electrical efficiency and very low emissions [6,7].

Fuel cells are electrochemical energy conversion devices that convert chemical energy from fuels directly into electricity and heat. Conversely to thermal power generation, fuel cells do not involve a combustion process. Fuel cells are modular in nature and can be scaled from a small generator (100 W) to an MW-class power plant, which makes them suitable for a wide range of applications. There are different types of fuel cells based on their electrolyte material. The fuel cells operating at the highest temperature are called Solid Oxide Fuel Cells (SOFCs) and operate between 600 and 900 °C. SOFCs have been the subject of intensive research and development because of their specific advantages.

SOFCs can achieve high efficiency even in small power units, with a demonstrated system electrical efficiency of 60% in units as small as 1–2 kW [8]. The

high operating temperature of SOFCs means that they can provide high quality heat for CHP applications. SOFCs have extremely low emissions. Because no combustion is taking place, nitrogen oxide and particulate matter emissions are insignificant. In addition, sulphur oxide emissions are extremely low because sulphur is a poison to SOFCs and is removed from the fuel feedstock before use. SOFCs also emit considerably less noise than combustion engines. The high temperature of operation of SOFCs enables a wide fuel flexibility and they can be designed to operate on hydrocarbon fuels, the infrastructures of which are already well developed. They are therefore a technology of choice for renewable fuels such as biogas, landfill gas, syngas from biomass gasification, biofuels and fuels produced from renewable electricity (power-to-gas route) [9-11] and thus they can additionally contribute to the reduction of GHG emissions and resource depletion.

Despites its advantages, the road to market has proven to be challenging for SOFCs. The main reasons hindering their market entry so far are their high cost, which is partly due to their insufficient durability and high system complexity. However, it should be noted that the market for SOFCs has seen a marked improvement in the last few years with 27 MW of shipped SOFC units worldwide in 2012 [12]. The market is presently driven by the demand for prime power for datacentres in the USA and CHP units in Japan and Europe.

Cost and lifetime targets of SOFCs depend on the specific application. For example, in their multi-annual implementation plan (2008–2013), the Fuel Cell and Hydrogen Joint Undertaking (FCH JU) specifies the SOFC technical targets for large commercial or industrial applications (300 kW – 5 MW) [13]. By 2015, the targets are 20,000 h lifetime at 55% electrical efficiency at a system cost of 4000 € kW^{-1}. By 2020, the targets are a lifetime of 40,000 h at 60% electrical efficiency with a system cost of 2000 € kW^{-1}.

1.2 Scope of the dissertation

The capital cost of an SOFC system is seen as key challenges preventing their market entry; it requires an improvement of their durability and a reduction of the system complexity to drive the overall cost down. The dissertation focuses on a selection of studies that address these challenges at the stack and system level.

One of these challenges is the prevention of cathode performance degradation. Several degradation phenomena can affect the durability of the cathode such as microstructural change, decomposition of the cathode material, chemical reaction with the electrolyte material, spallation of the cathode and chromium poisoning [14]. Despite numerous publications have been published on chromium poisoning, this topic was selected because some questions are still unanswered. It is established that volatile chromium species originating from stainless steel components can deposit on the cathode and degrade their performance over time, leading to insufficient SOFC lifetime. Most effort in research have targeted the development of protective coatings for metallic interconnect, however, the data about the dura-

bility of such coating in stack testing is limited. The publication I presents the results on the development of coating to reduce the transport of chromium from the stainless steel interconnect to the cathode and the coating evaluation in long-term stack test. Additionally, little is published about the transport of chromium from stainless steel balance-of-plant components to the cathode. Therefore, a quantification method was developed to assess the contribution of balance-of-plant components on the chromium intake of the cathode (Publication II).

Another challenge is to simplify the fuel processing subsystem. SOFCs running on natural gas have previously relied on steam reforming to generate a hydrogen-rich gas. The steam necessary for the steam reforming reaction can either be provided from an external source or from the electrochemical reaction in the SOFC itself. An external source of water requires a cleaned water inlet and an evaporator and it significantly increases the complexity of the system. One way of eliminating the cleaned water inlet during operation is to recirculate the steam-rich anode off-gas of the SOFC stack. This solution brings up new challenges for the activity of the reforming catalyst and increases the risk of carbon formation in the pre-reformer. This dissertation includes the results of an experimental study on the effect of anode off-gas recycling on the pre-reformer of an SOFC system (Publication III). Another simplification of the fuel processing subsystem is the elimination of the need for premixed protection gas during the heat-up. Traditionally, the premixed protection gas (4%-vol hydrogen in nitrogen) is used during SOFC heat-up to prevent the nickel of the anode from oxidising. This is a costly solution and increases the system size and maintenance need. Therefore, there is a motivation to generate in-situ the hydrogen-containing protective gas using natural gas and the system pre-reformer. This is addressed by Publication IV. This study presents the results on the generation of hydrogen with steam reforming on precious metal catalyst at temperatures as low as 200 °C. This result was used to develop a heat-up procedure that was used to heat up a 10 kW SOFC system.

The last challenge addressed in this work is the development of durable, low cost, highly conformable seals for an SOFC stack. Seals are needed to prevent mixing of the fuel and the oxidant in the SOFC stacks. Currently, seals are often made of ceramic glass that is brittle and prone to cracking upon thermal cycling. An alternative explored in the dissertation is the use of a composite structure of a mica-type of paper sandwiched between thin layers of glass. Such hybrid seals are not brittle in nature, limit the use of expensive sealing glass and allow larger manufacturing tolerance for SOFC components. The performance of such seals and the material compatibility with other stack components are investigated in Publications V and VI.

2. Solid Oxide Fuel Cells

2.1 Theory of operation

SOFCs produce electricity (and heat) from fuel and air via electrochemical reactions. They are based on cells constituted by gas-tight ionic-conductor ceramic electrolytes in contact with two electrically and ionically conductive electrodes. The operating principle of an SOFC is illustrated in Figure 1. The fuel (typically hydrogen-rich gas) is oxidised at the anode to form water and to release two electrons (Equation 1). The electrons are transported through an external circuit to the cathode. At the cathode, oxygen uptakes the electrons and is reduced to form oxygen ions (Equation 2). The oxygen ions are transported to the anode side through the electrolyte to react with the fuel by the overall reaction expressed in Equation 3.

$$H_2 + O^{2-} \leftrightarrow H_2O + 2\ e^- \quad (1)$$

$$1/2\ O_2 + 2\ e^- \leftrightarrow O^{2-} \quad (2)$$

$$H_2 + 1/2\ O_2 \leftrightarrow H_2O \quad (3)$$

In order to increase the delivered electrical power, cells are connected in series with electrically conductive interconnects to form a stack.

SOFCs do not require pure hydrogen as a fuel, as opposed to low-temperature fuel cells such as proton-exchange membrane fuel cells. Hydrocarbon fuels such as methane can be reformed inside the stack (as shown in Figure 1) or externally to form a gas mixture rich in hydrogen and carbon monoxide. Methane is reformed according to equation 4 in the anode of the SOFC, which typically includes nickel as a catalyst.

$$CH_4 + H_2O \leftrightarrow CO + 3\ H_2 \quad (4)$$

The carbon monoxide reacts further according to the water gas shift reaction (Equation 5) to form hydrogen and carbon monoxide. Therefore, carbon monoxide is not a poison to SOFC, but can be considered as a fuel.

$$CO + H_2O \leftrightarrow CO_2 + H_2 \quad (5)$$

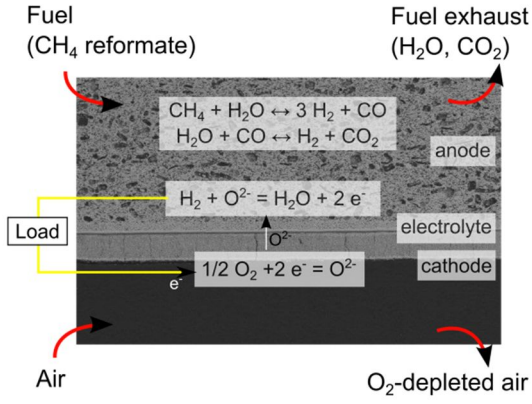

Figure 1. Elementary reaction steps in an SOFC.

2.2 Electrical efficiency of fuel cells

One of the advantages of fuel cells over a thermodynamic cycle engine is that they are not limited by the Carnot efficiency. The maximum achievable work from a chemical reaction is given by the change in Gibbs free energy ΔG. For the same reaction, the maximum amount of heat released (at constant pressure) is given by the change in enthalpy ΔH. Consequently, the maximum thermodynamic efficiency can be defined according to Equation 6.

$$\epsilon_{th} = \frac{\Delta G}{\Delta H} \quad (6)$$

The maximum thermodynamic efficiency therefore depends on the fuel considered. For example, at 700 °C, ϵ_{th} with hydrogen as a fuel is 82%, while for methane, the same value is 99%.

In practice, the maximum thermodynamic efficiency is not achieved because of different irreversibilities.

The theoretical reversible voltage E_r of a fuel cell is given by the available electrical work available, ΔG, divided by the charge transferred in the reaction according to:

$$E_r = \frac{-\Delta G}{zF} \quad (7)$$

where z is the number of electrons taking part in the reaction and F is the Faraday constant.

However, the actual cell voltage is always below the reversible voltage because of different irreversibilities. For example, the gas leakage through the seals or through the electrolyte leads to a voltage drop. Additionally, the electronic conduction of the electrolyte is non-zero and causes a short-circuit of the cell, which also decreases the cell voltage. If the partial pressures of the gas in the fuel cell are known, the Nernst equation can be used to calculate the voltage as a function of temperature and partial pressure of oxygen on the cathode and of the hydrogen and steam on the anode:

$$E_{Nernst} = E° + \frac{RT}{zF} \ln\left(\frac{p_{O_2}^{1/2} p_{H_2}}{p_{H_2O}}\right) \tag{8}$$

where $E°$ is the reversible voltage at standard condition, R is the gas constant, T the temperature and p_i is the partial pressure of the different gases.

In addition, the cell voltage is further decreased when current is drawn from the cell due to activation loss (η_{act}), ohmic loss (η_{ohm}) and concentration loss (η_{conc}). The activation loss corresponds to the overpotential required to overcome the activation energy of the electrochemical reaction. It is a measure of the catalyst effectiveness at a given temperature. The ohmic loss stems from the resistivity of the materials to the current and it is dominated by the ionic resistivity of the electrolyte. The concentration loss is present at high current density when the limitation of mass transport of reactants to the catalysts and the reaction products from the catalyst causes a voltage drop. Therefore, the cell voltage under load is:

$$E = E_{Nernst} - \eta_{act} - \eta_{ohm} - \eta_{conc} \tag{9}$$

One can thus define a voltage efficiency, ε_E, as the quotient of the actual cell voltage over the reversible voltage.

$$\varepsilon_E = \frac{E}{E_r} \tag{10}$$

In addition, not all the fuel is used in the fuel cell, therefore one can define the fuel utilisation, FU, defined as the quotient of the current drawn from the cell and the maximum current that a flow of fuel could deliver:

$$FU = \frac{I}{zF\dot{Q}_{fuel}} \tag{11}$$

where $\dot{Q}_{fuel}$is the flow of fuel. The fuel utilisation is typically between 70 and 90% in an SOFC.

The fuel cell efficiency, ε_{FC}, is obtained by multiplying the efficiency components (Equations 6 and 10) and the fuel utilisation (Equation 11):

$$\varepsilon_{FC} = \varepsilon_{th}\, \varepsilon_E\, FU = \frac{E\, I}{-\Delta H\, n_{fuel}} \tag{12}$$

which is the electric power produced in the cell divided by the chemical power of the fuel flow.

In fuel cell systems, auxiliary devices, such as the blowers, cause parasitic losses. In addition, the current cable and the direct to alternating current convertor cause additional losses. If we assume that the auxiliary devices use grid electricity, the fuel cell system efficiency, ε_{sys}, can be expressed as:

$$\varepsilon_{sys} = \frac{P_{AC}}{-\Delta H\, n_{fuel} + P_{aux}} \tag{13}$$

where P_{aux} is the power demand of auxiliary devices and P_{AC} corresponds to the alternating current power supplied by the fuel cell to the grid after conversion to alternating current.

Presently, the highest SOFC system efficiency reported in the literature is 60% from natural gas (lower heating value) to net export of alternating current electricity to the grid [8].

2.3 SOFC stack components

2.3.1 Electrolyte

The electrolyte needs to transport oxygen ions from the cathode to the anode, to be electronically insulating and to be dense to avoid the mixing of the fuel and the air atmosphere. It also needs to be stable in reducing and oxidising atmospheres and chemically and physically compatible with the electrode materials. The materials of choice are dense ceramic and the most commonly used is yttria-stabilised zirconia (YSZ) [15].

2.3.2 Anode

The anode needs to be catalytically active towards hydrogen oxidation, electrically conductive to direct the electrons to the interconnect, ionically conductive and its material should be stable in reducing conditions. Commonly, nickel is used in combination with YSZ in a porous cermet (a composite material of metal and ceramic). Nickel offers sufficient catalytic activity and is a good electrical conductor. In addition, it is also catalytically active towards steam reforming of methane, which is a significant advantage because it allows the use of methane as a fuel as explained in more detail in Section 2.4. The YSZ phase allows the transport of

oxygen ions towards the electrochemically active anode sites, at the triple-phase boundary between the nickel, the YSZ and the hydrogen-rich atmosphere [15].

2.3.3 Cathode

The requirements for the cathode are to be active for oxygen reduction, transport of the oxygen ions to the electrolyte and distribution of electric current associated with the cathode reaction. Perovskite materials such as doped-lanthanum manganite (La,Sr)MnO_3 (LSM) have been extensively used as cathode material. However, LSM is a largely electronic conductor, which restricts the reaction to the triple-phase boundary with the YSZ material. In order to increase the cathode active site, mixed ionic electronic conductor perovskites are also used as a cathode material, such as (La,Sr)CoO_3 (LSC) [16] and (La,Sr)(Co,Fe)O_3 (LSCF) [17].

A major issue with SOFC cathodes is the so-called chromium poisoning. Chromium evaporates from metallic interconnect and other steel balance-of-plant components and is transported to the cathode, where it deposits and degrades the cathode properties [18,19].

2.3.4 Interconnects

Interconnects have several functions in an SOFC stack. They collect electrons at electrodes and transport them to the neighbouring cells. In addition, they separate the fuel-rich atmosphere of the anode and the oxygen-rich atmosphere of the cathode. The simultaneous exposure to reducing and oxidising atmospheres at temperatures between 600 and 800 °C sets the high-temperature corrosion resistance requirement very high. Lastly the interconnects ensure the homogenous distribution of fuel and oxidants to the entire electrode surface [20-22].

The requirements of the interconnect materials are therefore:

i) High electrical conductivity
ii) High corrosion resistance
iii) Coefficient of thermal expansion matching with those of the other components of the cell and stack
iv) Suitable mechanical properties at elevated temperature
v) Low cost materials and manufacturing method.

For SOFCs operating at temperatures as high as 1000 °C, ceramic interconnects, such as doped-lanthanum chromite, are needed due to the challenging conditions [20]. Thanks to progress in SOFC manufacturing, there has been a general trend towards lowering the operating temperature of SOFCs to 600–800 °C, which allows the use of stainless steel as interconnect materials. Compared to ceramic interconnect material, stainless steels are generally more conductive, cheaper and easier to manufacture and shape. The high electrical conductivity requirement eliminates the alumina-forming stainless steels. The need for coefficient of thermal expansion (CTE) matching with the YSZ (about 10×10^{-6} $°C^{-1}$ from 25 to 1000 °C)

eliminates the austenitic stainless steels due to their higher CTE. Therefore, most of the research has focused on using ferritic stainless steels for interconnect applications [23]. Several commercial alloys were developed for this specific purpose, such as Crofer 22 APU (ThyssenKrupp VDM), E-Brite (Allegheny Ludlum), ZMG (Hitachi), or Sandvik Sanergy HT (Sandvik Materials Technology). They contain between 20–25% of chromium to meet the CTE and corrosion resistance requirements [24]. In order to further decrease the interconnect material cost, general purpose stainless steel alloys such as AISI 441 are being investigated in combination with corrosion protective coating [25-29].

2.3.5 Seals

The development of effective sealing solutions that address all the seal requirements is essential for improving the durability of SOFC stacks and reducing their cost [30,31]. Seals need to exhibit a low leak rate to decrease fuel loss (fuel leaking to air side and vice versa). Moreover, if the leak is localised, the air leaking to the anode side can cause local reoxidation of the nickel of the anode and can cause the cell to crack. Another issue with localised leakage is the formation of a hot spot, a local increase in the temperature due to the exothermal reaction of fuel and oxidant, which increases the degradation rate of the stack [32]. They need to withstand simultaneous exposure to the air side and to the fuel side at temperatures between 600 to 900 °C. Additionally, their performance should not be affected by hundreds to thousands of thermal cycles for stationary and mobile applications respectively. Moreover, they need to be chemically compatible with the adjacent components like the interconnects and cell materials over the lifetime of the SOFC stack. The seal material should be electrically insulating to avoid short-circuiting. Lastly, the seals should also be inexpensive, easy to assemble and compensate for the manufacturing tolerances of the other stack components.

Currently, glass ceramic seals are widely used in SOFC stacks. Their wet adjacent surfaces form a very gas-tight structure (e.g. 0.01 ml (min m)$^{-1}$ [33]) with few interfacial leakages. However, their main drawback is that the glasses are fragile and withstand tensile stress poorly, which makes them susceptible to failure when thermo-mechanical stresses are present, especially during thermal cycling. Additionally, the properties of glass or glass-ceramics (such as the coefficient of thermal expansion (CTE)), viscosity and porosity change over time, and these changes can create additional thermo-mechanical stresses during long-term operation and increase the risk of seal failure [31,34].

Compressive seals composed of mica-type paper have been investigated as an alternative [32,35,36]. Because compressive seal material exhibits some deformability and the seals are not rigidly bonded to the adjacent surface, they are more resistant to thermo-mechanical stresses. However, their leak rates are usually higher and are dominated by the interfacial leak paths, especially at low compression stresses [37,38].

2.4 Fuel processing for SOFC

SOFCs have a significant advantage over low-temperature fuel cells in the field of fuel flexibility. Because they operate at high temperatures, i.e. 600–900 °C, methane can be reformed on the nickel cermet anode, carbon monoxide does not poison the anode catalyst, and recoverable heat is available for steam reforming reaction [39-41]. Therefore, SOFCs can use a wide range of hydrocarbon fuels from renewable or fossil sources with a relatively simple fuel processing subsystem. They have been operated on biogas [42], natural gas [43], liquefied petroleum gas reformate [44], propane [45], methanol [46] and diesel reformate [47].

Hydrocarbon fuels are typically processed by steam reforming (SR) according to equation 14, by catalytic partial oxidation (Equation 15) or by oxidative-steam reforming, which uses a mixture of air and steam as a reforming agent. Steam reforming is a very endothermic reaction with a change of enthalpy $\Delta H°_r$ of +206 kJ mol^{-1} for methane, while catalytic partial oxidation is exothermic with $\Delta H°_r$ = -38 kJ mol^{-1} for methane [48].

$$C_nH_m + n\ H_2O \leftrightarrow n\ CO + (n + m/2)\ H_2 \quad (14)$$

$$C_nH_m + n/2\ O_2 \leftrightarrow n\ CO + m/2\ H_2 \quad (15)$$

Natural gas is currently widely used as a fuel for SOFCs due to the availability of its infrastructure and low requirements for fuel processing. Its exact composition depends on its source but the main compounds are methane and light hydrocarbon like ethane and propane. A typical natural gas composition from the grids of the United States, Australia, Denmark and Finland are listed in Table 1.

Table 1. Natural gas composition from various national grids.

	Main components				
Natural gas grid from	CH_4	C_2H_6	C_3H_8	CO_2	N_2
USA [49]	87–97	1.5–7	0.1–1.5	0.1–1	0.2–5.5
Australia [8]	91.0	5.0	0.5	2.4	1.0
Danmark [50]	89.1	6.0	2.4	1.0	0.3
Finland [51]	97.9	0.9	0.3	0.0	0.8

Typically, the natural gas is partially reformed before the stack in a pre-reformer. On the one hand, it is beneficial to maintain some internal reforming inside the stack because the endothermic steam reforming reaction cools down the stack, which reduces the need for stack cooling with excess cathode air and the parasitic loss associated with the air blower. On the other hand, a high degree of internal reforming causes a large temperature gradient and thermal stress at the anode

inlet and is detrimental to the durability of the stack [52]. Additionally, there is a risk of carbon formation at the anode at high degrees of internal reforming and this risk increases with higher hydrocarbon fraction [53,54]. In order to decrease the degree of internal reforming, a natural gas-fuelled SOFC system typically includes a pre-reformer upstream of the stack. In the pre-reformer, the fuel is converted to syngas (methane, carbon monoxide and dioxide, hydrogen and steam). The degree of conversion depends on the steam-to-carbon ratio and the pre-reformer temperature.

2.5 SOFC system layout: an example

The scope of this section is not to provide an exhaustive introduction to SOFC systems, but rather to present a specific layout. This specific layout is relevant to the present work because the experiments of Publications III and IV were designed to produce results applicable to this system. The SOFC system is illustrated in Figure 2 and consists of the stack module and the BoP components module. A detailed description of this system and its performance can be found in [43]. The system uses an anode off-gas recycling (AOGR) loop, which enables operation without an external water supply when sufficient steam is produced in the stack. The natural gas is fed to the system and mixed with the recycled anode exhaust gas before being heated up in the fuel heat exchanger. The fuel is then partially reformed in the pre-reformer and fed to the stack. The stack fuel outlet gas is used to heat up the inlet fuel and then a fraction of the fuel is recycled by the AOGR blower. An important parameter is then the recycling ratio (RR), which corresponds to the fraction of the flow of recycled gas over the total flow of anode off-gas. The rest of the fuel exhaust gas is fed to a catalytic burner, where the unreacted fuel fraction is burned with the exhaust air. The heat produced in the catalytic burner is used to heat up the inlet air. The inlet air is fed to the system by an air blower and heated up in the air heat exchanger before being fed to the stack. Additionally, two by-pass valves are used to control the temperature of the stack and the burner. In addition, two electric heaters are used during start-up, one before the stack inlet inside the stack module and another one before the AOGR blower. The system is designed to be thermally self-sustained during operation.

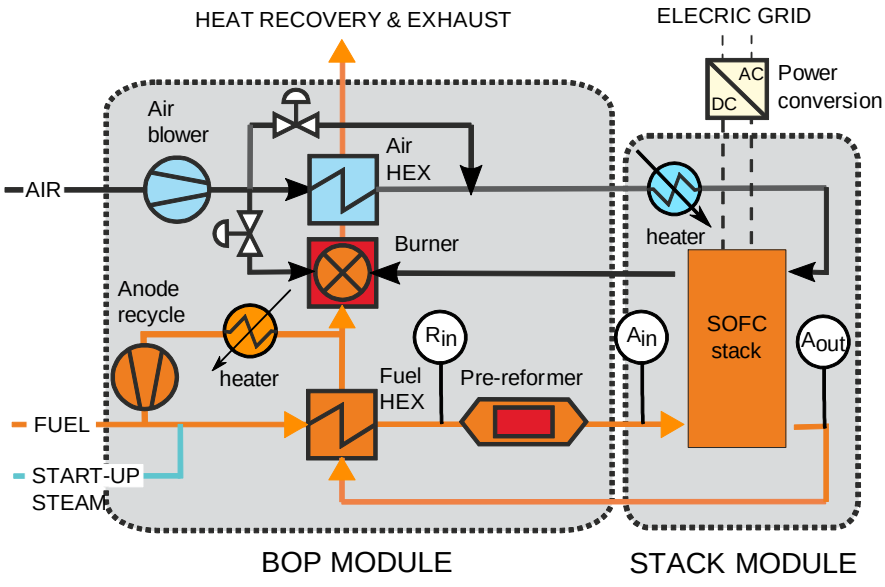

Figure 2. VTT 10 kW demo unit layout with fuel system gas sampling locations. Reproduced and adapted from Ref. [43]. Copyright 2011, The Electrochemical Society.

As mentioned, not all the fuel is used in the stack and this is described by the stack fuel utilisation parameter (FU_{stack}) (Equation 11). As discussed in Section 2.2, it is beneficial to have high fuel utilisation for electrical efficiency. However, there is an optimal value for the stack fuel utilisation because concentration voltage loss becomes important at high fuel utilisation. Moreover, if all the fuel is used in the stack, the nickel of the anode starts to oxidise from the stack outlet, which is highly detrimental to the cell integrity. In a system equipped with an AOGR loop, part of the unused fuel is recycled, which means that the system fuel utilisation (FU_{sys}) becomes higher than the stack utilisation. System fuel utilisation can be calculated from the stack fuel utilisation with Equation 16 [55].

$$FU_{sys} = \frac{FU_{stack}}{1 - RR + RR \cdot FU_{stack}} \quad (16)$$

For example, the VTT 10 kW demo unit operates at about 80% system fuel utilisation, while the stack fuel utilisation is kept at about 60% in nominal conditions.

3. Prevention of chromium poisoning

3.1 Protective coating for metallic interconnects (Publication I)

3.1.1 Background

Ferritic stainless steels are widely used as interconnect materials because they offer an advantageous balance between the fulfilment of their different requirements such as good electrical conductivity, matching of CTE with cell materials and the low cost associated with the material and manufacturing methods [56]. However, the thermally grown oxide layer is mainly composed of chromium oxide and is a source of volatile chromium species, which have been found to deposit on the cathode and cause the so-called chromium poisoning. Chromium poisoning decreases the performance of the cathode over time, which reduce the durability of SOFC [19,57,57-62]. Some ferritic stainless steel alloys were specifically designed for SOFC operation such as Crofer 22 APU (ThyssenKrupp VDM), E-Brite (Allegheny Ludlum, or ZMG (Hitachi) and they form an outer chromium-manganese spinel layer with a lower area-specific resistance (ASR) and a lower chromium evaporation rate (up to 75% reduction of evaporation rate) [58]. However, the reduction of chromium evaporation brought about by optimised steel composition is seen as insufficient and a protective coating is necessary to further reduce the chromium evaporation rate and thus improve the durability of SOFCs [23].

In order to reduce chromium evaporation and oxidation of stainless steel, protective coatings need to have no porosity or closed porosity and low diffusivity of oxygen and chromium through the coating. Moreover, the addition of a coating should not decrease the performance of the SOFC and therefore a coating needs to have a low and stable ASR and good chemical, physical and structural compatibility with the adjacent components.

A wide range of protective coatings have been reported in the literature [23] and among them $(Mn, Co)_3O_4$ has received attention for its good performance [63-66]. Numerous methods have been used to deposit such coatings like slurry spraying [67,68], radio-frequency sputtering [68], magnetron sputtering [69,70], plasma spraying [71], atomic layer deposition [72], pulsed laser deposition [73], electrodeposition [74], and filtered arc [75]. In addition, $MnCO_{2-x}Fe_xO_4$ spinel coating has been tested for its better electrical conductivity [65,66].

The goal of the work reported in Publication I was to assess the performance of $MnCo_2O_4$ and $MnCo_{1.8}Fe_{0.2}O_4$ spinel coatings on Crofer 22 APU steel by high velocity oxy-fuel (HVOF) spraying. Thermal spraying was chosen because it produces coatings that are already very dense and additional sintering is not necessary because the coating is formed by molten or semi-molten droplets. Among thermal spraying method, HVOF spraying was selected because it produces coating with a high tensile bond strength [76]. For this purpose, high-temperature oxidation behaviour and ASR of the coated steel samples were investigated. Additionally, a post-experimental analysis was performed on a single-cell stack using a coated interconnect that was operated for 6000 h. The post-experimental analysis focussed on the evaluation of the coating microstructure, the oxidation of the interconnect, and the transport of chromium. To the authors' knowledge, $(Mn,Co)_3O_4$ and $MnCo_{2-x}Fe_xO_4$ spinel coatings deposited by HVOF spraying for SOFC interconnects have not been previously reported in scientific journals.

3.1.2 Experimental

Coated Crofer 22 APU test coupons were prepared to evaluate their high temperature oxidation behaviour and to measure their ASR over time. Commercial Crofer 22 APU steel (ThyssenKrupp VDM) with a thickness of 0.2 mm was used as a substrate for test coupons. The coupons were coated by HVOF spraying with a Praxair HV2000 spray gun fitted with a combustion chamber. Nitrogen was used as powder carrier, hydrogen as fuel and air as oxidant.

The high-temperature behaviour was investigated in exposure tests with 10 x 10–15 x 0.2 mm coated coupons. The samples were coated on both sides and only the edges were uncoated. The test was conducted in humidified air (3% vol. steam) for 1000 h at 700 °C. Cross-sections were prepared from the sample for scanning electron microscopy (SEM) observation.

The ASR of the coated interconnect needs to be low and stable over time. For this reason, the ASR was measured for 1000 h at 700 °C in a test arrangement illustrated in Figure 3. The test samples consisted of two coatings ($MnCo_{1.8}Fe_{0.2}O_4$ and $MnCo_2O_4$) deposited on two 26 x 26 x 0.2 mm steel coupons separated by a ceramic spacer mimicking a cathode. In addition, an uncoated steel plate was tested as a reference. Green $La_{0.85}Sr_{0.15}Mn_{1.1}O_3$ (LSM) spacers (20 x 20 x 1 mm, IRD Fuel Cells A/S, Denmark) were used as separation material in order to serve as a contact surface with a material similar to an SOFC cathode. Therefore, the investigated contact resistance interface was coated steel against LSM. Several samples were stacked up and a vertical load of 20 N was applied to the samples. Steel plates of 1 mm thickness were used as separator disks between each substrate-coating system. All samples were connected in a single direct current (DC) loop with a current density of 0.2 A cm^{-2}. The samples were slowly heated up in flowing air to burn off the binder from the green LSM spacers, until 850 °C. The samples were held at 850 °C for 12 hours to sinter the LSM spacer. The steady-state measurements were conducted at 700 °C in dry air. The ASR reported corresponds to half of the ASR measured for one substrate-coating system. The use

of an LSM spacer in the system mimics the contact interface between the coated interconnect and the cathode. However, in a real stack, the sintering of the cathode is performed before stack assembly, whereas the LSM spacers were sintered with the coated substrates in the ASR set-up.

The $MnCo_{1.8}Fe_{0.2}O_4$ coating was tested in a single-cell stack for 6000 h at 700 °C. The interconnects were made of Crofer 22 APU plate with a thickness of 1 mm and the gas channels were etched into the plates. The protective coating was sprayed on the cathode interconnect and was about 20 µm in thickness in its as-sprayed condition. The coated interconnect was not heat-treated prior to use and no contact coating was used. An anode-supported cell with an (La, Sr)(Co,Fe)O_3 (LSCF) cathode was used. Dry hydrogen and dry air were used as fuel and oxidant. The current density was 0.3 A cm^{-2}.

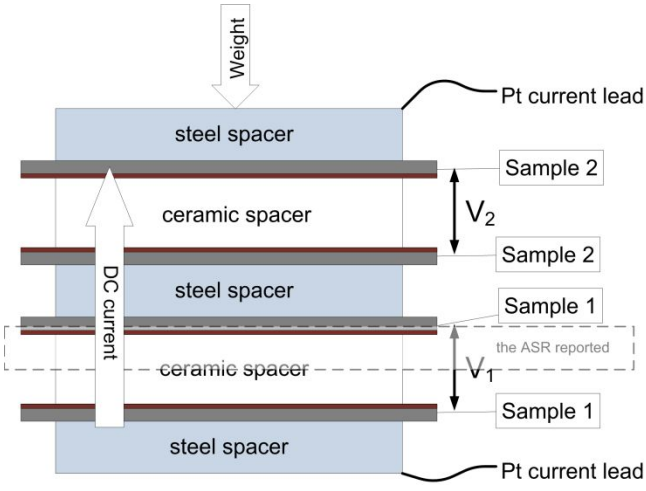

Figure 3. The ASR measurement arrangement for coated Crofer 22 APU coupons with LSM spacers. The protective coatings were applied on the Crofer 22 APU steel surfaces facing the ceramic spacers.

3.1.3 Results and discussion

A typical microstructure of an $MnCo_2O_4$ as-sprayed coating made by HVOF is presented in Figure 4. The coating exhibits an adequate density. Some alumina particles are visible at the steel-coating interface from the steel grit blasting procedure. The coatings were subjected to exposure to air at 700 °C for 1000 h. Figure 5 illustrates a cross-section of an exposed steel coupon with an $MnCo_{1.8}Fe_{0.2}O_4$ coating of about 17 µm in thickness. The microstructure of the coating is shown in Figure 5 (a) and (b) and an elemental profile from an energy-dispersive X-ray spectroscopy (EDS) line scan is presented in Figure 5 (c). The thermally grown chromium oxide layer between the steel and the coating is about 0.5 µm in thickness. During high-temperature exposure, the coating sintered and lost its lamellar

structure. Some closed porosity remains visible after 1000 h of exposure with a decreasing porosity towards the surface. The elemental profile shows that there is little or no chromium gradient in the coating, which suggests that the diffusion of chromium is effectively hindered. As a reference, a non-coated Crofer 22 APU sample exposed to the same condition exhibited a thermally grown chromium oxide layer of about 2.5 µm in thickness, which is five times higher than the coated sample. Therefore, the coating solution effectively reduces the oxidation of the steel interconnect.

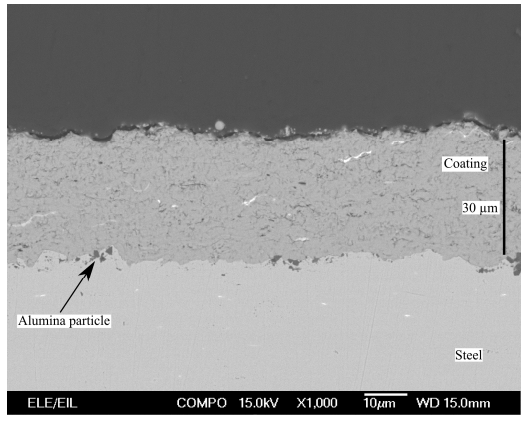

Figure 4. A SEM-BSE image of an as-sprayed HVOF $MnCo_2O_4$ coating on a Crofer 22 APU substrate.

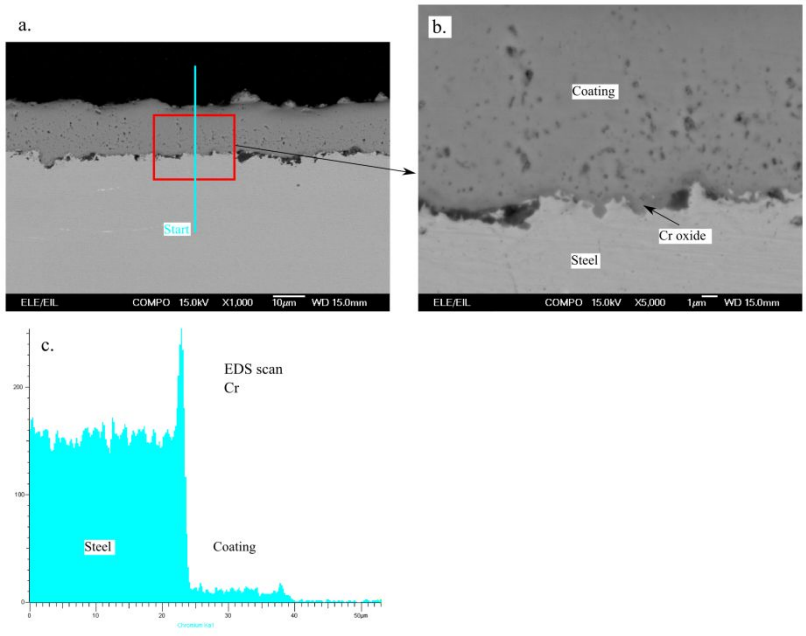

Figure 5 (a and b). SEM-BSE images of an HVOF $MnCo_{1.8}Fe_{0.2}O_4$ coating on a Crofer 22 APU substrate exposed to air at 700 °C for 1000 h at different magnification. c. Measured chromium EDS profile.

The ASR measurements versus time for coated and uncoated stainless steel coupons are presented in Figure 6. The ASR values included the contribution of different components, which are the steel substrate, the chromium oxide scale developing on the steel surface, the protective coating, the contact resistance of the interface between the coating and the ceramic cathode material, and the resistance of the ceramic cathode material (i.e. 500 µm of LSM). A few step changes in the ASR took place at 220 and 720 h and are associated with either structural instability or small unintentional changes in the test temperature (10 °C) due to a power failure. The ASRs of the $MnCo_{1.8}Fe_{0.2}O_4$ (17 µm thick) and the $MnCo_2O_4$ (20-28 µm thick) coatings were initially between 20 and 30 $m\Omega cm^2$ and stabilised at about 20 $m\Omega cm^2$ after a few hundred hours. The ASRs then remained stable until the end of the test after 1000 h. These results suggest that the electrical properties of the coated stainless steel samples do not degrade when exposed to air at high temperatures. It is difficult to compare ASR results between different studies because the experimental parameters, such as measurement temperature, test duration, gas atmosphere, contact material and the spacer used vary widely throughout the literature. However, the ASR results reported here are in

line with results obtained for $MnCo_2O_4$ spinel coatings deposited by a slurry-coating technique [77] or using a similar test arrangement including cathode material spacers [68,78].

The ASR of the uncoated Crofer 22 APU in contact with the LSM spacer was initially about 100 $m\Omega cm^2$ and decreased during the tested period to reach 45 $m\Omega cm^2$ after 1000 h. The observed decrease in ASR over time is attributed to the formation of a conductive $(Cr, Mn)_3O_4$ spinel layer on top of the oxide layer, which improves the electrical contact between steel and LSM. This behaviour was previously observed by Yang et al. [68,79]. In principle, the observed decrease in ASR could also be attributed to possible sintering of the green LSM spacer and consequent increasing of its bulk conductivity, however this initial improvement was not observed for the coated samples that were also using green LSM spacers. The ASR of both coated samples was initially smaller than the uncoated Crofer 22 APU, which is counterintuitive because the coating is expected to have some resistance. Therefore, it is believed that the initial difference originates from a lower contact resistance of the coated samples.

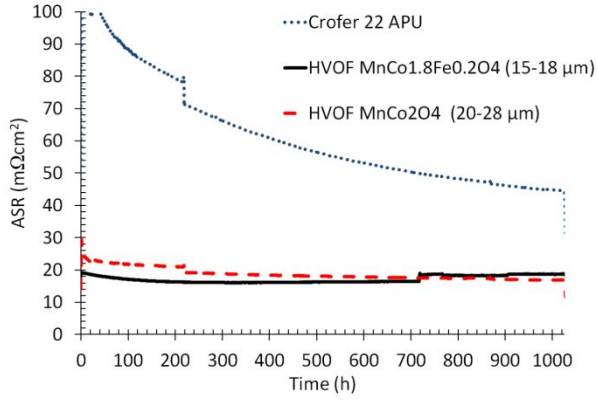

Figure 6. Measured ASR in a 4-point DC measurement of Crofer 22 APU coupons, coated and uncoated, all in contact with an LSM spacer. The coatings are $MnCo_{1.8}Fe_{0.2}O_4$ and $MnCo_2O_4$.

Finally, a post-experimental analysis was performed on a single-cell stack that used a coated interconnect. The aim of the post-experimental analysis was to assess the performance of the coating in terms of interconnect oxidation and retention of chromium. Four back-scattered electron (BSE) SEM cross-sections of the single-cell stack are illustrated in Figure 7. Figure 7 (a) presents a low-magnification view of the cathode side where the air channel and the contact location between the cathode and the coated interconnect are visible. The coating

covers the interconnect completely, including geometrically challenging features like the edges of the interconnect ribs.

Figure 7 (b) shows the contact location between the cathode and the interconnect coated with $MnCo_{1.8}Fe_{0.2}O_4$. The chromium oxide scale is about 1 µm in thickness after 6000 h at 700 °C in air. Figure 7 (c) shows the coated interconnect at an air channel location. The chromium oxide scale below the coating is also about 1 µm in thickness. These results can be compared with the exposure tests presented above where the chromium oxide layer of the coated steel was about 0.5 µm in thickness and the oxide layer of the uncoated steel was about 2.5–3 µm after 1000 h in air at 700 °C. Therefore, the coating solution appears to effectively reduce the oxidation of the interconnect in a long-term test in an SOFC environment. The elemental composition of the coatings at both locations was analysed by EDS but no chromium could be detected (detection limit is about 0.3%-at), which indicates that the diffusion of chromium is effectively hindered by the coating. The chromium content of the cathode was also investigated and no chromium could be detected in the cathode at the interconnect contact location (Figure 7 (b)). Figure 7 (d) illustrates the cathode at an air channel location and an EDS chromium concentration profile across the cathode. The EDS analysis reveals that chromium was present in the cathode at this air channel location. Chromium distribution is inhomogeneous and peaks at 2.1%-at. The chromium source for this contamination can either be the stainless steel interconnect, coming through the protective coating, or the uncoated Crofer 22 APU air manifold and Inconel 600 air inlet pipe upstream of the stack. However, chromium contamination was only found at the air channel location (Figure 7 (d)) and not at the contact location with the interconnect (Figure 7 (b)), which supports the hypothesis that the chromium has originated from the uncoated air manifold and inlet pipe. Additionally, the EDS analysis showed that no chromium could be detected in the coating, suggesting that negligible chromium diffusion appears to take place across the coating. Stainless steel components and manifold upstream of the cells have been previously identified as chromium contamination sources [80] and the work presented in Publication II also shows that BoP components can be a significant source of volatile chromium [81].

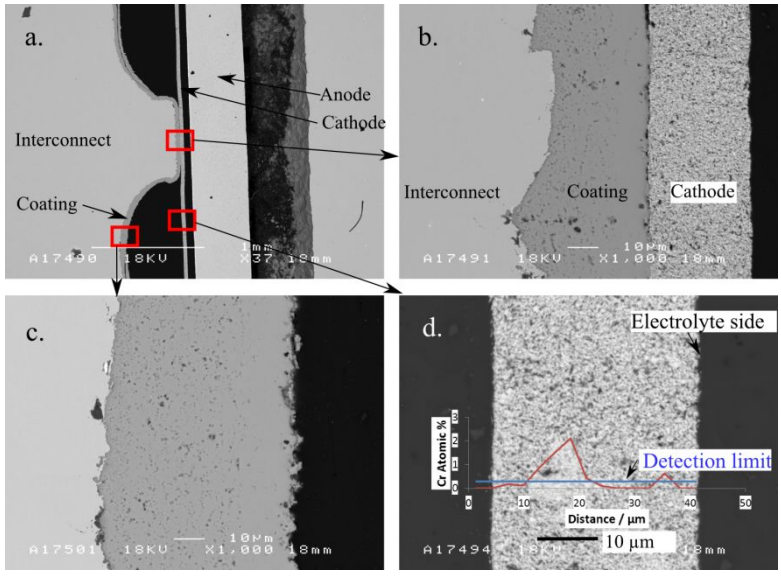

Figure 7. SEM-BSE cross-section from the single-cell stack at different locations. (a) Low-magnification image of the air side of the single-cell stack. The interconnect coating composition is $MnCo_{1.8}Fe_{0.2}O_4$. (b) The contact area between coated interconnect and cathode. (c) Surface of the interconnect at an air channel location. (d) Cathode with an EDS chromium profile.

3.2 Method for measuring chromium evaporation (Publication II)

3.2.1 Background

As discussed in Section 3.1, chromium poisoning of cathode is seen as one of the major issues with respect to the durability of SOFCs. A large amount of literature has been dedicated to the development of solutions to reduce the transport of chromium from stainless steel interconnect materials to the cathode. Section 3.1 presented such a solution in the form of a protective coating applied by HVOF spraying. However, metallic interconnects are not the only possible source of chromium in an SOFC system. Commonly, the high-temperature BoP components, such as piping and heat exchangers, are made of austenitic stainless steels for their better mechanical and corrosion properties and are thus also a potential source of volatile chromium species [58]. The chromium volatile species can then be transported from the BoP component upstream of the stack to deposit on the cathode as proposed in [82,83]. Due to the relative complex geometry of BoP

components, most of the coating techniques developed for interconnects are not applicable to BoP components. An assessment of chromium evaporation rates from BoP components is therefore seen as a prerequisite for the development of solutions to reduce this effect and the evaluation of improvements brought about by such solutions. These include material selection [84], surface treatment such as aluminising [85,86], coatings or chromium trapping [87]. Publication II aims to contribute to this challenge by presenting a dedicated measurement technique.

Several methods to quantify chromium evaporation have been reported in the literature and were reviewed in [88]. They all rely on the evaluation of small metal coupons [58,89,90]. These methods are well adapted to comparing different samples. However, it is difficult to calculate from their results the actual amount of chromium coming from a real complex-shaped component (uneven temperature and flow profile and large surface area), as the evaporation rate depends on several factors like the flow rate, flow regime and local temperature. This work focuses on the development of a method for measuring chromium evaporation directly from the hot gas stream of a BoP component. The chromium collection is carried out by using a coated denuder tube, a technique previously used by Froitzheim et al. [89].

3.2.2 Experimental

The schematic drawing of the experimental set-up is illustrated in Figure 8. An austenitic stainless steel pipe was evaluated as a simple BoP component. However, the method could be used on a more complex component, e.g. a heat exchanger. The 1.2 m long pipe was of grade 253MA (Sandvik) and its composition is given in Table 2. It was exposed to a high temperature in a furnace. Humidified air (1.8 vol-% humidity) was fed into the pipe at a rate of 10 l_N min^{-1}. A quartz denuder tube (inner diameter 5.2 mm and length 500 mm) was inserted into the steel pipe near its end. A fraction of the flow (from 15 to 35% of the main flow) was sampled through this denuder tube by a diaphragm pump and a rotameter. The inner wall of the denuder tube was dip-coated with sodium carbonate from a surfactant-containing solution. In the presence of humidity, the dominant species in air is chromium oxyhydroxide which is formed according to equation (17) [91].

$$Cr_2O_3(s) + 2\,H_2O(g) + 3/2\,O_2(g) \leftrightarrow 2\,CrO_2(OH)_2(g) \qquad (17)$$

The chromium oxyhydroxide reacts with the sodium carbonate coating according to the equation (18). According to HSC [92], the equilibrium constant of this reaction is above 10^{10} from room temperature to 800 °C.

$$CrO_2(OH)_2(g) + Na_2CO_3(s) \leftrightarrow Na_2CrO_4(s) + H_2O(g) + CO_2(g) \qquad (18)$$

Each measurement lasted 24 hours, after which the coated denuder tube was replaced without cooling down the furnace, which is very time-efficient to perform

repeated experiments. The chromium-containing coating was dissolved in 10% nitric acid, diluted to obtain a suitable chromium concentration for inductively coupled plasma mass spectrometry (ICP-MS, Thermo Scientific ELEMENT 2). The effect of temperature of the stainless steel pipe on the chromium evaporation rate was investigated by triplicated measurements that were carried out at 650, 700 and 750 °C.

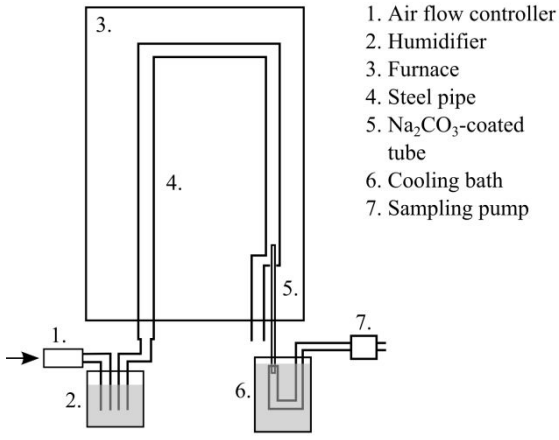

Figure 8. Schematic drawing of the experimental set-up.

The effect of the heat treatment history of the stainless steel pipe was investigated by measuring the chromium evaporation rate at 750 °C before and after a heat treatment at 800 °C for 100 hours. SEM and EDS were used to investigate the correlation between the change of evaporation rates and microstructure of stainless steel oxide layers.

Table 2. Nominal chemical composition of 253MA in %-weight [93].

C	Si	Mn	P	S	Cr	Ni	N	Ce
0.08	1.6	≤0.8	≤0.04	≤0.03	21	11	0.17	0.05

3.2.3 Results and discussion

3.2.3.1 Measurement uncertainty

It was verified that the coated denuder tube was sufficiently long for chromium collection by assessing that most of the chromium collected (70.7 +/- 17.2%) reacted in the first third of the tube. Actually only 7.3 +/- 1.8% of the total amount of chromium collected reacted in the last third of the tube. Sodium carbonate coated denuder tube can reach very high collection efficiency, for example, Froitzheim et al. used a similar set-up to measure chromium evaporation from steel coupons and they demonstrated a collection efficiency of 95% [89].

Measurement error on the chromium concentration in air was calculated to be 6% based on the errors of the individual measurement devices (flow meter, timer, volume measurement, pipette, collection efficiency). The random error was 13%, which corresponds to two times the standard deviation to have a confidence level of 95% assuming a normal distribution of the measurement values. Therefore, the overall uncertainty is thus 14%.

3.2.3.2 Effect of temperature on chromium evaporation

The Figure 9 illustrates the results from chromium evaporation measurements at 650, 700 and 750 °C in triplicates. The measured values are compared to value calculated from thermodynamic data, assuming that the equilibrium pressure is reached in the pipe. The three thermodynamics datasets are generated from three different experimental studies and they were obtained from Stanislowski et al. [58]. The experimental results of chromium evaporation obtained with the method presented here are coherent with the thermodynamic data found in the literature. In addition, the good repeatability of the method is demonstrated by the low standard deviation.

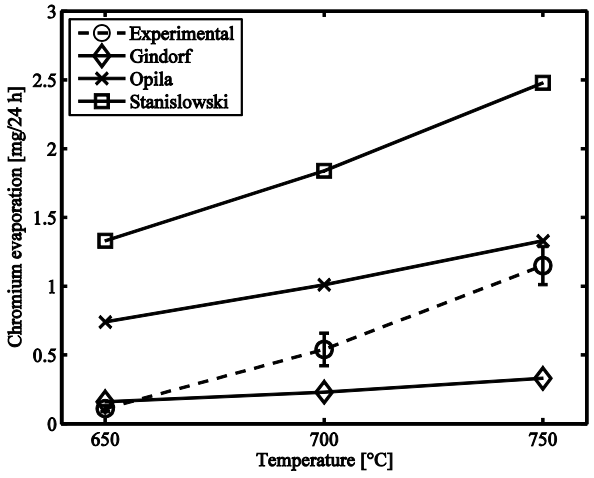

Figure 9. Measured amounts and standard deviations of evaporated Chromium at different temperatures. The experimental data are compared with calculations based on thermodynamics data from different sources (data extracted from [58]).

3.2.3.3 Effect of heat treatment history on chromium evaporation

It was found that the temperature history has a significant effect on the amount of chromium evaporation at 750 °C. A heat treatment of the pipe for 100 h at 800 °C resulted in a reduction by a factor of four in the volatile chromium concentration in the air exiting the pipe at 750 °C (from 8.0×10^{-8} to 2.0×10^{-8} kg m^{-3}). To investigate the reason behind the decrease in chromium evaporation, the oxide layer on top of the stainless steel was investigated by SEM cross-section and EDS elemental mapping before and after the heat treatment. For this purpose, one pipe was exposed at 750 °C for about 300 h. Another pipe was exposed in a same way, except that it was subsequently exposed to 800 °C for 100 h before repeating the chromium evaporation measurements at 750 °C.

Figure 10 (a) and (b) present SEM micrographs of cross-sections of the inner surface of the stainless steel pipe before and after the exposure at 800 °C. Before exposure at 800 °C, a thin oxide layer of about 1 µm is present on the steel surface (Figure 10 (a)) and the oxide layer is chromium-rich (Figure 10 (c)). After exposure at 800 °C, the oxide layer was found to be about 10 µm thick (Figure 10 (b)) and its oxide layer is not homogenous in composition. The inner layer is chromium-rich and the top layer is depleted in chromium (Figure 10 (d)), but rich in iron oxide.

The reduction of chromium evaporation is explained by a thicker oxide layer, which is depleted from chromium at its surface. Enrichment in iron of the stainless steel oxide layer is associated with high oxidation rate because iron oxide is not as

protective as chromium oxide. Thus this is not beneficial for SOFC applications despite the associated reduction in chromium evaporation.

Although the reason for the formation of such an oxide layer is not ascertained, this result is presented here to illustrate the ability of the developed measurement method to notice an unexpected oxide layer growth through change in chromium evaporation rate. Alloy 253MA, the alloy of the pipe, is designed to withstand higher temperature and therefore this corrosion behaviour is unexpected.

The method presented here was used to quantify the chromium concentration at the outlet of a stainless steel pipe and it proved to be an effective tool because of its repeatability and the coherence of its results with thermodynamic data. In addition, it was sensitive enough to detect a heat treatment induced decrease in evaporation rate caused by an oxide scale growth. The method therefore fulfils its purpose and can be used to measure chromium evaporation from BoP component such as heat exchanger. The results presented here also confirm that stainless steel BoP components can contribute to the chromium intake of the stack, since the air exiting the investigated pipe was saturated with volatile chromium species.

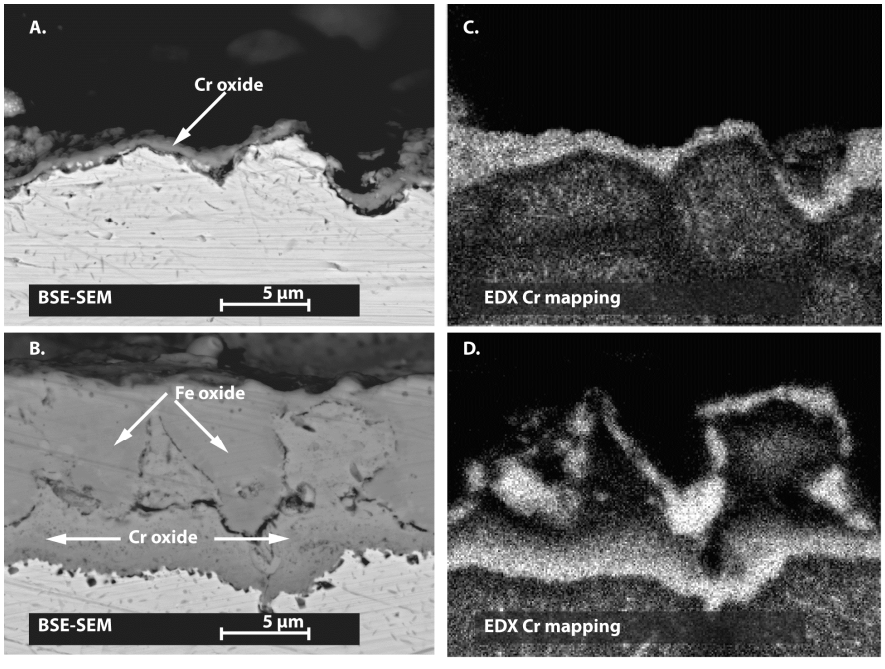

Figure 10 (a) and (b). SEM-BSE cross-section of the stainless steel before and after the 800 °C heat treatment. (c) and (d) EDX chromium mapping of the corresponding views.

4. Fuel processing subsystem

4.1 Effect of Anode off-gas Recycling on the pre-reformer (Publication III)

4.1.1 Background

The present chapter presents a study (Publication III) aiming at implementing an anode off-gas recycling loop in an SOFC system. An SOFC system that operates on steam-reformed fuel relies on a continuous supply of steam. It is technically simple to provide the steam from an external water supply with a deionisation system and an evaporator. However, this approach has significant drawbacks: the water source, the deionisation system and evaporator increase the system complexity and its maintenance requirements. Alternatively, the steam produced by the electrochemical reaction on the anode side (Equation 1) can be recycled back to the fuel inlet. It can be realised by recycling a fraction of the SOFC anode off-gas back to the fuel inlet. Thus, the need for an external water source is made unnecessary at least during operation [94]. Another significant advantage of recycling the anode off-gas is to increase the system efficiency. Because not all the fuel is utilised when it passes through the SOFC stack, recycling a part of this unreacted fuel allows to decrease accordingly the fuel inlet feed, which can improve the electrical efficiency of the system [95,96]. Lastly, the stack fuel utilisation can be decreased when an AOGR loop is used, which has been shown to be beneficial for the stack durability [97].

In practise, the implementation of a hot AOGR loop (i.e. without steam condensation) has proven challenging. AOGR can be implemented by a recycling blower or by an ejector, but suitable components cannot be found off-the-shelf at the moment [95]. Another issue is the risk of carbon formation which can occur if not enough steam is recycled, i.e. if the recycling ratio is too low [98]. Moreover, the risk of carbon formation increases when higher hydrocarbons than methane are present in the fuel [54]. It is possible to predict the gas composition, temperature and possibility for carbon formation using thermodynamic equilibrium calculation. However, actual carbon formation eventually depends on the activity of the reforming catalyst. Therefore, experimental investigation of the catalyst and pre-reformer is needed to map the safe operating region without carbon formation. Lastly, there is little experimental data reported in the literature on the effect of AOGR on cata-

lyst activity. Peters et al. reported that AOGR caused a decrease of the activity of a nickel-based catalyst [99], conversely Nummela et al. reported that AOGR had no negative effect on the performance of another pre-reformer nickel catalyst [100].

As already mentioned, the recycling ratio should be sufficient to have carbon-free operation. However, it should not be too high either, because it means larger parasitic electrical loss associated with the AOGR blower. In addition, AOGR results in a dilution of the fuel at the anode, which decreases the cell voltage [96]. Therefore, the recycling ratio should be optimised to have carbon-free operation and minimise the parasitic loss and the voltage drop.

This study aimed at generating the necessary results to build a pre-reformer for a 10 kW SOFC system including an AOGR loop [43]. This work contributes to the field of fuel processing in SOFC system by assessing experimentally the effect of AOGR on the performance of a precious metal-based pre-reformer using natural gas as a fuel. The performance of the pre-reformer in AOGR conditions is compared against SR conditions. Additionally, the effect of varying the recycling ratio is evaluated to determine its effect on the performance and to identify the minimum recycling ratio that can be used safely in an SOFC system, i.e. corresponding to carbon formation-free operation. The effect of the degree of reforming in the pre-reformer on the thermal management of the stack is out of the scope of this work. The temperature of the stack can be manage either by adjusting the degree of reforming of the pre-reformer or by adjusting the air flow and its temperature to the cathode. Results of this work led to the successful implementation of an anode off-gas recycling loop in a 10 kW SOFC demonstration unit, where the system is operated at nominal conditions without external water supply [43].

4.1.2 Experimental

The effect of AOGR on a precious metal catalyst-based pre-reformer was investigated in a natural gas pre-reformer test bench. As illustrated in Figure 11, the test bench consisted of the gas and deionised water mass flow controllers (EL-FLOW and LIQUI-FLOW, Bronkhorst), a water evaporator and mixer (CEM-303, Bronkhorst), a superheater (in-house built), a pre-reformer containing a commercially available precious metal catalyst monolith (Süd-Chemie), micro-quartz particle filters (MK 360, Munktell, designed to collect particles above 0.3 µm of diameter) and a heat exchanger (Alpha-Laval) to condensate the water from the exhaust gas. The temperature of the process gas was measured after the evaporator (TI1 in Figure 11), at the reactor inlet (TI2), at the catalyst monolith leading surface (TI3), at the centre of the monolith (TI4), at the trailing edge of the monolith (TI5), at the pre-reformer outlet (TI6), and after the filter (TI7). The process gas pressure was measured before the evaporator (PI1), at the pre-reformer inlet (PI2) and outlet (PI3) and after the filter (PI4). The dried pre-reformer exhaust gas was analysed by an online gas analyser (Sick S710 series) and with gas chromatographs (Agilent 6890 N, Agilent 6850 and HP 5890 Series II).

The heat used in the reforming reaction was supplied by heating the inlet gas in the superheater and the pre-reformer was used in a condition close to adiabatic, which means that heat loss was minimised by thermal insulation and electric heaters.

Depending on the pre-reformer temperature and gas composition, carbon formation can take place in the pre-reformer. The detection of its formation is based on pressure measurements. The carbon can accumulate on the catalyst surface and eventually cause a measureable increase of pressure at the pre-reformer inlet. Alternatively, the carbon formed in the pre-reformer can be carried downstream by the gas flow and is then collected at the filter, causing a measureable pressure increase before the filter. Additionally, when the pre-reformer was kept for an extended time in a defined condition, the set-up was flushed with nitrogen and air and the CO and CO_2 fractions at the set-up outlet were monitored to detect oxidation of possible carbon deposits.

The recycling gas compositions were synthesised using gas cylinders of carbon monoxide, carbon dioxide and hydrogen, in addition to deionised water (Millipore Elix system) and natural gas from the grid. The natural gas in the Finnish grid contains mainly methane (ca. 98%) with a small fraction of ethane, propane and nitrogen as listed in Table 1. The natural gas was desulphurised before the set-up with sulphur adsorbent (Süd-Chemie) because it contains 4–10 ppm of tetrahydrothiophene (THT) as an odorant.

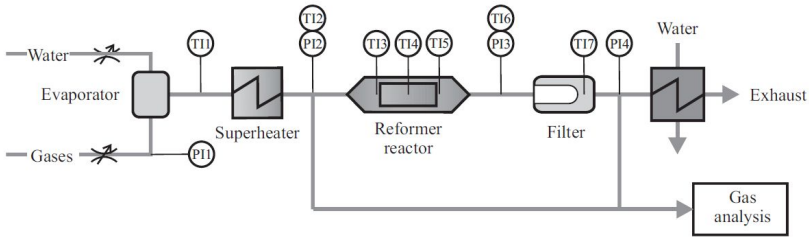

Figure 11. Schematic layout of the test equipment.

In order to assess the effect of an AOGR loop in an SOFC system on the pre-reformer, the pre-reformer was operated in two different modes. Firstly it was operated in steam reforming mode, in other words, only natural gas and steam were supplied to the pre-reformer. Secondly, natural gas was fed to the pre-reformer in addition to the simulated anode off-gas containing steam, carbon monoxide, carbon dioxide and hydrogen. This second mode is referred further as AOGR mode. In both cases, the pre-reformer inlet temperature was kept at 600 °C. The different experimental conditions are listed in Table 3. In steam reforming mode, the steam-to-carbon ratio (H_2O/C) was varied between 1.5 and 2.5. In AOGR mode, the recycling ratio varied between 0.2 and 0.7. The outlet gas of a correctly designed pre-reformer should be at thermodynamic equilibrium. There-

fore, the measured outlet gas temperatures and compositions are compared to the calculated equilibrium values to assess the performance of the pre-reformer.

The gas compositions given in Table 3 have been calculated on the basis of equilibrated gas with an in-house developed code [96]. Because this study aimed to generate the necessary results to build a pre-reformer for a defined SOFC system [43], the boundary conditions were predefined. In the calculations, the stack outlet temperature (700 °C), the stack fuel utilisation (0.6) and the current density were kept constant. Based on the heat exchanger layout (see Figure 2), the pre-reformer inlet temperature was expected to be about 600 °C in nominal conditions.

An important parameter for the pre-reformer operation is the gas hourly space velocity (GHSV), which is calculated by dividing the gas volume flow ($Nm^3\ h^{-1}$) at normal temperature and pressure (NTP) by the catalyst volume (m^3). On the one hand, it is advantageous to operate the pre-reformer at as high a GHSV as possible, since it minimises the pre-reformer size, the amount of expensive catalyst material and the pressure drop at the pre-reformer. On the other hand, the GHSV should be limited to a value at which the gas reaches thermodynamic equilibrium at the pre-reformer outlet. A GHSV value of about 20,000 h^{-1} at recycling ratio of 0.5 was selected as a reference condition in this study. The GHSV was chosen based on previous experience with this catalyst and the recycling ratio is based on the results of an electrical efficiency optimisation study. The GHSV corresponding to the different experimental conditions is plotted as a function of the recycling ratio in Figure 12 (left). It can be noted that the GHSV increases with the recycling ratio, which means that the residence time of the gas in the pre-reformer becomes shorter. Additionally, the natural gas inlet flow rate is also plotted as a function of the recycling ratio in Figure 12 (right) and it can be seen that the natural gas flow rate decreases when the recycling ratio is increased, illustrating how much fuel can be saved by increasing the recycling ratio.

Table 3. Experimental conditions in SR and AOGR modes.

	H_2O/C	Recycling ratio	GHSV (h^{-1})	NG	CO	CO_2	H_2	H_2O	Methane conversion (%)
	2.5	–	21 900	28.6	0	0	0	71.4	17
SR	2	–	18 800	33.3	0	0	0	66.7	15
	1.5	–	15 700	40	0	0	0	60	13
		0.2	10 200	56.7	5.5	8.8	14.1	14.8	5
		0.28	12 100	46	6.4	11.6	16.5	19.5	5
		0.36	14 500	37.1	6.9	14	17.9	24	6
		0.4	15 800	33.3	6.8	15.3	18.1	26.4	7
AOGR		0.5	20 000	25	6.7	18.3	17.9	32.2	9
		0.55	22 700	21.5	6.4	19.8	17.4	35	11
		0.6	26 100	18.2	6	21.2	16.5	38	13
		0.65	30 300	15.3	5.5	22.7	15.4	41.1	16
		0.7	35 800	12.5	5	24.1	14.1	44.3	19

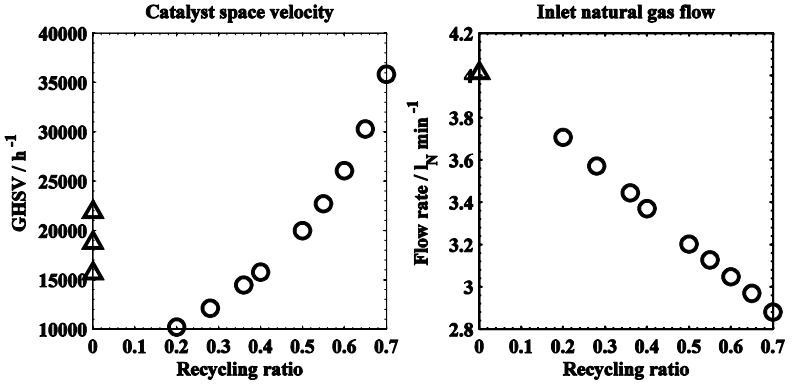

Figure 12. GHSV of the pre-reformer catalyst and the inlet natural gas flow rate in SR (Δ) and AOGR (O) modes for different recycling ratio values.

The temperature limits of carbon formation in AOGR mode were calculated using HSC6.1 [92] software to assess which experimental conditions could potentially

lead to carbon formation in the pre-reformer. The equilibrium temperature and composition of the pre-reformer outlet gas were calculated with the Cantera toolbox [101] using GRI-Mech 3.0 reactions developed for natural gas combustion [102]. The equilibrium was solved for an adiabatic system, where the total enthalpy and pressure between reactants and products was kept constant.

In addition to short-term experiments, the pre-reformer was held in selected conditions for a longer period to observe possible carbon formation or degradation of the catalyst performance. The conditions of the different holds are detailed in Table 4 and the longest hold was 1000 h.

Table 4. Operation conditions during extended holds.

Hold no.	Recycling ratio (-)	Inlet temperature (°C)	GHSV (h^{-1})	Hold time (h)
1	0.6	609	26,100	122
2	0.5	597	20,000	121
3	0.5	598	20,000	117
4	0.5	513	20,000	67
5	0.5	600	20,000	1000
6	0.2	589	10,200	165
7	0.2	646	20,300	165

4.1.3 Results and discussion

4.1.3.1 Risk of carbon formation at thermodynamic equilibrium

In order to evaluate the effect of AOGR on the performance of a precious metal-based catalyst, a pre-reformer was operated with simulated conditions relevant to an SOFC system using steam-reformed natural gas, with or without an AOGR loop. First of all, the risk of carbon formation was investigated and the carbon formation limits based on thermodynamic calculations are illustrated in Figure 13. According to thermodynamic equilibrium, the risk of carbon formation is more severe at a lower recycling ratio. This stems from the O/C value (also showin in Figure 13) which decreases with the recycling ratio, in other words, when less steam and other oxygen-containing species from the anode outlet are recycled back to the pre-reformer inlet. At a recycling ratio of 0.5, the calculated temperature limit of carbon formation is already below the typical operating temperature of anode-supported SOFCs (700–800 °C). However, the pre-reformer temperatures are typically lower, e.g. between 500 and 600 °C depending on the system layout; therefore there is a higher risk of carbon formation in the pre-reformer compared to the SOFC stack. Carbon is stable in equilibrium conditions at a typical operating temperature of a pre-reformer below a recycling ratio of about 0.65. The risk of

carbon formation was further assessed experimentally, as described below in Section 4.1.3.3. The experimental conditions tested in this work are illustrated in Figure 13 in the red rectangle.

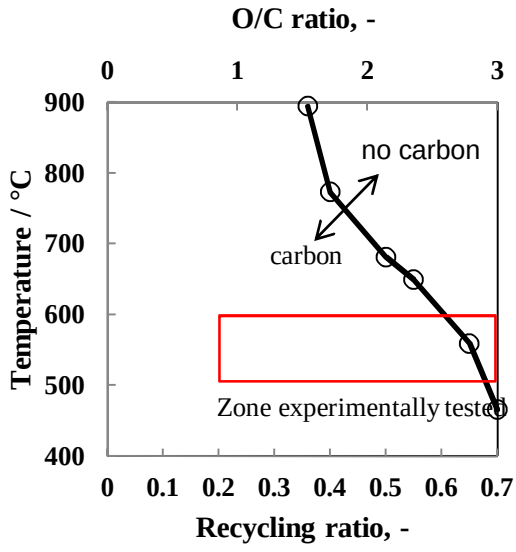

Figure 13. Temperature limit of carbon formation based on thermodynamic calculations in AOGR mode with a varying recycling ratio. The corresponding O/C ratios are shown in the secondary x-axis. The red rectangle shows the limits of the experimental conditions tested in this work.

4.1.3.2 Effect of AOGR on the performance of the pre-reformer

The performance of the pre-reformer and the catalyst were then tested by comparing the measured outlet temperature and gas composition with the values obtained by thermodynamic calculations. The inlet and outlet temperature of the pre-reformer are illustrated in Figure 14 in steam reforming and AOGR modes and the measured outlet temperature is compared to the calculated equilibrium outlet temperature. The difference between the experimental and equilibrium outlet temperature is larger in steam reforming mode compared to AOGR mode; this indicates that the equilibrium is not reached in steam reforming mode. This is also confirmed by the comparison of the experimental and equilibrium outlet gas fractions of methane and hydrogen in Figure 15. There is a systematic deviation from equilibrium values for the methane and hydrogen fractions in steam reforming mode, whereas experimental and equilibrium values are within the error limits in AOGR mode. Because both the outlet temperature and methane fraction are higher than the equilibrium values, kinetics is probably limiting the extent of the SR

reaction. In other words, to achieve equilibrium with this inlet gas composition and temperature, the GHSV should be reduced. Conversely, in AOGR mode, the equilibrium is reached regardless of the recycling ratio.

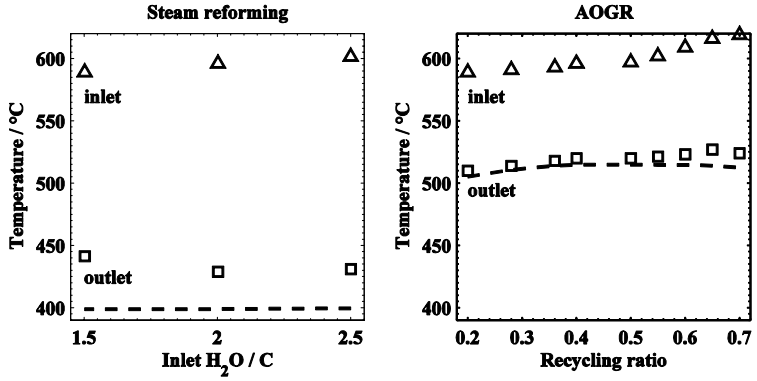

Figure 14. Inlet and outlet temperature of the pre-reformer in SR and AOGR modes. Δ: measured inlet temperature, □: measured outlet temperature, dashed line: calculated equilibrium temperature.

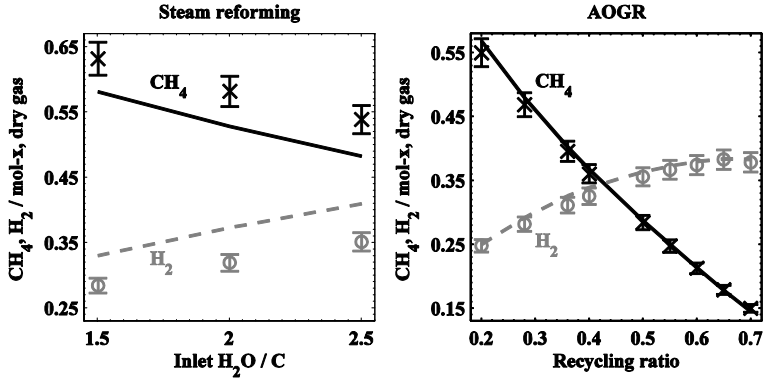

Figure 15. Molar fraction of methane and hydrogen at pre-reformer outlet with varying SR and AOGR conditions. Measured values are x: methane and O: hydrogen. Calculated equilibrium values are solid line: methane and dashed line: hydrogen.

In order to investigate possible limitations with regards to the GHSV in AOGR mode, the pre-reformer was tested with a fixed gas composition corresponding to a recycling ratio of 0.5 and with varying the GHSV from 20,000 to 35,000 h^{-1}, which is the maximum value achievable in this set-up. The methane and hydrogen fractions at the outlet as a function of GHSV are illustrated in Figure 16. The experimental values exhibit no deviation from the equilibrium values, which means that there is no kinetics limitation in the tested range of GHSV in AOGR mode.

The results show that equilibrium is more readily achieved in the pre-reformer tested using AOGR mode compared to SR mode. In other words, implementing an AOGR loop in the considered SOFC system enables a reduction in the size of this precious metal catalyst compared to the steam reforming case. This result contrasts with the conclusions of Peters et al., who reported that the use of AOGR caused a decrease in the activity of a nickel-based catalyst in AOGR conditions [99]. The difference between the results obtained by Peters et al. and those presented here probably originates from the catalyst used, nickel-based versus precious metal-based catalyst. Moreover, the catalyst can be used at high GHSV (at least up to 35,000 h^{-1}) without kinetics limitation at an inlet of 600 °C. As a comparison, nickel-based catalysts have been used at a much lower space velocity, in the range of 2000–6000 h^{-1} [100].

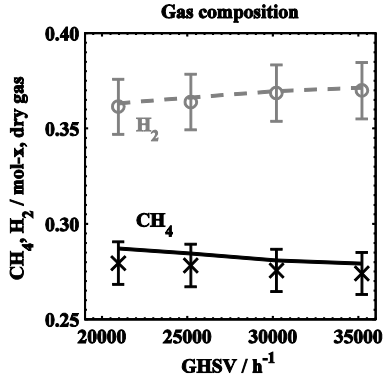

Figure 16. Molar fraction of methane and hydrogen at the pre-reformer outlet in AOGR mode with varying GHSV at recycling ratio of 0.5. x: methane, and ○:hydrogen. Calculated equilibrium values are presented with lines.

4.1.3.3 Carbon formation during extended holds

The pre-reformer also operated in selected conditions for longer time (see Table 4) to investigate possible carbon formation in the pre-reformer or change of catalyst performance. For this purpose, the pre-reformer outlet temperature, gas composition and pressure drop over the catalyst and filter were monitored during the hold. Additionally, after each hold, the set-up was flushed with nitrogen and air and the CO and CO_2 fraction at the set-up outlet was monitored to detect oxidation of possible carbon deposits. It should be noted that carbon is present at the thermodynamics equilibrium for all the conditions tested in Table 4 (see Figure 13).

The measured and calculated pre-reformer outlet temperature and methane fraction during the long-term holds are illustrated in Figure 17. It shows that there are no significant changes in outlet temperature and composition during the different holds. Moreover, the measured values are close to the calculated equilibrium

values. It is only during the last hold that an increase in the methane fraction is measured. However, in this condition, the gas composition corresponded to a recycling ratio of 0.2 and it is unlikely that such a low recycling ratio would be used in an actual system without an external steam supply because of the risk of carbon formation in the SOFC stack (see Figure 13).

Similarly to the outlet temperature and methane fraction, the pressure drop over the pre-reformer reactor did not change significantly during the holds with a variation of less than 1 mbar observed. This method is not very sensitive to a small amount of carbon. However, if equilibrium was reached, the amount of solid carbon expected would be about 50 g per hour at a recycling ratio of 0.5, which would certainly be detected in less than an hour. Moreover, the oxidation procedure carried out after each hold did not reveal any carbon accumulation at the reactor (detection limit of the order of 1 mg). These results indicate that carbon formation is not taking place to an extent that would compromise the operation of this pre-reformer in an SOFC system with the tested recycling ratios, even though carbon is present at thermodynamic equilibrium. This result is significant because it enables the optimisation of the system's operation and the minimising of the losses associated with a high recycling ratio. Additionally, they confirm that the experimental evaluation of the catalyst in the conditions of interest is needed to assess the actual risk of carbon formation.

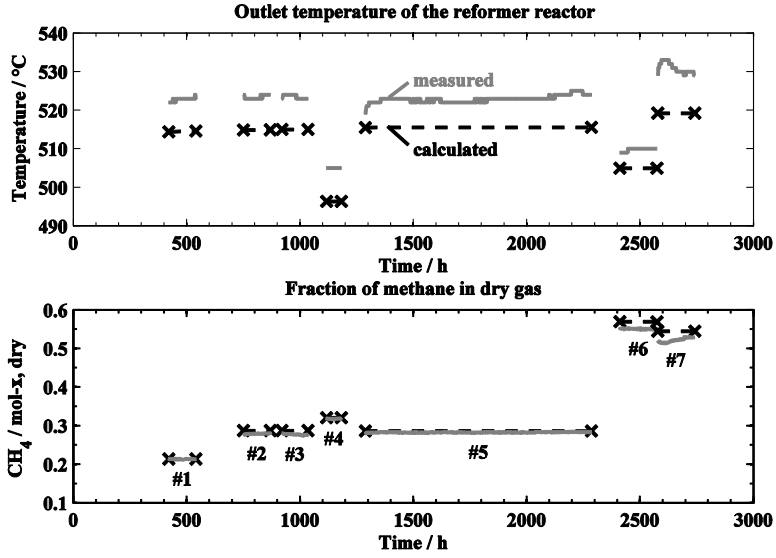

Figure 17. Temperature (above) and molar fraction of methane (below) at a reactor outlet during the experiment. The measured value is presented by a solid line and the calculated equilibrium value by a dashed line with markers at the ends.

The aim of this study was to generate the results necessary for the implementation of an AOGR loop in a 10 kW SOFC system. The main results are that the outlet gas of the tested pre-reformer and catalyst reach thermodynamic equilibrium more readily in AOGR conditions compared to SR conditions. No deviation from equilibrium was observed with a GHSV of 35,000 h^{-1} and a recycling ratio of 0.5. Lastly, carbon formation was not observed during long-term holds (up to 1000 h), despite carbon being stable at equilibrium in the tested conditions. Therefore, the pre-reformer and catalyst are considered suitable for implementation in a 10 kW system including an AOGR loop.

4.2 Generation of anode protective gas with the system pre-reformer (Publication IV)

4.2.1 Background

Commonly, SOFC anodes are made of a nickel cermet, where the particles of nickel are in their metallic form during operation. However, nickel can oxidise if the stack is hot (> ca. 300 °C) and no reducing gas is fed to the anode. The oxidation of nickel is very detrimental because it causes a loss of catalyst activity and a volume increase. Even if the nickel can be reduced again, the volume change causes mechanical stress and affects the durability of the stack [103]. Tolerance to reoxidation cycles depends on the microstructure and mechanical properties of the cells, and efforts are made to develop cells with improved tolerance [104,105]. Alternatively, it is possible to design and operate the BoP components of the SOFC system to avoid the conditions leading to nickel oxidation; in other words, to ensure that there is a reducing atmosphere when the stack is above ca. 300 °C. A critical time is the heat-up of the system, which might last several hours from room temperature to operating temperature (600–800 °C) in order to keep the thermal gradient and thermal stresses at an acceptable level. Nickel cermet anode was observed to start to oxidise at temperatures as low as 290 °C [106] and the oxidation kinetics increases with temperature [107]. Air can be present on the anode side because of the transport from the cathode to the anode side through the electrolyte or stack seals [108] and air might have migrated to the anode side from the exhaust when the system was shut down. Therefore, a forced flow of reducing protective gas is necessary during heat-up to displace the oxygen and maintain reducing conditions at the anode.

As explained in Section 4.1, SOFC systems that include an AOGR loop achieve higher efficiencies and potentially simpler design compared to an SOFC system without AOGR [109]. However, the AOGR loop needs to be operating during the heat-up phase in order to heat up all the system components. As a consequence, the air that leaks to the anode side is force-fed back to the pre-reformer inlet, which increases the risk of anode reoxidation.

The simplest and safest way to protect the anode during heat-up consists of using premixed protective gas such as 4%-vol hydrogen in nitrogen. This approach is not practical for commercial applications because such premixed protective gas is expensive and due to the lengthy heat-up time, a relatively large amount is needed. For example, five cylinders of 50 L at 200 bars would be needed to heat up and start up the 10 kW demonstration unit [43]. Lastly, the protective gas cylinders require space and their replacement and logistics add up to the operation and maintenance costs. There is therefore a clear incentive to produce such protective gas within the SOFC system and it can be accomplished by reforming natural gas in the pre-reformer by providing the steam with the start-up steam generator. The challenge consists of operating the pre-reformer at a sufficiently high temperature for the catalyst to be active for steam reforming while avoiding carbon deposition in the pre-reformer and at the anode during heat-up. Additionally, carbon-containing species can form nickel carbonyl at the anode below 230 °C according to reference [105] and the toxicity of this gas is extremely high (the lowest published lethal concentration for humans is 30 ppm for 30 min [110,111]; therefore, the conditions for its formation should be strictly avoided.

Publication IV presents a study aiming at developing a method to heat up the 10 kW demonstration unit without premixed protective gas using natural gas and steam. Firstly, ex-situ experiments were conducted on a pre-reformer test bench. The aim of these experiments was to realise the suitable operating parameters of a pre-reformer at low temperature (<500 °C) in a system with an AOGR loop and air leakage (i.e. forced oxygen supply to the fuel system). Secondly, the results of the ex-situ experiments were used to develop a safe heat-up procedure for a 10 kW SOFC system without the use of premixed protective gas. A series of heat-up cycles were performed on the SOFC system and the performance of the stack was investigated after each heat-up. Several authors have investigated the heat-up of an SOFC by modelling [103,112,112-114], but at the time of writing, no experimental work describing the heat-up of a planar SOFC system with AOGR had been published previously.

4.2.2 Experimental

4.2.2.1 Ex-situ pre-reformer experiments

The ex-situ experiments were performed on a pre-reformer test bench described in Figure 11 in Section 4.1.2. The aim of these experiments was to assess the activity of a precious metal monolith catalyst at low temperature in natural gas steam reforming. The light-off temperature was determined by the pre-reformer inlet gas temperature at which the pre-reformer starts to convert methane to hydrogen according to the steam reforming reaction (Equation 4).

The gas outlet composition was monitored continuously with an online gas analysis equipment (IR-based for CH_4, thermal conductivity for H_2 and paramag-

netic for O_2, Sick Maihak S700 series). The analyser results should be used to evaluate trends rather as quantitative measurements because of the different channels' cross-sensitivity. The temperature of the inlet gas was ramped up from 200 to 550 °C at a rate of about 2 °C min^{-1}. The GHSV of the pre-reformer was about 32,000 h^{-1}. The investigated inlet gas flows are listed in Table 5. These conditions are relevant to the gas composition of an SOFC system using AOGR, when the steam and fuel supply have just been initiated and the temperature is too low to expect reforming activity in the pre-reformer or in the stack. Without reforming, the gas in the recirculation loop consists of natural gas, steam and the air originating from stack leakages. The gas composition in run 1 includes only natural gas (98% methane), steam and nitrogen. This is the zero-leakage case. In runs 2–7, a small fraction of air was added to simulate the effect of air leakage on the activity of the pre-reformer. In runs 3–7, hydrogen was added with varying H_2/O_2 ratio from 0 to 4 according to Equation 19.

$$O_2 + 2H_2 \rightarrow 2\ H_2O \tag{19}$$

Nitrogen was added to all runs because a sufficient flow of carrier gas is needed to operate the steam evaporator and mixer (CEM-303, Bronkhorst). Nitrogen is not expected to react in the tested conditions.

Table 5. Test gas mixtures used for determining the light-off temperature.

Run		1	2	3	4	5	6	7
Gas flow / NLPM	NG	0.5	0.5	0.5	0.5	0.5	0.5	0.5
	H_2O	10	10	10	10	10	10	10
	N_2	10	10	10	10	10	10	10
	H_2	-	-	0.2	0.05	0.1	0.15	0.4
	Air	-	0.5	0.5	0.5	0.5	0.5	0.5
H_2/O_2			0	2	0.5	1	1.5	4

4.2.2.2 System heat-up experiment

The experiments at system level were realised with the 10 kW demo unit, which is described in Section 2.5 and illustrated in Figure 2. The system included a 10 kW stack consisting of 64 anode-supported cells (Versa Power Systems [115]). The heat needed for the system heat-up was primarily provided by the electrical heater located at the stack air inlet inside the module, and secondarily heat-up was assisted using an electric heater in the AOGR loop.

Based on the results obtained from the ex-situ pre-reformer tests, a heat-up procedure was developed that would not use any premixed protective gas. The heat-up procedure is illustrated in Figure 18 and consists of four phases.

1. The stack is heated up from room temperature to over 200 °C and all the other fuel subsystem components to at least 100 °C, without any forced flow to the system fuel inlet. The cathode air blower and the AOGR blower are in operation throughout the entire heat-up procedure.
2. Steam is introduced to the fuel side using the steam start-up generator when the stack temperature is above 200 °C. The natural gas was fed in only when the stack temperature was above 300 °C to avoid the risk of formation of toxic nickel carbonyl in the SOFC stack. Pre-reformer light-off was triggered by a short-term hydrogen pulse.
3. The stack is heated up to a temperature of 700 °C. The anode is protected from reoxidation by the hydrogen produced by the natural gas steam re-forming reaction.
4. The electrical loading of the stack is started and the fuel is proportionally increased. When sufficient steam is produced in the stack, the external steam supply is stopped.

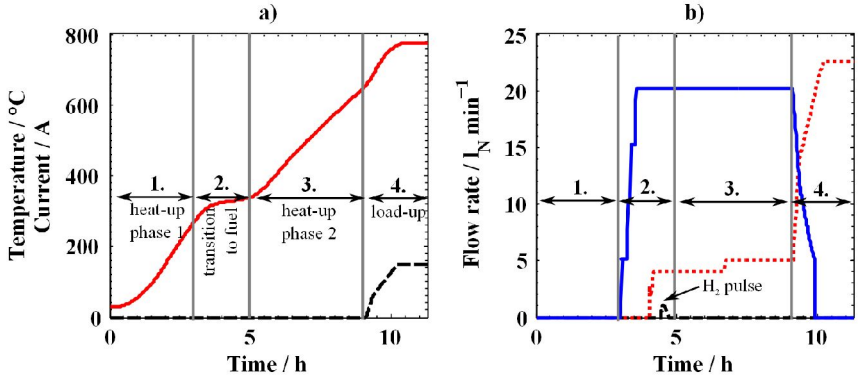

Figure 18. Experimental start-up. (a) Stack temperature (solid line) and current (dashed line) (b) Flow rate of hydrogen pulse (dashed line), fuel (dotted line) and steam (solid line).

4.2.3 Results and discussion

4.2.3.1 Ex-situ pre-reformer experiments

The activity of a precious metal catalyst in steam reforming was investigated at a low temperature on an ex-situ pre-reformer. Figure 19 illustrates the outlet gas composition against the inlet temperature of the pre-reformer for the different investigated runs, see Table 5. In Figure 19 (a), it can be seen that the catalyst

exhibits some measureable activity at 235°C with the inlet gas from run 1 (zero-leakage case). The methane conversion increases gradually with the inlet temperature. The inlet temperature at which the methane conversion starts is further referred to as the light-off temperature. In Figure 19 (b), some air is added to the inlet gas to simulate the effect of air leakage in the system (run 2). Conversely to the “zero-leakage case”, the catalyst exhibits no activity before its inlet reaches ca. 390 °C. Above this temperature, the reforming reaction starts abruptly and then methane conversion increases gradually. Apparently, the presence of oxygen has an inhibiting effect on the tested catalyst at low temperatures. In Figure 19 (c), hydrogen is added at a stoichiometric ratio with oxygen (run 3) and methane conversion is already observed at 200 °C. Apparently, the combustion of hydrogen (Equation 19) occurs at 200 °C, which removes the inhibiting effect of oxygen and increases the temperature in the catalyst. Qualitatively, this result is similar to the one obtained in run 1 (Figure 19 (a)), in other words, the methane conversion starts at as low a temperature as around 200 °C.

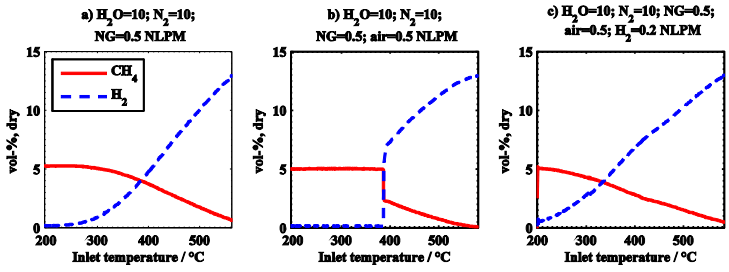

Figure 19. Pre-reformer dry outlet gas composition against pre-reformer inlet gas temperature. (a) Fuel and steam (zero-leakage case, run 1), (b) addition of air (run 2) and (c) addition of air and hydrogen at stoichiometric ratio (run 3).

Figure 20 illustrates the effect of different H_2/O_2 ratios in the inlet gas on the light-off temperature of the pre-reformer. With no hydrogen present, the light-off temperature is as high as ca. 390 °C, the light-off temperature then decreases when the H_2/O_2 ratio is increased. At a H_2/O_2 ratio of two (stoichiometric ratio of equation 19), the light-off temperature is below 200 °C. These results indicate that the steam reforming of methane can be triggered in two ways during the heat-up of an SOFC system: either to increase the temperature of the pre-reformer inlet to about 400 °C in order to overcome the inhibiting effect of oxygen originating from leakages, or to add a relatively small amount of hydrogen to decrease the light-off temperature to below 200 °C. From a system point of view, it is beneficial to be able to reform the natural gas to hydrogen-containing reformate as early as possible during the heat-up procedure. If hydrogen can be generated before the temperature of the anode is above 300 °C, the need for premixed protective gas to protect the anode from reoxidation can be completely suppressed. These results are further exploited to design a procedure to heat up an SOFC system without the use of premixed protective gas.

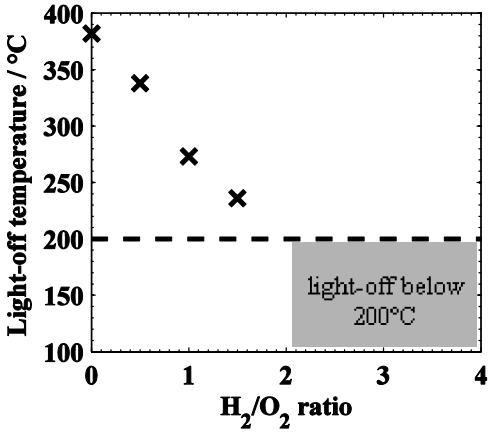

Figure 20. The effect of the H_2/O_2 ratio on the light-off temperature of the pre-reformer, results from runs 2–7.

4.2.3.2 System heat-up experiments

The heat-up of the 10 kW demo unit was experimentally investigated and a selection of the results is depicted in Figure 21. It should be noted that the anode inlet concentration (Figure 21 (c)) also corresponds to the pre-reformer outlet concentration. During the first phase, the stack was heated up until ca. 350 °C (Figure 21 (a)). The anode inlet concentration was about 21% oxygen, meaning that mostly air was present in the fuel system (Figure 21 (c)). At t = 4 h, the oxygen concentration decreased by about 1%, when the stack temperature was between ca. 200 and 350 °C, which is explained by the slow start of the oxidation of nickel at the anode. During the second phase, 20 NLPM of steam feed was initiated when the stack was ca. 350 °C at t = 4 h. At t = 5 h, 4 NLPM of natural gas was fed into the system and the concentration at the anode inlet was measured to be about 50% methane and 8% oxygen, indicating that the amount of air leak to the fuel side was approximately of the same magnitude, i.e. 4 NLPM. The pre-reformer inlet and outlet temperature are very close (Figure 21 (b)), indicating that no reforming reaction is taking place at the pre-reformer between t= 3.5…5.5. This result is similar to that obtained in the ex-situ pre-reformer, where the reforming reaction is inhibited by the presence of oxygen under 400 °C. At t = 5.5 h, a short hydrogen pulse (15 minutes) is initiated and can be seen as a stack voltage increase (Figure 21 (a)) and by the increase of the pre-reformer outlet temperature, which means that hydrogen reacts with the oxygen that is present and is confirmed by the drop in oxygen concentration at the anode inlet. At the same time, a small amount of methane is converted and the hydrogen concentration at the pre-reformer outlet is about 2% after the termination of the hydrogen pulse. The third phase consists of resuming the heat-up of the stack to 700 °C. During t = 5.5…6.5 h, the pre-reformer catalyst activity is only slightly increasing. At t = 6.5 h, at a stack temper-

ature of about 400 °C, the nickel of the anode is reducing, the cell voltage increases suddenly and methane starts to be reformed in the stack, as seen in the large decrease of methane and increase of hydrogen concentration at the anode inlet. The fourth and final phase consists of electrical loading of the stack (not shown in Figure 21).

In short, the oxygen present on the fuel side during heat-up starts to partially oxidise the anode at temperatures below 350 °C and inhibits the steam reforming reaction at the pre-reformer. A hydrogen pulse is needed to remove this molecular oxygen by catalytic combustion with hydrogen on the precious metal catalyst of the pre-reformer and to start the production of a small amount of hydrogen in the pre-reformer. When the stack temperature increases further to about 400 °C, the nickel fraction of the anode that had oxidised is reduced and natural gas is reformed in the stack. The heat-up can proceed without excessive oxidation of the anode.

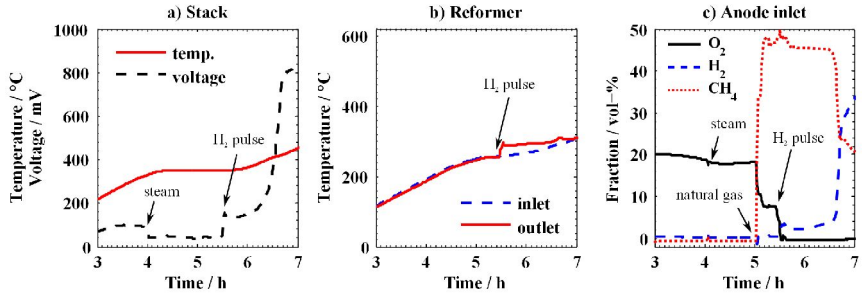

Figure 21. Heat-up of the 10 kW demo unit without premixed gas (a) stack temperature and average cell voltage, (b) inlet and outlet temperature of the pre-reformer (c) fraction of methane, hydrogen and oxygen at the anode inlet on a dry basis.

The cell voltage after experimental heat-up is used as an indicator of damage to the stack during the heat-up procedure. The difference in individual cell voltage at 150 A before and after two experimental heat-up procedures is depicted in Figure 22. Most of the voltage changes were small and within 10 mV for the majority of the cells and the average cell difference is below 1 mV. The result from the cell #64 is not considered because this cell was already severly degraded before the experimental heat-up procedures and its result are consequently not considered relevant. Therefore, the experimental heat-up without the use of premixed protective gas appears to have caused no measurable degradation to the stack. This result validates the possibility of producing the reducing protective gas inside the system at the pre-reformer using a hydrogen pulse. However, the results obtained from the ex-situ pre-reformer suggest that natural gas can be reformed in the presence of oxygen if the temperature of the pre-reformer inlet is above 400 °C. Therefore, the system could be further simplified by eliminating the hydrogen

pulse if the pre-reformer inlet gas could be heated up to above 400 °C when the stack is at about 350 °C.

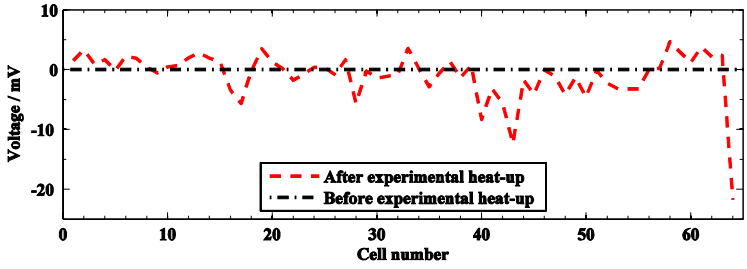

Figure 22. Difference in individual cell voltages after two experimental heat-up procedures.

5. Performance and material compatibility of hybrid seals (Publication V and VI)

5.1 Background

Compressive seals composed of mica-type paper have been investigated for SOFC stack applications [32,35,36]. They have the advantages of having good thermal cycling capability and being easy to handle during stack assembly [116]. However, they exhibit a relatively high leak rate, principally due to the presence of interfacial leak paths between the seal and adjacent stack components [37]. For this reason, they require high compressive stresses (usually at least 2 MPa) to decrease the extent of these interfacial leak paths for adequate sealing performance [35,36,117]. For example, in Publication I, the stack had a cell footprint of 100 cm^2 and the applied load on the stack was about 2000 kg, corresponding to about 4 MPa on the seals. Compression is needed in SOFC stacks to ensure adequate sealing performance when using compressive seals and good electrical contact between cells and interconnects. There are multiple benefits to reducing the compression requirement for the stack, such as reducing the compression system size and its complexity. Additionally, the compression rods usually need to go through the stack insulation; therefore, the thinner the rods, the smaller the heat loss. A smaller compression also enables the use of thinner and less robust stack components. This means that there are clear benefits to decreasing the compression stress needed on compressive seals, while retaining the easy handling and assembly of this type of seal.

To overcome the drawbacks of the compressive seals, hybrid seal concepts have been developed. The principle is to have a core made of compressible materials sandwiched between layers of compliant materials that would block the interfacial leak paths. Thus, the hybrid seal inherits its mechanical properties from the compressible core but exhibits a low leak rate, even at lower compression stresses. This enables the compressible core to deform in response to thermomechanical stresses without causing the failure of the seal. The hybrid seal concept has been investigated by Chou et al. using different micas for the compressible core and glass or silver foil as compliant layers [118-124].

In addition, it is essential that the sealing materials exhibit limited material interactions with the other SOFC stack components to ensure sufficient stack durability. Sealing material interaction studies have previously been published in the literature, on pure ceramic glass seals [62,125] or on compressible seals [126,127]. They observed different forms of accelerated corrosion that all took place preferentially at the three-phase interface sealing material/interconnect steel/air. Chou et al. presented a post-experimental analysis of a stack using hybrid seals [128]. They concluded that material interaction was limited and that their material selection for the seal and interconnect material was suitable for long-term operation. However, the three-phase interfaces between seal/interconnect/gas were not discussed.

The work presented here contributes to the field of sealing solutions for SOFC by presenting the hybrid seal development at VTT Technical Research Centre of Finland. The sealing solution uses Thermiculite 866 [129] as a compressible core coated with glass using an organic carrier. The advantages of using Thermiculite 866 over traditional mica-type paper are its improved gas tightness, because of the presence of steatite filler between the vermiculite platelets, and its superior compressibility [35]. The method presented here enables easy stack manufacturing because the seal can be coated beforehand, cut to shape and handled in the same way as traditional compressible gaskets. The organic carrier present in the glass coating is burned out in the first heat-up and the remaining glass forms a thin conformable interlayer between the seal core and adjacent stack components. The major advantage of the conformable core is also its ability to compensate for manufacturing tolerances of the adjacent components. Publication V presents the manufacturing method of the coated seals and the results from ex-situ leakage tests. The possible material interactions between seals and adjacent components have been investigated in Publication VI, where a post-experimental analysis of an SOFC stack using hybrid seals is detailed. The stack operated for 1800 h at 700 °C. The in-situ nature of the experiment provides exposure conditions to the seals and interconnects that are more relevant to stack operation compared to ex-situ experiments.

5.2 Experimental

5.2.1 Ex-situ leak rate measurement

The improvement brought about by adding compliant glass layers to compressive sealing materials was evaluated by leak rate measurements of seal samples made of Thermiculite 866 (Flexitallic Ltd) material, either uncoated or coated with glass layers. Thermiculite 866 is a commercial compressive material composed of vermiculite and steatite. The materials of the seal were selected to target operation at 700 °C. The glass used was a commercial glass with a softening temperature of 650 °C to obtain a compliant layer.

For the leak test experiments, Thermiculite 866 was coated by wet spraying. A fluid mixture of glass powder and organic carrier (24%-weight of Terpineol, 75%-weight of ethanol and 1%-weight of ethyl cellulose) was prepared with a glass-to-organic ratio of 0.5 by weight. After coating, the coated substrate was cut to the required shape. All the seals were heated from room temperature up to 700 °C using a 1 °C min^{-1} ramp rate.

The set-up used to measure the leak rate ex-situ is illustrated in Figure 23. Mass flow controllers fed gases to the sample line and exhaust line. The pressure inside the seal was controlled with a back pressure controller. During heat-up, air was fed to the seal samples to burn off the organic binders. The seal samples were ring-shaped with an outer diameter of 40 mm. The seal samples were placed on a 10 mm-thick Crofer 22 H bottom plate, from where the gas was fed to the samples. A 1 mm-thin plate of Crofer 22H was placed on top of the seal sample and weight plates were added on top of it. The measurement set-up mimics the conditions inside a stack by using the relevant test temperature, heat-up procedure, steel materials, hydrogen-containing gas and applied stress on the seal sample, but the measurement is qualified as ex-situ because it is not conducted inside a stack.

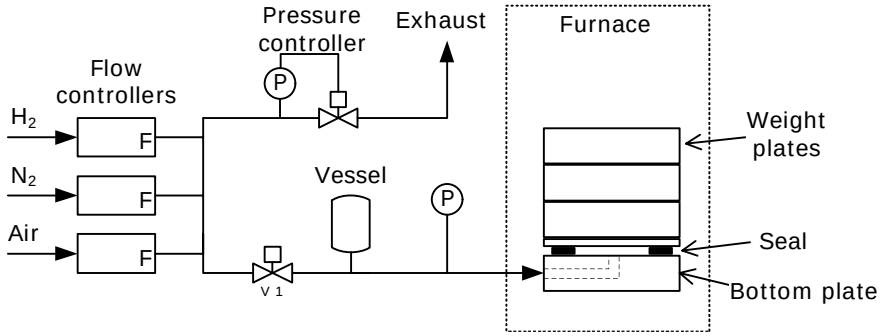

Figure 23. Measurement set-up for the ex-situ leak rate test.

After heat-up, the pressure inside the seal was set 25 mbar above ambient in a gas mixture of nitrogen and hydrogen at 700 °C. Leak rate measurements were performed periodically by shutting off valve V1 and measuring the pressure decay. A vessel of a known volume was connected to the sample line, enabling calculation of the leak rate as a function of pressure from the pressure decay curve. Based on the ideal gas assumption, the leak rate is proportional to the slope of the pressure decay curve and can be expressed as

$$\dot{Q} = V \frac{T_{ntp}}{T\, p_{ntp}} \frac{dp}{dt} \tag{20}$$

where V is the combined volume of the vessel and the sample line, T is the temperature of the gas in the volume and T_{ntp} and p_{ntp} are normal temperature and pressure. This method was used to measure the leak rates of Thermiculite 866, either uncoated or glass-coated.

5.2.2 Stack testing

Hybrid seals were tested in a single-cell stack in order to observe material interactions between seal materials and other stack components during operation. The stack used a cross-flow configuration. Its metallic components were made of Crofer 22 APU (ThyssenKrupp). The anode-supported cell was provided by Elcogen AS and its dimension was 100 mm x 100 mm. Hybrid seals were used for all seals located between Crofer 22 APU plates and are made with Thermiculite 866 between two glass tapes of 220 µm green thickness. The glass used is a commercial product from Schott (GM31107), which belongs to the system MO (M = Mg, Ca)-Al_2O_3-BaO-SiO_2-B_2O_3 [130]. The Thermiculite 866 is composed in nearly equal amount of vermiculite and steatite, the compositions of which are [(K, Mg, Fe)$_3$(Si,Al)$_4$O$_{10}$(OH)$_2$] and [$(Mg_3Si_4(OH)_2$] respectively. The seal between the cell electrolyte and Crofer 22 APU plate was made of a glass tape without Thermiculite 866. Forty kilograms of weight was added on the stack, which corresponds to a compressive stress on the seal of ca. 0.1 MPa, assuming all the weight was carried by the seals and not by the cell.

Dry hydrogen and dry air (ca. 0.1%-vol water) were used as fuel and oxidant. Pure hydrogen exposes the seals to a worst-case condition as the leak rate through the hybrid seal increases with the concentration of hydrogen as discussed in Section 5.3. The stack was operated at 700 °C for 1800 h. The average current density was 0.2 A cm^{-2} and fuel utilisation and air utilisation were both 18%. The hydrogen cross leak value was calculated from the relative humidity at the cathode outlet according to the following equation.

$$\dot{Q}_{H_2}^{cross} = X_{H_2O}^{C,out} \left(\dot{Q}_{Air}^{C,in} - \frac{I}{4F}\frac{RT_{ntp}}{p_{ntp}}\right) \quad (21)$$

where $X_{H_2O}^{C,out}$ is the steam molar fraction at the cathode outlet, $\dot{Q}_{Air}^{C,in}$ is the cathode air inlet flow, I is the current drawn from the stack, and F is the Faradic constant. These calculations are based on the assumption that the different leak rates are small compared to the cathode air flow.

After the test, the stack was mounted in epoxy resin and a cross-section sample was extracted near the air outlet for SEM and EDS analysis.

5.3 Results and discussion

The leak rate of seals made of Thermiculite 866 and glass-coated Thermiculite 866 were investigated in order to assess the improvement brought by the addition of a compliant glass layer between the Thermiculite 866 and the adjacent sealing surfaces. The leak rates of seals were studied as a function of the pressure difference across the seal and gas composition. In addition, a stack using a hybrid seal was assembled, tested and post-experimental microscopy analysis was conducted to study possible material interactions between seal materials and other stack components.

The leak rates as a function of pressure at compression stress of 0.1 and 0.4 MPa are detailed in Figure 24. The Thermiculite 866 was coated by wet spraying and the glass coating after heat treatment was about 10 µm. It can be seen that coating the Thermiculite 866 with glass decreases the leak rate, especially at low compressive stress. At low compressive stress and with a pressure difference of 20 mbar, the leak rate of the coated Thermiculite 866 is about 0.4 ml (m min)$^{-1}$, which is a reduction of about 85% compared to the uncoated one (2.7 ml (m min)$^{-1}$). The allowable leak rate in an SOFC stack is specific to the design of the stack and its operation conditions. However, it is common sense to strive to develop a seal with the lowest leak rate at low compression stress to limit the fuel loss that limits the SOFC efficiency, and to decrease the risk of local oxidation of the nickel due to air leakage to the anode side. The results presented here are coherent with findings in the literature, although direct comparisons are difficult due to different conditions used. Chou et al. reported leak rates below 1 ml (m min)$^{-1}$ using hybrid seals made of mica paper coated with glass at compressive stresses of 0.04–0.7 MPa [118,121,131].

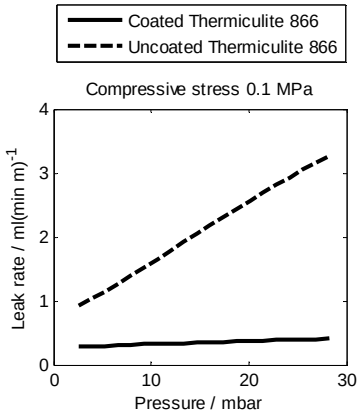

Figure 24. Leak rates of coated and uncoated Thermiculite 866 at compressive stress of 0.1 MPa in 50%-vol H_2 in N_2.

Figure 25 presents the leak rates as a function of pressure for coated and uncoated Thermiculite 866 with different hydrogen fractions. It can be seen that the uncoated Thermiculite 866 exhibits a leak rate which depends on the pressure difference and the gas composition. Conversely, the leak rate of the coated Thermiculite 866 depends only on the hydrogen concentration and is independent of the pressure difference. These results suggest that glass coating effectively blocks the direct interfacial leak paths and the remaining observed leak rate is due to concentration-driven diffusion rather than pressure-driven advection.

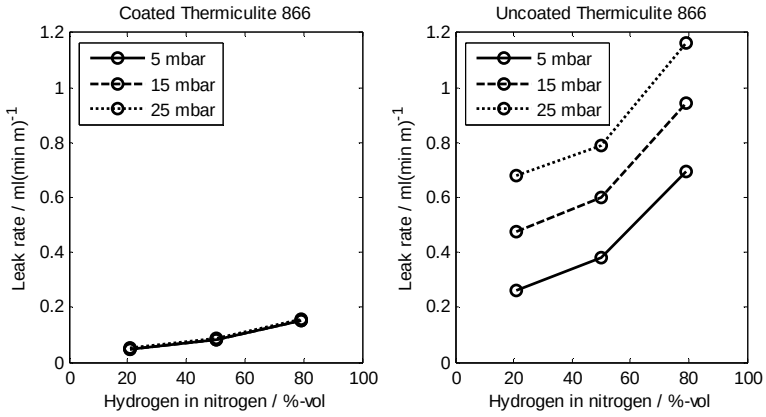

Figure 25. Leak rates of coated (left) and uncoated (right) Thermiculite 866 at different pressure differences as a function of hydrogen concentration. Compressive stress is 0.4 MPa.

A cross-section of a single-cell stack operated for 1800 h was investigated by SEM and EDS in order to investigate seal microstructure and possible material interactions. Figure 26 illustrates a cross-section of two hybrid seals from a single-cell stack. It can be observed that the glass has effectively covered the Thermiculite 866 and adapted to the thickness variations. For example, the dye-cutting process used to cut the seal to shape can form cutting burrs near the edges of the seal. This effect is particularly marked in the upper seal, where the glass coating has accommodated a gap varying from 15 to 150 µm. Some porosity can be seen in the glass where it is at its thickest (at the “150 µm” annotation in Figure 26). However, the pores are closed and do not form a continuous leak path. Additionally, the gap clearances between the Crofer 22 APU plates are 710 and 580 µm at the location of measurement, and this difference did not seem to affect the quality of the seal at this location. This illustrates the benefits of using hybrid seals over purely compressible seals. In short, similar hybrid seals were able to effectively seal gaps of 710 and 576 µm and the glass layer was able to accommodate up to 140 µm of thickness variation in the Thermiculite 866. Compressive seals would have needed much higher compression stress in order to effectively accommodate the different gap clearance and to flatten the cutting burrs. Variations in gap clearance can be caused by the variation of thickness of the stack components (cells, gaskets, interconnects). This variation can be minimised by tight manufacturing tolerance, but this comes at higher costs. Therefore, it is highly advantageous to have a sealing solution that can accommodate the geometric variation in a stack.

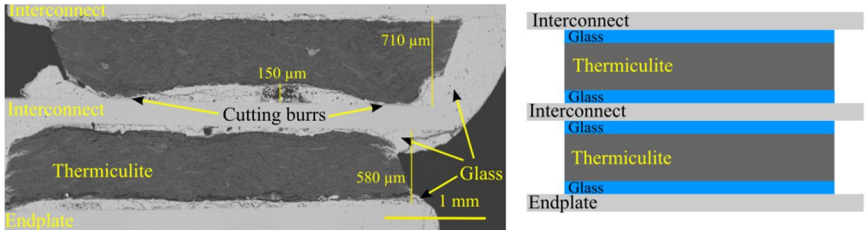

Figure 26. SEM-BSE cross-section of two hybrid seals. The seals are composed of a Thermiculite 866 core between two glass layers.

At nominal condition, the hydrogen cross leak value corresponded to a loss of 0.9% of the inlet hydrogen flow, which is a promising result for the first short-stack using this type of hybrid seal. Moreover, the hydrogen cross leak value remained constant during the 1800 h of the test as illustrated in Figure 27, showing that the performance of the seal did not degrade over time.

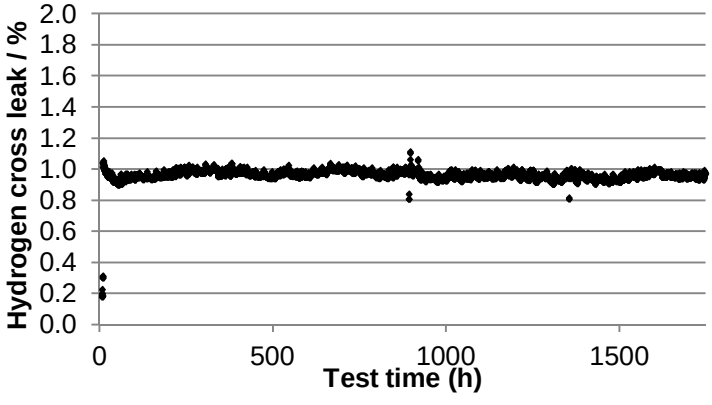

Figure 27. Hydrogen cross leak expressed as a percentage of the hydrogen fuel inlet flow.

The Crofer/glass and glass/Thermiculite 866 interfaces are shown in Figure 28. The location corresponds to the middle of a seal section, therefore the exposure to gas is limited to the leak through the seals. The oxide layer is found to be less than 1 µm, which corresponds to the oxide layer thickness of the interconnect far from the seal location. It appears that the glass has not affected the oxidation of the steel and therefore material interactions are limited at this interface. Additionally, there is no visible interaction between the glass and Thermiculite 866.

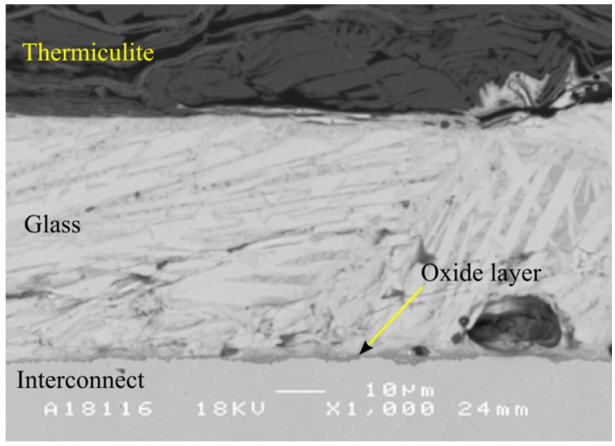

Figure 28. SEM-BSE cross-section of Crofer/glass and glass/Thermiculite 866 interfaces.

Four Crofer/glass/air interfaces are illustrated in Figure 29 and Figure 30. Figure 29 (a) and (b) depicts the upper and lower corners of the same seal exposed to the same cathode atmosphere. Despite the fact that they are exposed to the same conditions, their oxidation behaviour is very different. The upper seal does not exhibit any significant corrosion, whereas an oxidation layer of 20 µm in thickness has developed where the seal glass layer ends. The oxidation layer extends about 200 µm from the three-phase boundary. The composition of the oxidation layer has been investigated by EDS (Figure 29 (d)) and shows that the oxide layer is divided into an inner layer composed mainly of chromium oxide and a top layer composed of iron oxide. This corresponds to a break-away oxidation, i.e. when the chromium oxide can no longer protect the steel from rapid oxidation.

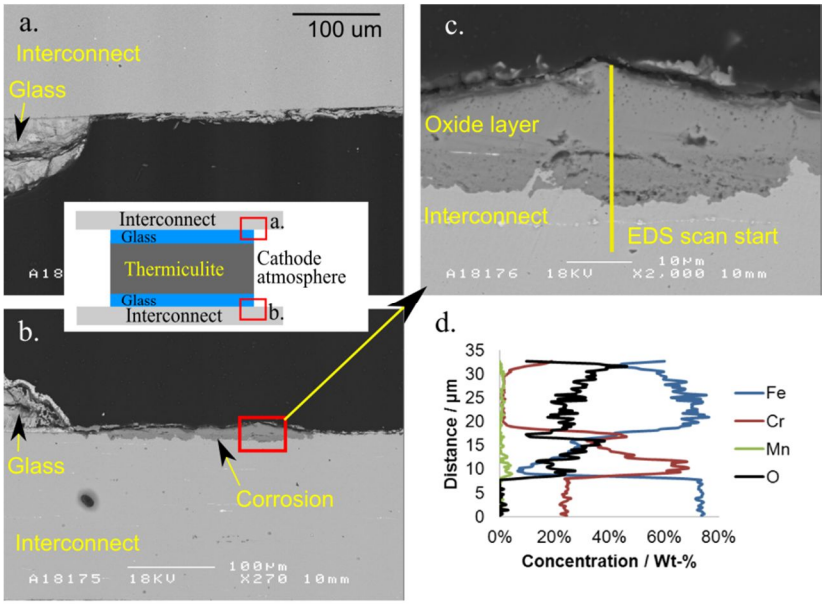

Figure 29. SEM-BSE cross-sections of two Crofer/glass/air interfaces (a and b) that are both exposed to cathode atmosphere. Magnified view of cross-section (c).

Similarly, Figure 30 depicts the three-phase interfaces of two different seals but which are exposed to the same air exhaust atmosphere from the air manifold. Also in this case, one interface (Figure 30 (a)) exhibits no significant oxidation, whereas a 20 µm-thick oxidation layer can be seen on the steel at the three-phase interface. Accelerated oxidation was also found further in the air manifold towards the stack air outlet. The oxide layer was thickest 5 mm away from the air manifold seals, where its thickness reached 120 µm (picture not shown). However, corrosion in the manifold of the thick endplate is not critical for stack performance.

There can be different causes for accelerated oxidation of the interconnect stainless steel. Chromium evaporation is enhanced in the presence of water vapour [91]. The water vapour concentration can be locally higher due to a hydrogen leak into the air atmosphere. However, this is not the case here, because there is air on both sides of the seals where accelerated oxidation was found. The heavy oxidation that was found deep in the manifold could be attributed to the presence of lubricant from machining. The endplates were lubricated during machining and were subsequently heat-treated (800 °C for 12 hours), polished and only then cleaned in a laboratory dishwasher and wiped with ethanol-impregnated tissues. However, it is difficult to remove lubricant or residue from burned lubricant from the narrow manifolds. This hypothesis is supported by the fact that the heaviest oxidation was found deep in the manifold, away from the seals. Lastly, the corrosion could be attributed to the transport of elements from the glass or the Thermiculite 866 to the stainless steel, where they could promote rapid corrosion.

However, if material interaction was the corrosion mechanism, one would expect it to happen systematically like in [126,127], which is not the case here.

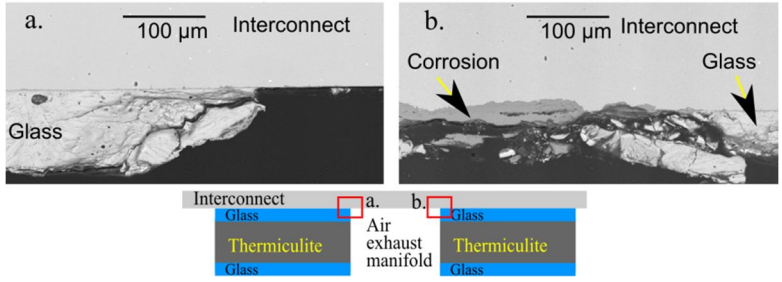

Figure 30. SEM-BSE cross-sections of two Crofer/glass/air interfaces (a and b) that are both exposed to the atmosphere of the air exhaust manifold.

Bram et al. also found accelerated oxidation in their work on material interaction between Thermiculite 866 and Crofer 22 APU (no glass used) [127]. They exposed their sample in ambient air at 600 °C for 400 h, which resulted in a very thick oxide layer (80–100 µm) that extended more than one mm away from the Thermiculite 866. They attributed the corrosion to an increase of water vapour content due to the dehydration of vermiculite and the decomposition of steatite. Wiener et al. also conducted research on the material interaction between Crofer 22 APU and Thermiculite 866 [126]. They exposed their Thermiculite material to 800 °C for 400 h in ambient air and also found accelerated oxidation. Their oxide layer was about 20 µm in thickness near the seal material. They explained the oxidation behaviour by the transport of magnesium from the steatite contained in the Thermiculite 866.

The most likely reason for the observed accelerated corrosion in the tested stack was attributed to the contamination from lubricant that was not properly removed during stack assembly. However, material interaction between the glass and the Thermiculite 866 cannot be ruled out. The main risks associated with oxidation on the interconnect in the vicinity of the seals is either the formation of porous oxidation product all the way through the 0.2 mm interconnect or that the oxidation product forms a conductive bridge between two interconnects, resulting in short-circuiting. However, in our case the extent of corrosion is rather limited after 1800 h. Corrosion was only found at the three-phase interface between glass, steel and air, which is consistent with the results of several previous study [62,125-127]. Therefore, the author recommends that the three-phase interface should always be included in material interaction studies between seals and interconnects.

The last interfaces investigated were the Crofer/glass/humid hydrogen interface, illustrated in Figure 31, and the glass/YSZ-electrolyte interface in Figure 32. The Crofer 22 APU oxide layer is below 1 µm next to the glass seal and no visible interaction is visible between the glass and the electrolyte material. In short, no

accelerated oxidation could be observed at the three-phase interface Crofer/glass/humid hydrogen and between the glass and the electrolyte materials.

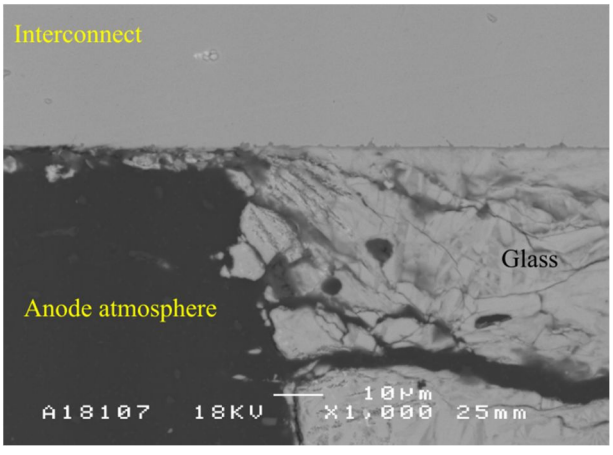

Figure 31. SEM-BSE cross-section at the Crofer/glass/humid hydrogen interface. The visible glass is part of the cell seal which is composed of glass without any Thermiculite 866.

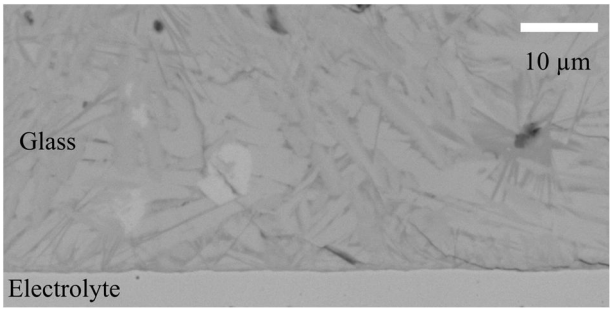

Figure 32. SEM-BSE cross-section at the interface between glass and electrolyte.

6. Summary and conclusions

SOFC systems are expected to play an important role in the power generation sector due to their advantages in terms of high efficiency, fuel flexibility, modularity and very low emissions. However, their high cost remains a burden delaying their market entry. In order to drive their cost down, their durability must be improved and system complexity needs to be reduced. The work presented in this dissertation addresses these two challenges by the prevention of chromium poisoning of the cathode, by demonstrating the possibility to decrease the complexity of the fuel processing subsystem and by the development of a performant and durable type of seal.

Chromium poisoning of the cathode causes a degradation of its performance and it is seen as a major issue limiting the durability of SOFC. A protective coating solution was developed to limit chromium transport from the stainless steel interconnect to the cathode and by the development of a method to quantify the amount of chromium species originating from BoP components.

Protective $MnCo_2O_4$ and $MnCo_{1.8}Fe_{0.2}O_4$ coatings were manufactured on SOFC interconnect steel by High Velocity Oxy Fuel spraying coating. The coating effectively reduced the oxidation rate of the steel substrate in a high-temperature exposure test. The ASR was measured from coated samples and showed that the ASR did not exhibit degradation during the 1000 h test at 700 °C. The suitability of the coating solution was further assessed by performing a post-experimental analysis of a single-cell stack with a coated interconnect that was operated for 6000 h. It confirmed that the coating effectively reduced the oxidation of the interconnect and that the coating did not exhibit cracks or open porosity. Additionally, chromium could not be detected in the coating, suggesting that the chromium diffusion through the coating was sufficiently low. A low concentration of chromium was detected in the SOFC cathode. However, the uncoated steel manifold and piping upstream of the stack are also known to be a source of volatile chromium and are likely to be the source of the chromium found in the cathode. Overall, the coating developed is promising in terms of improving the durability of SOFC stacks by preventing interconnect oxidation and chromium poisoning of the cathode. The suitability of the coating should be further assessed in accelerated ageing stack tests with humidified air because humidity is known to increase the evaporation rate of chromium from stainless steel [91]. Additionally, electrochemical imped-

ance spectroscopy should be performed during future stack tests to follow the different contributions to the ASR behaviour during ageing. Obviously, adding any type of coating increases the cost associated with the SOFC stack, but coatings that effectively reduces oxidation of the steel allow the use of cheaper grade steel such as AISI441 (EN 1.4509) [132]. Using a cheaper grade of steel is likely to offset the cost associated with the coating to some extent.

The findings of Publication I suggested that the stainless steel components upstream of the cathode are a potential source of volatile chromium. To gain insight into this contamination source, a method for quantifying chromium evaporation from BoP component was developed and evaluated on a stainless steel pipe in Publication II. The principle of the method is to collect volatile chromium species by sampling hot air directly from a BoP component through a denuder tube coated with sodium carbonate. The chromium species react with the sodium carbonate coating, which is then dissolved and its chromium content analysed by ICP-MS.

The developed method proved to be an effective tool because its results were found to be coherent with thermodynamics data from the literature and it yielded repeatable results. These results confirmed that stainless steel BoP components are a source of volatile chromium that can poison the cathode of SOFC. Therefore, future research should address the issue of reducing chromium transport from the hot stainless steel BoP component to the cathode. The experimental setup is designed in a way that enables its implementation after a BoP component, such as a heat exchanger or at various places within an SOFC system. This makes the assessment of local chromium concentration possible at the stack air inlet or outlet. Therefore, the method enables identification of the major chromium sources of the system that can contaminate the SOFC cathode and is a tool for assessing the effectiveness of solutions such as protective coatings, surface treatments, chromium trap, and material selection to mitigate chromium transport from BoP components to the cathode.

Two simplifications of the fuel subsystem are proposed in this dissertation. The first is to eliminate the external water supply during SOFC operation. A steam supply is needed for the steam reforming reaction taking place in the fuel processing subsystem. The steam can either be supplied externally, which requires a water inlet and an evaporator or it can be supplied by recycling the steam-rich anode off-gas, which simplifies the system. Recycling the anode off-gas has been extensively studied because it can also improve electrical efficiency of SOFC system, but most of the publications focus on simulation work. However, using anode off-gas recycling increases the risk of carbon formation in the pre-reformer at low recycling ratios and its effect on the activity of a precious metal catalyst has not been published in the literature before Publication III. In Publication III, a commercial precious metal catalyst was tested in steam reforming conditions and in simulated anode off-gas recycling (AOGR) conditions. It was found that the catalyst is more active in AOGR mode for the evaluated conditions, therefore the prereformer dimension can be reduced if AOGR is used in a system instead of supplying the water externally. Additionally, long-term tests demonstrated that the tested catalyst did not form carbon to an extent that would threaten SOFC system

operation in AOGR conditions. The results of this study demonstrated that the tested pre-reformer can be used in a system with an AOGR loop. Based on these results, an AOGR loop was successfully implemented in a 10 kW demonstration SOFC system. The system relied solely on AOGR to provide the necessary steam for natural gas reforming and no external water was used at nominal conditions. In the future, additional kinetics analysis could be performed to understand the observed difference in catalyst activity in steam reforming and AOGR conditions. The experiments presented in this dissertation were using grid natural gas and in Finland, its higher hydrocarbon content (ethane and propane) is particularly low. Therefore, supplementary experiments could be conducted with natural gas containing more higher hydrocarbon in order to investigate the conversion of ethane and propane by the developed pre-reformer.

The second system simplification proposed is to heat up an SOFC system by using the pre-reformer to generate hydrogen-containing protective gas. The protective gas is needed to prevent the nickel of the anode from reoxidising, which is detrimental for the SOFC stack durability. The reducing protective gas is often provided from cylinders of premixed hydrogen and nitrogen. However, the premixed gas cylinders increase the system size and their replacement adds up to the maintenance cost of the system, therefore it would be beneficial to generate the hydrogen-containing gas with the pre-reformer during heat-up.

The activity of the pre-reformer catalyst at temperatures as low as 200 °C was tested for the steam reforming reaction. It was found that the catalyst had measurable activity below 250 °C, but if oxygen originating from leakage was present, the reaction was inhibited below ca. 400 °C. However, the oxygen could be consumed by the addition of hydrogen at temperatures as low as 200 °C. These results were used to develop a heat-up procedure for a 10 kW SOFC system including a pre-reformer and an AOGR loop. The pre-reformer was used for two purposes: firstly, to remove molecular oxygen from the fuel side by the catalytic combustion of a small feed of hydrogen and secondly, to provide a reducing atmosphere to the SOFC anode by reforming a small fraction of the natural gas feed. The difference of the cell voltage before and after the heat-up procedure did not reveal any performance degradation. Therefore, it was considered that the heat-up procedure fulfilled its requirements and it allows for a reduction of the system size and its complexity by making the premixed gas cylinders unnecessary for heat-up. At the time of writing, no experimental work describing the heat-up of a planar SOFC system with AOGR had been published previously.

The results showed that a steam generator and a water feed are not needed during operation, i.e. when current is drawn from the stack. However, the heat-up procedure presented in this work relies on a steam feed for the steam reforming of the natural gas. Therefore, future research should focus on the development of a procedure to generate the hydrogen-containing protective gas without the need for a steam feed. For this purpose, the use of catalytic partial oxidation of natural gas is suggested.

A method for producing hybrid seals consisting of a compressible core coated with compliant glass was presented in Publication V. The aim of this development was to achieve low leak rate at low compression stresses. The novelty of the hybrid seals investigated in this dissertation is in the core material chosen that contains a steatite filler between vermiculite platelets, which results in improved gas tightness and superior compressibility. The developed solution exhibited a leak rate of about 0.4 ml (min m)$^{-1}$ at 20 mbar pressure difference using a compressive stress of 0.1 MPa. This is an 85% reduction compared to uncoated Thermiculite 866. The leak rate performance of the developed seal was considered very promising. The coated Thermiculite 866 could be handled in exactly the same way as uncoated gasket, thus enabling a simple stack assembling method. Using the developed hybrid seals instead of compressive seals allows a significant reduction in the compression need on the stack, which enables the simplification of the stack compression system.

While the leak rate performance of the developed hybrid seal makes it an attractive sealing solution, the durability of the SOFC stack requires limited material interactions between the materials of the hybrid seals and other stack components during operation. For this purpose, a post-experimental analysis was performed on a stack using hybrid seals after 1800 h of operation (Publication VI). Different locations inside the stack were investigated. No corrosion could be found at the two-phase interfaces such as Crofer/glass, glass/electrolyte and glass/Thermiculite 866. The three-phase interfaces between Crofer/glass/hydrogen exhibited no corrosion, whereas interfaces corresponding to Crofer/glass/air exhibited some non-systematic corrosion. The possible reasons for the corrosion discovered were discussed and the most likely was the contamination from lubricant that was not properly removed during stack assembly.

The developed hybrid seal can be used together with the coated interconnect used in Publication I. However the coating should only be applied where it will be exposed to oxidative atmosphere (cathode side). The reason for that is that the reductive atmosphere of the anode is likely to reduce the coating to its metallic form and to make it porous.

Further research should focus on validating the hypothesis concerning the corrosion found near the hybrid seals in air atmosphere. Additionally, the long-term suitability of the hybrid seal materials should be investigated either in longer-term stack tests or by using accelerated ageing conditions such as increasing the air humidity content to 1…3%. Moreover, tests should be performed to compare the durability of glass and hybrid seals after numerous thermal cycles as it is known that thermal cycling is more critical towards durability than steady conditions.

The performance of the developed seal are very promising in terms of leak rate and material compatibility and the results presented in this section led to the commercialisation of the developed seal by Flexitallic under the brand “Thermiculite 866 LS”, which is a glass-coated version of the Thermiculite 866 product [1,133].

SOFCs have demonstrated very good performance in terms of electrical efficiency, which makes them a promising technology for the power generation sector. At the same time, SOFCs need to show rapid technological progress towards commercialization in order to sustain investment in research and development effort. The main obstacle is their high cost: SOFC stacks are expensive and their lifetime is limited due to degradation. Additionally, system BoP components are costly, because many of these components are not found off-the-shelf or produced in small series. There is no doubt that costs will be decreased by economies of scale when SOFCs are mass produced. However, scientific research has a key role to play in reducing the cost of SOFCs. Important topics are cost-effective solutions to improve SOFC durability. In the field of interconnect, coating methods suitable for mass production should be investigated. Additionally, the protective coating should enable using standard ferritic stainless steel grades that are much cheaper than alloys specifically design for SOFCs. An example of such progress is the roll-to-roll coating method of Sandvik [134]. On the system level, BoP components development include the integration of the catalytic reactor and the heat exchanger. For example, Lee et al. presented the development of a heat exchanger, with channels catalytically active for steam reforming and others for afterburner of the anode off-gas [135]. Other simplifications concern the instrumentation of the system. For example, stack temperature is difficult to measure. However, the maximum stack temperature could be estimated by accurate data-based models, making direct measurement unnecessary [136].

References

[1] Flexitallic Ltd., Thermiculite ® 866 / 866 LS, 2014, Last accessed 08.01.2015 2015, http://www.flexitallicsofc.com/downloads/thermiculite866.pdf.

[2] Intergouvernmental panel on climate change - IPCC, Fifth Assessment Report (AR5), Cambridge University Press, Cambridge, United Kingdom and New York, NY, USA, 2014.

[3] European Environment Agency, Annual European Union Greenhouse Gas Inventory 1990–2012 and Inventory Report 2014, Publications Office of the European Union, Luxembourg, 2014.

[4] European Environment Agency, EEA Greenhouse gas - Data viewer, 2015, Last accessed 16.01 2015, http://www.eea.europa.eu/data-and-maps/data/data-viewers/greenhouse-gases-viewer.

[5] P. Capros, A. De Vita, N. Tasios, D. Papadopoulos, P. Siskos, E. Apostolaki, M. Zampara, L. Paroussos, K. Fragiadakis, N. Kouvaritakis, L. Höglund-Isaksson, W. Winiwarter, P. Purohit, H. Böttcher, S. Frank, P. Havlik, M. Gusti, H.P. Witzke, EU Energy, Transport and GHG Emissions, Trends to 2050. Publications office of the European Union, Luxembourg, 2013.

[6] L. Chick, M. Weimar, G. Whyatt, M. Powell, The Case for Natural Gas Fueled Solid Oxide Fuel Cell Power Systems for Distributed Generation, Fuel Cells. 15.1 (2015) 49-60.

[7] S.C. Singhal, Solid oxide fuel cells for stationary, mobile, and military applications, Solid State Ionics. 152-153 (2002) 405-410.

[8] R. Payne, J. Love, M. Kah, Generating Electricity at 60% Electrical Efficiency from 1-2 kWe SOFC Products, ECS Trans. 25 (2009) 231-239.

[9] K. Sasaki, K. Watanabe, K. Shiosaki, K. Susuki, Y. Teraoka, Multi-fuel capability of solid oxide fuel cells, J Electroceram. 13 (2004) 669-675.

[10] K. Eguchi, H. Kojo, T. Takeguchi, R. Kikuchi, K. Sasaki, Fuel flexibility in power generation by solid oxide fuel cells, Solid State Ionics. 152-153 (2002) 411-416.

[11] G. Gahleitner, Hydrogen from renewable electricity: An international review of power-to-gas pilot plants for stationary applications, Int J Hydrogen Energy. 38 (2013) 2039-2061.

[12] E4tech, The Fuel Cell Industry Review 2014, Lausanne, Switzerland, 2014.

[13] Fuel cell and hydrogen joint undertaking (FCH JU), Multi Annual Implementation Plan 2008-2013. 2011.

[14] H. Yokokawa, H. Tu, B. Iwanschitz, A. Mai, Fundamental mechanisms limiting solid oxide fuel cell durability, J. Power Sources. 182 (2008) 400-412.

[15] R.M. Ormerod, Solid oxide fuel cells, Chem. Soc. Rev. 32 (2003) 17-28.

[16] S.J. Skinner, Recent advances in Perovskite-type materials for solid oxide fuel cell cathodes, International Journal of Inorganic Materials. 3 (2001) 113-121.

[17] D.J.L. Brett, A. Atkinson, N.P. Brandon, S.J. Skinner, Intermediate temperature solid oxide fuel cells, Chem. Soc. Rev. 37 (2008) 1568-1578.

[18] E. Konysheva, H. Penkalla, E. Wessel, J. Mertens, U. Seeling, L. Singheiser, K. Hilpert, Chromium poisoning of perovskite cathodes by the ODS alloy Cr5Fe1 Y2 O3 and the high chromium ferritic steel Crofer22APU, J. Electrochem. Soc. 153 (2006) A765-A773.

[19] K. Hilpert, D. Das, M. Miller, D.H. Peck, R. Weiß, Chromium vapor species over solid oxide fuel cell interconnect materials and their potential for degradation processes, J. Electrochem. Soc. 143 (1996) 3642-3647.

[20] J. Wu, X. Liu, Recent Development of SOFC Metallic Interconnect, J. Mater. Sci. Technol. 26 (2010) 293-305.

[21] J.W. Fergus, Metallic interconnects for solid oxide fuel cells, Materials Science and Engineering A. 397 (2005) 271-283.

[22] W.Z. Zhu, S.C. Deevi, Development of interconnect materials for solid oxide fuel cells, Mater. Sci. Eng. A. 348 (2003) 227-243.

[23] N. Shaigan, W. Qu, D.G. Ivey, W. Chen, A review of recent progress in coatings, surface modifications and alloy developments for solid oxide fuel cell ferritic stainless steel interconnects, J. Power Sources. 195 (2010) 1529-1542.

[24] Z. Yang, K.S. Weil, D.M. Paxton, J.W. Stevenson, Selection and Evaluation of Heat-Resistant Alloys for SOFC Interconnect Applications, J. Electrochem. Soc. 150 (2003).

[25] P.D. Jablonski, C.J. Cowen, J.S. Sears, Exploration of alloy 441 chemistry for solid oxide fuel cell interconnect application, J. Power Sources. 195 (2010) 813-820.

[26] Y. Chou, J.W. Stevenson, J. Choi, Long-term evaluation of solid oxide fuel cell candidate materials in a 3-cell generic stack test fixture, part III: Stability and mi-

crostructure of Ce-(Mn,Co)-spinel coating, AISI441 interconnect, alumina coating, cathode and anode, J. Power Sources. 257 (2014) 444-453.

[27] Z. Yang, G.-G. Xia, C.-M. Wang, Z. Nie, J. Templeton, J.W. Stevenson, P. Singh, Investigation of iron-chromium-niobium-titanium ferritic stainless steel for solid oxide fuel cell interconnect applications, J. Power Sources. 183 (2008) 660-667.

[28] M.W. Lundberg, R. Berger, J. Westlinder, N. Folkeson, H. Holmberg, Novel multilayered PVD-coating in a roll to roll mass production process, ECS Transactions. 57 (2013) 2203-2208.

[29] J.W. Stevenson, Z.G. Yang, G.G. Xia, Z. Nie, J.D. Templeton, Long-term oxidation behavior of spinel-coated ferritic stainless steel for solid oxide fuel cell interconnect applications, J. Power Sources. 231 (2013) 256-263.

[30] J.W. Fergus, Sealants for solid oxide fuel cells, J. Power Sources. 147 (2005) 46-57.

[31] K. Weil, The state-of-the-art in sealing technology for solid oxide fuel cells, JOM. 58 (2006) 37-44.

[32] Z. Wuillemin, N. Autissier, M. Nakajo, M. Luong, J. Van Herle, D. Favrat, Modeling and study of the influence of sealing on a solid oxide fuel cell, J. Fuel Cell Sci. Technol. 5 (2008).

[33] Y. Chou, J.W. Stevenson, R.N. Gow, Novel alkaline earth silicate sealing glass for SOFC: Part II. Sealing and interfacial microstructure, J. Power Sources. 170 (2007) 395-400.

[34] A. Shyam, R. Trejo, D. McClurg, A. Ladouceur, M. Kirkham, X. Song, J. Howe, E. Lara-Curzio, Microstructural evolution in two alkali multicomponent silicate glasses as a result of long-term exposure to solid oxide fuel cell environments, J. Mater. Sci. 48 (2013) 5880-5898.

[35] M. Rautanen, O. Himanen, V. Saarinen, J. Kiviaho, Compression properties and leakage tests of mica-based seals for SOFC stacks, Fuel Cells. 9 (2009) 753-759.

[36] S.P. Simner, J.W. Stevenson, Compressive mica seals for SOFC applications, J. Power Sources. 102 (2001) 310-316.

[37] Y.-S. Chou, J.W. Stevenson, L.A. Chick, Ultra-low leak rate of hybrid compressive mica seals for solid oxide fuel cells, J. Power Sources. 112 (2002) 130-136.

[38] Y.-S. Chou, J.W. Stevenson, L.A. Chick, Novel compressive mica seals with metallic interlayers for solid oxide fuel cell applications, J Am Ceram Soc. 86 (2003) 1003-1007.

[39] D. Mogensen, J.-D. Grunwaldt, P.V. Hendriksen, K. Dam-Johansen, J.U. Nielsen, Internal steam reforming in solid oxide fuel cells: Status and opportunities of kinetic studies and their impact on modelling, J. Power Sources. 196 (2011) 25-38.

[40] Y. Yi, A.D. Rao, J. Brouwer, G.S. Samuelsen, Fuel flexibility study of an integrated 25 kW SOFC reformer system, J. Power Sources. 144 (2005) 67-76.

[41] S.L. Douvartzides, F.A. Coutelieris, A.K. Demin, P.E. Tsiakaras, Fuel options for solid oxide fuel cells: A thermodynamic analysis, AIChE J. 49 (2003) 248-257.

[42] R.-U. Dietrich, J. Oelze, A. Lindermeir, C. Spieker, C. Spitta, M. Steffen, Power generation from biogas using SOFC - Results for a 1kWe demonstration unit, Fuel Cells. 14 (2014) 239-250.

[43] M. Halinen, M. Rautanen, J. Saarinen, J. Pennanen, A. Pohjoranta, J. Kiviaho, M. Pastula, B. Nuttall, C. Rankin, B. Borglum, Performance of a 10 kW SOFC Demonstration Unit, ECS Transactions. 35 (2011) 113-120.

[44] K. Ahmed, J. Gamman, K. Föger, Demonstration of LPG-fueled solid oxide fuel cell systems, Solid State Ionics. 152-153 (2002) 485-492.

[45] Y. Du, D. Cui, K. Reifsnider, Characterization of propane-fueled SOFC portable power systems, ECS Transactions. 35 (2011) 167-178.

[46] P. Leone, A. Lanzini, G.A. Ortigoza-Villalba, R. Borchiellini, Operation of a solid oxide fuel cell under direct internal reforming of liquid fuels, Chem. Eng. J. 191 (2012) 349-355.

[47] M. Rautanen, M. Halinen, M. Noponen, K. Koskela, H. Vesala, J. Kiviaho, Experimental study of an SOFC stack operated with autothermally reformed diesel fuel, Fuel Cells. 13 (2013) 304-308.

[48] D. Shekhawat, D.A. Berry, J.J. Spivey, Fuel Cells: Technologies for Fuel Processing, Elsevier Ltd., Oxford, UK, 2011.

[49] Union Gas, Chemical Composition of Natural Gas, 2015, Last accessed 01.22 2015, http://www.uniongas.com/about-us/about-natural-gas/Chemical-Composition-of-Natural-Gas.

[50] Energinet.dk, Vis gaskvalitet, 2013, Last accessed 01.22 2015, http://energinet.dk/DA/GAS/Gasdata-og-kvalitet/Gaskvalitet/Sider/Vis-gaskvalitet.aspx?Visning=aarsgennemsnit.

[51] Gasum Oy, Natural Gas Composition Yearly Report, 2012.

[52] R. Peters, R. Dahl, U. Klüttgen, C. Palm, D. Stolten, Internal reforming of methane in solid oxide fuel cell systems, J. Power Sources. 106 (2002) 238-244.

[53] S. McIntosh, R.J. Gorte, Direct hydrocarbon solid oxide fuel cells, Chem. Rev. 104 (2004) 4845-4865.

[54] J.N. Armor, The multiple roles for catalysis in the production of H2, Applied Catalysis A: General. 176 (1999) 159-176.

[55] L. Blum, E. Riensche, FUEL CELLS – SOLID OXIDE FUEL CELLS | Systems, in: J. Garche (Ed.), Encyclopedia of Electrochemical Power Sources, Elsevier, Amsterdam, 2009, pp. 99-119.

[56] P. Gannon, R. Amendola, High-temperature, dual-atmosphere corrosion of solid-oxide fuel cell interconnects, JOM. 64 (2012) 1470-1476.

[57] H. Tu, U. Stimming, Advances, aging mechanisms and lifetime in solid-oxide fuel cells, J. Power Sources. 127 (2004) 284-293.

[58] M. Stanislowski, E. Wessel, K. Hilpert, T. Markus, L. Singheiser, Chromium vaporization from high-temperature alloys, J. Electrochem. Soc. 154 (2007).

[59] M.C. Tucker, H. Kurokawa, C.P. Jacobson, L.C. De Jonghe, S.J. Visco, A fundamental study of chromium deposition on solid oxide fuel cell cathode materials, J. Power Sources. 160 (2006) 130-138.

[60] J.A. Schuler, H. Yokokawa, C.F. Calderone, Q. Jeangros, Z. Wuillemin, A. Hessler-Wyser, J. Van Herle, Combined Cr and S poisoning in solid oxide fuel cell cathodes, J. Power Sources. 201 (2012) 112-120.

[61] J.W. Fergus, Effect of cathode and electrolyte transport properties on chromium poisoning in solid oxide fuel cells, Int J Hydrogen Energy. 32 (2007) 3664-3671.

[62] N.H. Menzler, P. Batfalsky, L. Blum, M. Bram, S.M. Groß, V.A.C. Haanappel, J. Malzbender, V. Shemet, R.W. Steinbrech, I. Vinke, Studies of material interaction after long-term stack operation, Fuel Cells. 7 (2007) 356-363.

[63] Y. Larring, T. Norby, Spinel and perovskite functional layers between Plansee metallic interconnect (Cr-5 wt % Fe-1 wt % Y2O3) and ceramic (La0.85Sr0.15)0.91MnO3 cathode materials for solid oxide fuel cells, J. Electrochem. Soc. 147 (2000) 3251-3256.

[64] J.W. Fergus, Synergism in the design of interconnect alloy–coating combinations solid for oxide fuel cells, Scr. Mater. 65 (2011) 73-77.

[65] X. Montero, N. Jordán, J. Pirón-Abellán, F. Tietz, D. Stöver, M. Cassir, I. Villarreal, Spinel and perovskite protection layers between crofer22APU and La 0.8Sr0.2FeO3 cathode materials for SOFC interconnects, J. Electrochem. Soc. 156 (2009) B188-B196.

[66] J. Puranen, J. Lagerbom, L. Hyvärinen, M. Kylmälahti, O. Himanen, M. Pihlatie, J. Kiviaho, P. Vuoristo, The structure and properties of plasma sprayed iron oxide doped manganese cobalt oxide spinel coatings for SOFC metallic interconnectors, J. Therm. Spray Technol. 20 (2011) 154-159.

[67] X. Chen, P.Y. Hou, C.P. Jacobson, S.J. Visco, L.C. De Jonghe, Protective coating on stainless steel interconnect for SOFCs: oxidation kinetics and electrical properties, Solid State Ionics. 176 (2005) 425-433.

[68] Z. Yang, G. Xia, G.D. Maupin, J.W. Stevenson, Conductive protection layers on oxidation resistant alloys for SOFC interconnect applications, Surf. Coat. Technol. 201 (2006) 4476-4483.

[69] A. Balland, P. Gannon, M. Deibert, S. Chevalier, G. Caboche, S. Fontana, Investigation of La2O3 and/or (Co,Mn)3O4 deposits on Crofer22APU for the SOFC interconnect application, Surf. Coat. Technol. 203 (2009) 3291-3296.

[70] Y. Fang, C. Wu, X. Duan, S. Wang, Y. Chen, High-temperature oxidation process analysis of MnCo2O4 coating on Fe–21Cr alloy, Int J Hydrogen Energy. 36 (2011) 5611-5616.

[71] J. Puranen, J. Lagerbom, L. Hyvärinen, T. Mäntylä, E. Levänen, M. Kylmälahti, P. Vuoristo, Formation and structure of plasma sprayed manganese-cobalt spinel coatings on preheated metallic interconnector plates, Surf. Coat. Technol. 205 (2010) 1029-1033.

[72] K. Uusi-Esko, E.-L. Rautama, M. Laitinen, T. Sajavaara, M. Karppinen, Control of oxygen nonstoichiometry and magnetic property of MnCo 2O 4 thin films grown by atomic layer deposition, Chem. Mater. 22 (2010) 6297-6300.

[73] L. Mikkelsen, M. Chen, P.V. Hendriksen, Å. Persson, N. Pryds, K. Rodrigo, Deposition of La0.8Sr0.2Cr0.97V0.03O3 and MnCr2O4 thin films on ferritic alloy for solid oxide fuel cell application, Surf. Coat. Technol. 202 (2007) 1262-1266.

[74] M.J. Lewis, J.H. Zhu, A process to synthesize (Mn,Co) 3 O 4 spinel coatings for protecting SOFC interconnect alloys, Electrochem. Solid-State Lett. 14 (2011) B9-B12.

[75] V.I. Gorokhovsky, P.E. Gannon, M.C. Deibert, R.J. Smith, A. Kayani, M. Kopczyk, D. Vanvorous, Z. Yang, J.W. Stevenson, S. Visco, C. Jacobson, H. Kurokawa, S.W. Sofie, Deposition and evaluation of protective PVD coatings on ferritic stainless steel SOFC interconnects, J. Electrochem. Soc. 153 (2006) A1886-A1893.

[76] L. Pawlowski, Thermal Spraying Techniques, The Science and Engineering of Thermal Spray Coatings, John Wiley & Sons, Ltd, 2008, pp. 67-113.

[77] Z. Yang, G.-G. Xia, X.-H. Li, J.W. Stevenson, (Mn,Co)3O4 spinel coatings on ferritic stainless steels for SOFC interconnect applications, Int J Hydrogen Energy. 32 (2007) 3648-3654.

[78] L. Mikkelsen, K. Neufeld, P.V. Hendriksen, Interface Resistance Between FeCr Interconnects and La0.85Sr0.15Mn1,1O3, ECS Transactions. 25 (2009) 1429.

[79] Z. Yang, J.S. Hardy, M.S. Walker, G. Xia, S.P. Simner, J.W. Stevenson, Structure and conductivity of thermally grown scales on ferritic Fe-Cr-Mn steel for SOFC interconnect applications, J. Electrochem. Soc. 151 (2004) A1825-A1831.

[80] J.A. Schuler, Z. Wuillemin, A. Hessler-Wyser, C. Comminges, N.Y. Steiner, J. Van Herle, Cr-poisoning in (La,Sr)(Co,Fe)O 3 cathodes after 10,000 h SOFC stack testing, J. Power Sources. 211 (2012) 177-183.

[81] O. Thomann, M. Pihlatie, J.A. Schuler, O. Himanen, J. Kiviaho, Method for measuring chromium evaporation from SOFC balance-of-plant components, Electrochem. Solid-State Lett. 15 (2012) B35-B37.

[82] Z. Wuillemin, N. Nakajoa, A. Müllera, A. Schuler, S. Diethelm, J. Van herle, D. Favrat, Locally-resolved study of degradation in a SOFC, ECS Trans. 25 (2009) 457-466.

[83] J.A. Schuler, C. Gehrig, Z. Wuillemin, A.J. Schuler, J. Wochele, C. Ludwig, A. Hessler-Wyser, J. Van Herle, Air side contamination in Solid Oxide Fuel Cell stack testing, J. Power Sources. 196 (2011) 7225-7231.

[84] K. Gerdes, C. Johnson, Surface Scale Formation on Solid Oxide Fuel Cell Proximal Balance of Plant Components, Journal of Fuel Cell Sci. & Tech. vol. 6 (2009).

[85] M. Stanislowski, E. Wessel, T. Markus, L. Singheiser, W.J. Quadakkers, Chromium vaporization from alumina-forming and aluminized alloys, Solid State Ionics. 179 (2008) 2406-2415.

[86] D. Chatterjee, S. Biswas, Development of chromium barrier coatings for solid oxide fuel cells, Int J Hydrogen Energy. 36 (2011) 4530-4539.

[87] J.A. Schuler, A.J. Schuler, D. Penner, A. Hessler-Wyser, C. Ludwig, J. Van Herle, Mitigating Cr Contamination by Hot Air Filtering in Solid Oxide Fuel Cells, Electrochemical and Solid-State Letters. 14 (2011).

[88] C. Key, J. Eziashi, J. Froitzheim, R. Amendola, R. Smith, P. Gannon, Methods to Quantify Reactive Chromium Vaporization from Solid Oxide Fuel Cell Interconnects, Journal of The Electrochemical Society. 161 (2014) C373-C381.

[89] J. Froitzheim, H. Ravash, E. Larsson, L.G. Johansson, J.E. Svensson, Investigation of chromium volatilization from FeCr interconnects by a denuder technique, J. Electrochem. Soc. 157 (2010) B1295-B1300.

[90] M. Casteel, P. Willson, T. Goren, P. O'Brien, D. Lewis, Novel Method for Measuring Chromia Evaporation from SOFC Interconnect Materials, ECS Trans. 25 (2009) 1423.

[91] C. Gindorf, L. Singheiser, K. Hilpert, Vaporisation of chromia in humid air, J. Phys. Chem. Solids. 66 (2005) 384-387.

[92] Outotec, HSC Chemistry, 6.12 (2007).

[93] Sandvik, Sandvik 253MA, Last accessed 11/16 2011, http://www.smt.sandvik.com/en/materials-center/material-datasheets/tube-and-pipe-seamless/sandvik-253-ma/.

[94] E. Riensche, J. Meusinger, U. Stimming, G. Unverzagt, Optimization of a 200 kW SOFC cogeneration power plant. Part II: Variation of the flowsheet, J. Power Sources. 71 (1998) 306-314.

[95] R.-U. Dietrich, J. Oelze, A. Lindermeir, C. Spitta, M. Steffen, T. Küster, S. Chen, C. Schlitzberger, R. Leithner, Efficiency gain of solid oxide fuel cell systems by using anode offgas recycle - Results for a small scale propane driven unit, J. Power Sources. 196 (2011) 7152-7160.

[96] M. Noponen, M. Halinen, J. Saarinen, J. Kiviaho, Experimental study of anode gas recycling on efficiency of SOFC, ECS Transactions. 5 (2007) 545-551.

[97] D. Larrain, J. Van herle, D. Favrat, Simulation of SOFC stack and repeat elements including interconnect degradation and anode reoxidation risk, J. Power Sources. 161 (2006) 392-403.

[98] M.P. Heddrich, M. Jahn, A. Michaelis, R. Näke, A. Weder, SOFC system design using ideal efficiency modeling - Model and experimental implementation, Fuel Cells. 13 (2013) 612-622.

[99] R. Peters, E. Riensche, P. Cremer, Pre-reforming of natural gas in solid oxide fuel-cell systems, J. Power Sources. 86 (2000) 432-441.

[100] A. Nummela, M. Noponen, Experimental Study on Effects of Anode Recirculation to Pre-Reforming of Natural Gas, European Fuel Cell Forum. B0301 (2009).

[101] D.G. Goodwin, An open-source, extensible software suite for CVD process simulation, In Proceedings of CVD XVI and EuroCVD 14, M. Allendorf, F. Maury, and E. Teyssandier, Eds, PV 2003-2008.

[102] G.P. Smith, GRI-MECH 3.0, 2009, Last accessed 03.04 2015, http://combustion.berkeley.edu/gri-mech/.

[103] A. Selimovic, M. Kemm, T. Torisson, M. Assadi, Steady state and transient thermal stress analysis in planar solid oxide fuel cells, J. Power Sources. 145 (2005) 463-469.

[104] M. Pihlatie, T. Ramos, A. Kaiser, Testing and improving the redox stability of Ni-based solid oxide fuel cells, J. Power Sources. 193 (2009) 322-330.

[105] A. Wood, M. Pastula, D. Waldbilig, D.G. Ivey, Initial testing of solutions to redox problems with anode-supported SOFC, J. Electrochem. Soc. 153 (2006) A1929-A1934.

[106] Q. Jeangros, A. Faes, J.B. Wagner, T.W. Hansen, U. Aschauer, J. Van herle, A. Hessler-Wyser, R.E. Dunin-Borkowski, In situ redox cycle of a nickel–YSZ fuel cell anode in an environmental transmission electron microscope, Acta Materialia. 58 (2010) 4578-4589.

[107] M. Pihlatie, A. Kaiser, M. Mogensen, Redox stability of SOFC: Thermal analysis of Ni-YSZ composites, Solid State Ionics. 180 (2009) 1100-1112.

[108] J.F.B. Rasmussen, P.V. Hendriksen, A. Hagen, Study of internal and external leaks in tests of anode-supported SOFCs, Fuel Cells. 8 (2008) 385-393.

[109] R. Peters, R. Deja, L. Blum, J. Pennanen, J. Kiviaho, T. Hakala, Analysis of solid oxide fuel cell system concepts with anode recycling, Int J Hydrogen Energy. 38 (2013) 6809-6820.

[110] Guidechem.com, Nickel carbonyl(Ni(CO)4), (cas 13463-39-3) msds, 2014, Last accessed 11/21 2014, http://www.guidechem.com/msds/13463-39-3.html.

[111] Matheson Tri Gas, Material safety data sheet nickel carbonyl, 2008, Last accessed 03.04 2015, https://www.mathesongas.com/pdfs/msds/MAT16290.pdf.

[112] L. Petruzzi, S. Cocchi, F. Fineschi, A global thermo-electrochemical model for SOFC systems design and engineering, J. Power Sources. 118 (2003) 96-107.

[113] H. Apfel, M. Rzepka, H. Tu, U. Stimming, Thermal start-up behaviour and thermal management of SOFC's, J. Power Sources. 154 (2006) 370-378.

[114] D.L. Damm, A.G. Fedorov, Reduced-order transient thermal modeling for SOFC heating and cooling, J. Power Sources. 159 (2006) 956-967.

[115] B. Borglum, E. Tang, M. Pastula, Development of solid oxide fuel cells at versa power systems, ECS Transactions. 35 (2011) 63-69.

[116] Y.-S. Chou, J.W. Stevenson, Compressive mica seals for solid oxide fuel cells, ASM Conference Proceedings: Joining of Advanced and Specialty Materials. (2005) 132-139.

[117] M. Bram, S. Reckers, P. Drinovac, J. Mönch, R.W. Steinbrech, H.P. Buchkremer, D. Stöver, Deformation behavior and leakage tests of alternate sealing materials for SOFC stacks, J. Power Sources. 138 (2004) 111-119.

[118] Y.-S. Chou, J.W. Stevenson, L.A. Chick, Ultra-low leak rate of hybrid compressive mica seals for solid oxide fuel cells, J. Power Sources. 112 (2002) 130-136.

[119] Y.-S. Chou, J.W. Stevenson, L.A. Chick, Novel compressive mica seals with metallic interlayers for solid oxide fuel cell applications, J Am Ceram Soc. 86 (2003) 1003-1007.

[120] Y. Chou, J.W. Stevenson, Long-term ageing and materials degradation of hybrid mica compressive seals for solid oxide fuel cells, J. Power Sources. 191 (2009) 384-389.

[121] Y.-S. Chou, J.W. Stevenson, Infiltrated phlogopite micas with superior thermal cycle stability as compressive seals for solid oxide fuel cells, Ceramic Transactions. 161 (2005) 89-98.

[122] Y.-S. Chou, J.W. Stevenson, J. Hardy, P. Singh, Material degradation during isothermal ageing and thermal cycling of hybrid mica seals under solid oxide fuel cell exposure conditions, J. Power Sources. 157 (2006) 260-270.

[123] Y.-S. Chou, J.W. Stevenson, Novel infiltrated Phlogopite mica compressive seals for solid oxide fuel cells, J. Power Sources. 135 (2004) 72-78.

[124] Y.-S. Chou, J.W. Stevenson, P. Singh, Thermal cycle stability of a novel glass-mica composite seal for solid oxide fuel cells: Effect of glass volume fraction and stresses, J. Power Sources. 152 (2005) 168-174.

[125] P. Batfalsky, V.A.C. Haanappel, J. Malzbender, N.H. Menzler, V. Shemet, I.C. Vinke, R.W. Steinbrech, Chemical interaction between glass–ceramic sealants and interconnect steels in SOFC stacks, J. Power Sources. 155 (2006) 128-137.

[126] F. Wiener, M. Bram, H.-P. Buchkremer, D. Sebold, Chemical interaction between Crofer 22 APU and mica-based gaskets under simulated SOFC conditions, J. Mater. Sci. 42 (2007) 2643-2651.

[127] M. Bram, L. Niewolak, N. Shah, D. Sebold, H.P. Buchkremer, Interaction of sealing material mica with interconnect steel for solid oxide fuel cells application at 600 °C, J. Power Sources. 196 (2011) 5889-5896.

[128] Y.-S. Chou, J.W. Stevenson, J.-P. Choi, Long-term evaluation of solid oxide fuel cell candidate materials in a 3-cell generic short stack fixture, Part II: Sealing glass stability, microstructure and interfacial reactions, J. Power Sources. 250 (2014) 166-173.

[129] J.R. Hoyes, S. Bond, Gaskets for sealing solid oxide fuel cells, Sealing Technology. (2007) 11-14.

[130] D. Goedeke, J. Besinger, Y. Pflügler, B. Ruedinger, New Glass Ceramic Sealants for SOFC, ECS Transactions. 25 (2009) 1483-1490.

[131] Y.-S. Chou, J.W. Stevenson, Novel infiltrated Phlogopite mica compressive seals for solid oxide fuel cells, J. Power Sources. 135 (2004) 72-78.

[132] J.G. Grolig, J. Froitzheim, J.-E. Svensson, Coated stainless steel 441 as interconnect material for solid oxide fuel cells: Oxidation performance and chromium evaporation, J. Power Sources. 248 (2014) 1007-1013.

[133] J.R. Hoyes, M. Rautanen, SOFC sealing with thermiculite 866 and thermiculite 866 LS, ECS Transactions. 57 (2013) 2365-2374.

[134] M.W. Lundberg, R. Berger, J. Westlinder, N. Folkeson, H. Holmberg, Novel multilayered PVD-coating in a roll to roll mass production process, ECS Transactions. 57 (2013) 2203-2208.

[135] K. Lee, J. Yun, K. Ahn, S. Lee, S. Kang, S. Yu, Operational characteristics of a planar steam reformer thermally coupled with a catalytic burner, Int J Hydrogen Energy. 38 (2013) 4767-4775.

[136] A. Pohjoranta, M. Halinen, J. Pennanen, J. Kiviaho, Solid oxide fuel cell stack temperature estimation with data-based modeling - Designed experiments and parameter identification, J. Power Sources. 277 (2015) 464-473.

PUBLICATION I

Development and application of HVOF sprayed spinel protective coating for SOFC interconnects

Journal of Thermal Spray Technology 2013,
Vol. 22, No. 5, pp. 631–639.

JTTEE5 22:631–639
DOI: 10.1007/s11666-012-9880-9
1059-9630/$19.00 © ASM International

Development and Application of HVOF Sprayed Spinel Protective Coating for SOFC Interconnects

O. Thomann, M. Pihlatie, M. Rautanen, O. Himanen, J. Lagerbom, M. Mäkinen, T. Varis, T. Suhonen, and J. Kiviaho

(Submitted September 27, 2012; in revised form December 7, 2012)

Protective coatings are needed for metallic interconnects used in solid oxide fuel cell (SOFC) stacks to prevent excessive high-temperature oxidation and evaporation of chromium species. These phenomena affect the lifetime of the stacks by increasing the area-specific resistance (ASR) and poisoning of the cathode. Protective $MnCo_2O_4$ and $MnCo_{1.8}Fe_{0.2}O_4$ coatings were applied on ferritic steel interconnect material (Crofer 22 APU) by high velocity oxy fuel spraying. The substrate-coating systems were tested in long-term exposure tests to investigate their high-temperature oxidation behavior. Additionally, the ASRs were measured at 700 °C for 1000 h. Finally, a real coated interconnect was used in a SOFC single-cell stack for 6000 h. Post-mortem analysis was carried out with scanning electron microscopy. The deposited coatings reduced significantly the oxidation of the metal, exhibited low and stable ASR and reduced effectively the migration of chromium.

Keywords ASR, HVOF spraying, interconnect, protective coating, SOFC, spinel, stack testing

1. Introduction

Interconnects are required in solid oxide fuel cell (SOFC) stacks to staple together an array of cells in series. Interconnects collect electrons from an anode to the cathode of the neighboring cell, and are the physical barrier between the humid reducing atmosphere on one side and the oxidizing atmosphere on the other. Since SOFCs operate typically at 600-800 °C, the requirement for high-temperature corrosion resistance is high. Additionally, interconnects are designed to ensure homogenous distribution of fuel and oxidant to their respective electrodes. Therefore, their requirements are: (i) high electrical conductivity (i.e., the area-specific resistance (ASR) should be below 100 mΩ cm^2, Ref 1), (ii) high corrosion resistance, (iii) coefficient of thermal expansion (CTE) matching those of the other components of the cell (around $10.5 \times 10^{-6}\ K^{-1}$ for yttria-stabilized zirconia electrolyte), (iv) adequate mechanical properties at elevated temperature. At the same time, it is of paramount importance that the material used and the manufacturing methods are low cost as the high cost of SOFC systems is currently impeding their market entry (Ref 1-3).

Special metallic interconnect alloys such as Crofer 22 APU (ThyssenKrupp VDM), E-Brite (Allegheny Ludlum), or ZMG (Hitachi) are widely used in SOFC stacks as they are cheap compared to ceramic interconnects. State-of-the-art ferritic stainless steel interconnect alloys typically contain 20-25 wt.% Cr to meet the requirements concerning the CTE matching, sufficient oxidation resistance and low cost (Ref 4). At operating conditions, a double oxidation layer is formed consisting of a Cr-oxide layer at the surface of the metal and a Cr-Mn spinel as top layer (Ref 5). These oxide layers prevent the metal from excessive oxidation. However, Cr-oxide growth is associated with an increase in the ASR of the interconnect and is detrimental for the electrical efficiency. The corrosion behavior of the interconnect depends on various factors such as the pre-treatment, alloy composition, operating temperature, gas composition, thickness, and shape. However, it is possible to reduce the corrosion of the interconnect by the application of protective coating (Ref 6).

Another issue with uncoated metallic interconnect is the so-called Cr-poisoning of the cathode. It is by now well established that state-of-the-art SOFC cathodes are poisoned by the volatile Cr-species evaporated from the interconnects and other stainless steel components such as system balance-of-plant components (Ref 5, 7-13). Cr reacts at the cathode current collection to form $SrCrO_4$, increasing the ohmic resistance and additionally Cr-Mn spinel formation can impair the electrochemical activity of the cathode (Ref 12). Alloys specifically designed for interconnect applications exhibit up to 75% reduction of Cr evaporation rate compared to general purpose stainless steels (Ref 5). However, further Cr evaporation rate

O. Thomann, M. Pihlatie, M. Rautanen, O. Himanen, J. Lagerbom, M. Mäkinen, T. Varis, T. Suhonen, and **J. Kiviaho**, VTT Technical Research Centre of Finland, P.O. Box 1000, Espoo 02044 VTT, Finland. Contact e-mail: olivier.thomann@vtt.fi.

reduction is needed to achieve viable stack lifetime for market entry (Ref 14). Therefore, protective coatings are seen as a solution to address the issue of Cr release and the Cr-oxide scale growth of metallic interconnects.

The protective coating requirements are: (i) full density or at least closed porosity, (ii) low diffusivity of Cr and oxygen through the coating, (iii) low ohmic resistance to maximize electrical efficiency, (iv) chemical, physical, and structural compatibility with the adjacent components, e.g., the CTE of the coating and of the substrate must match closely (Ref 1).

A wide variety of protective coatings compositions and manufacturing routes have been reported in the literature and they have recently been the subject of a large review (Ref 6). $(Mn,Co)_3O_4$ spinel coatings have received attention due to their good performance compared to other types of coatings (Ref 15). $(Mn,Co)_3O_4$ spinel coatings have been prepared by slurry spraying (Ref 16, 17), radio-frequency sputtering (Ref 17), magnetron sputtering (Ref 18, 19), plasma spraying (Ref 20), atomic layer deposition (Ref 21), pulsed laser deposition (Ref 22), electrodeposition (Ref 23), and filtered arc (Ref 24). Additionally, $MnCo_{2-x}Fe_xO_4$ has also been tried for its better electrical conductivity (Ref 25, 26). To the authors' knowledge, $(Mn,Co)_3O_4$ and $MnCo_{2-x}Fe_xO_4$ spinel coatings prepared by HVOF spraying for interconnect application have not been previously reported in scientific journals.

Coatings produced on interconnect plates by thermal spraying have been previously reported in the literature. Lim et al. (Ref 27) reported applying $La_{0.8}Sr_{0.2}MnO_3$ (LSM) coating by plasma spraying. The coating was 70-90 μm thick and the ASR was about 20 mΩ cm^2 at 800 °C after 160 h. Zhai et al. (Ref 28) also reported applying LSM coating on interconnects by plasma spraying. The ASR was measured for 2 h and was ca. 30 mΩ cm^2. Vargas et al. (Ref 29) reported using atmospheric plasma spraying to produce $MnCo_2O_4$ coating. The coating was ca. 70 μm thick and the ASR was 50 mΩ cm^2 at 800 °C after 560 h. Cr retention capability was qualitatively evaluated to be sufficient by EDS analysis. Unfortunately, Cr retention is not systematically evaluated in papers reporting protective coatings. It can be evaluated qualitatively by EDS analysis of the coating or quantitatively by the transpiration method (Ref 10, 14, 30). Coatings produced by thermal spraying typically suffer from an as-sprayed lamellar microstructure, and there is a risk of cracking of the coating due to thermal or structural stress (Ref 5, 6). To remedy these issues, optimized powders and spraying parameters can improve the coating quality and ease the risk of fragmentation. In addition to interconnect protective coatings, some stack developers make use of a cathode contact layer of, e.g., $La(Ni,Fe)O_3$ between the protective coating and the cathode of the cell, to establish a good electrical contact (Ref 31).

The development of corrosion-resistant ferritic steels has allowed to use metal plates thinner than 1 mm as interconnect plates. Reducing the thickness of the interconnect allows to use low-cost manufacturing methods such as stamping, cutting, pressing, punching, and hydroforming among others. Additionally, thinner interconnects have a potential for faster start-up by reducing the thermal mass of the stack. But reducing the thickness of the interconnect might increase the corrosion rate because of selective depletion of an alloyed element. A thin plate is more prone to deformation and thus increases the risk of crack formation through the coating.

This article deals with experimental investigations of $MnCo_2O_4$ and $MnCo_{1.8}Fe_{0.2}O_4$ spinel coatings on Crofer 22 APU steel. The aim of the article is to present the results from protective coating development; in the first place the powder manufacturing and optimized coating HVOF method is described. Then, high-temperature oxidation behavior and the ASR of coated steel samples in contact with cathode material are investigated. In order to assess the mechanical behavior of the coating on thin corrugated interconnects, 0.2 mm thin coated corrugated plates were exposed at 700 °C under mechanical load for long-term testing. Furthermore, single-cell stack using the developed coating solution has been run for 6000 h to validate the coating solution in a relevant SOFC environment. The results of the post-mortem analysis of the stack are also presented.

2. Experimental

2.1 Powder Manufacturing

The powders used to produce the spinel coatings were either acquired commercially or manufactured in-house at VTT. The $MnCo_2O_4$ powder was commercial and prepared by the fused and crushed method. $MnCo_{1.8}Fe_{0.2}O_4$ powder was manufactured in-house by solid carbonate synthesis and suitable granule size for thermal spraying was obtained by spray drying. The particle shape of the powder is typically less regular for fused and crushed powders than for spray dried powders. The powder was prepared by weighing appropriate amounts of $MnCO_2$, $CoCO_2$, and Fe_2O_3 powders together and milling for 20 h in a drum ball mill (in-house built). After milling, the mixture was calcinated at 1000 °C for 6 h to form the spinel structure. Calcination was done prior to spray drying to avoid granule breakdown due to the large volume change associated to the phase change from the carbonate to oxide. The calcinated powder was sieved to below 63 μm. The powder was then ground and dispersed in water with dispersant Dispex A40 by BASF with a Hosokava Alpine AG bead mill (Hydro Mill 90 AHM). The bead milling was continued until average particle size of 1 μm was reached. Polyvinyl alcohol (PVA 22000 by VWR) was used as a bonding agent and was added to the slurry by a dispergator mixer. The PVA addition was carried out just before spray drying to avoid PVA chain shortening during bead milling. The suspension was spray dried with a Niro pilot p6.3 spray dryer. After spray drying parameter optimization, a high rotational speed (20,000 rpm) of centrifugal nozzle was used to obtain fine granule size. The spray dryer includes a cyclone separator and the cyclone fraction was not used further because of its small average particle size and irregular particle shape.

The chamber fraction of the powder was held at 500 °C for 2 h to pyrolyze the PVA without fracturing the agglomerates. Then, sintering occurred at 1150 °C for 6 h. After sintering the powder was sieved with 32 μm sieve. The cyclone fraction was pyrolyzed to remove the PVA and added to the sieved fraction over 32 μm for crushing and recycling to the bead milling stage. The powder fraction below 32 μm was used for HVOF spraying. The powder morphology was studied with Scanning Electron Microscope (SEM, JEOL JSM-636OLV). The crystal structures of the powders and coatings were determined by x-ray diffraction (XRD) using Mo Kα radiation with Philips X'pert diffractometer.

2.2 HVOF Spraying

Commercial Crofer 22 APU steel (ThyssenKrupp) of 0.2 mm thickness was used as substrate material for test coupons. The HVOF coatings were made using a Praxair HV2000 spray gun, fitted with a 22 mm combustion chamber. Nitrogen was used as powder carrier gas (20 slpm), hydrogen as fuel and oxygen as oxidant. For all the reported coatings but one, a hydrogen flow of 700 slpm and an oxygen flow of 350 slpm were used. The $MnCo_2O_4$ coating reported in Fig. 7 was deposited with a hydrogen flow of 687 slpm and an oxygen flow of 315 slpm. The spray gun was moved by an X-Y manipulator. Prior to deposition, the substrates were grit blasted using a −36 mesh alumina grit, brushed and ultrasonically cleaned in acetone. Grit blasting was conducted on both sides to keep the thin metal sheet substrates straight. For the same reason, the coating was applied on both sides. The targeted coating thickness was 20-30 μm, which is unusually thin for thermal spraying. More details on the HVOF coating process can be obtained from Ref 32.

2.3 Exposure Tests

Exposure tests were conducted using laser cut 10 × 10-15 × 0.2 mm samples. The samples were placed standing in a furnace in alumina sample holders so that no contact between samples occurred. The samples were coated on both sides and only the edges of the samples were uncoated. The tests were conducted in air for 1000 h at 700 °C. A continuous gas flow was implemented with the incoming air bubbled through a water bottle; the resulting humidity of the air was thus ~3%. Cross-sectional samples were prepared for SEM observation.

2.4 ASR Measurements

The ASR measurements were done for two coatings ($MnCo_{1.8}Fe_{0.2}O_4$ and $MnCo_2O_4$) applied on two flat 26 × 26 × 0.2 mm steel plates separated by an initially green ceramic layer mimicking a cathode. Additionally, an uncoated steel plate was also tested as a reference. Green 20 × 20 × 1 mm $La_{0.85}Sr_{0.15}Mn_{1.1}O_3$ (LSM) spacers (IRD Fuel Cells A/S, Denmark) were used as separation material between coated steel plates. The purpose of the LSM spacers is to serve as a contact surface with a material similar to a real SOFC cathode. The investigated contact

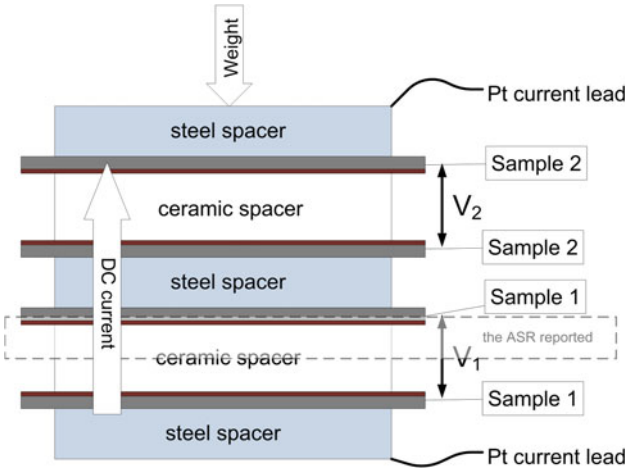

Fig. 1 The ASR measurement arrangement for coated Crofer 22 APU plates with LSM spacers. The protective coatings were applied on the Crofer 22 APU steel surfaces facing the ceramic spacers

resistance interface was therefore coated against LSM. For the experiments, several samples were stacked up and held together by a vertical load of 20 N. A sketch of the test arrangement is shown in Fig. 1. All samples were connected in a single DC current loop, the current was 0.8 A and the current density was 0.2 A/cm^2. Pt leads of 1 mm were mechanically attached to 1 mm thick steel plates at the bottom and top of the test sample stack. The voltage across each tested material couple was measured by thin (0.3-0.5 mm) Pt threads. To separate each tested substrate-coating system, 1 mm thick steel plates were used as separator disks. The binder was burned out from the green LSM spacers during a slow heat-up at 15 °C/min with a constant flow of air at 0.3 slpm, then the spacers were sintered at the beginning of the experiment for 12 h at 850 °C in contact with the coated steel to form the interface. The steady-state measurements were conducted in compressed filtered dry air at 700 °C during 1000 h. The data were logged using Agilent data logger and multiplexer. The post-mortem analysis was done using JEOL JSM-6335F field emission SEM equipped with a backscattered electron (BSE) detector and an Oxford Link Pentafet EDS analysator.

2.5 Mechanical Behavior of the Coating in Corrugated Geometry

The coated corrugated samples were tested to examine the effect of mechanical loading and substrate deformation on the HVOF coatings. The corrugated plates were supplied by ECN/ETE (Petten, The Netherlands) and were made by stamping 34 × 4.3 mm corrugations of approximately 1 mm depth into a 0.2 mm plate of Crofer 22 APU (corrugated area: 34 × 34 mm). The HVOF coatings were applied on the corrugated plate and the flat steel plate surfaces and the coatings were placed facing each other.

The mechanical loading was applied by a vertical load of 50 N, causing compressive and tensile stresses at different

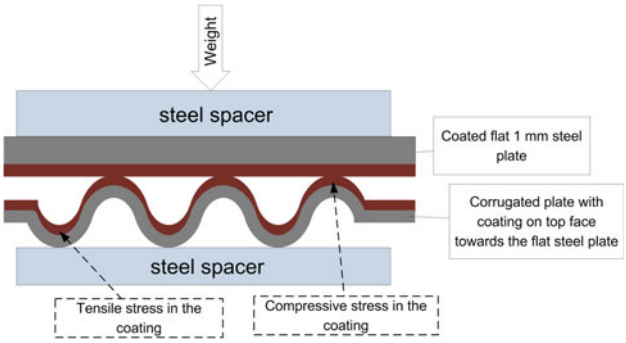

Fig. 2 The arrangement used to investigate the mechanical behavior of the coating on corrugated plates

locations of the coatings as illustrated in Fig. 2. Stationary ambient air was used in the large volume chamber furnace (lid breathable) which secured the sufficient amount of oxygen.

2.6 Stack Testing and Post-mortem Analysis

The $MnCo_{1.8}Fe_{0.2}O_4$ coating was tested in a single-cell stack that was operated for 6000 h at 700 °C. The metallic interconnects were made of 1 mm Crofer 22 APU plates and the gas channels were etched into the plates. Protective coating ($MnCo_{1.8}Fe_{0.2}O_4$) was sprayed on the cathode interconnect with approximately 20 μm as-sprayed thickness. The coated interconnect was not heat-treated and no contact coating was used. Compressible Thermiculite 866 made by Flexitallic Ltd (Cleckheaton, UK) was used as gasket (Ref 33). An anode-supported cell with a $(La,Sr)(Co,Fe)O_3$ (LSCF) cathode was used. Dry H_2 and dry air were used as fuel and oxidant, respectively. Current density was 0.3 A/cm^2.

The goals of the post-mortem analysis were to evaluate the coating, the oxide layers present on the cathode interconnect and possible Cr presence in the cathode. After testing, the single-cell stack was mounted in epoxy and cross sections were extracted from the middle area of the cell footprint. Post-mortem analysis was carried out using SEM observation and energy-dispersive x-ray spectroscopy (EDS) on JSM-6400 Scanning Microscope from JEOL equipped with a Prism 2000 detector and Spirit 1.06.02 Analyzer software from Princeton Gamma-Tech (PGT).

3. Results and Discussion

3.1 Powder and Coating Manufacturing

The applied synthesis route using carbonates was found practical in this case because of the simplicity of grinding and therefore thorough mixing of the raw materials. Additionally, the reactivity of the carbonates during calcination was found adequate. If larger amounts of powder would be done industrially, other means of mixing and perhaps other raw materials should be considered to avoid

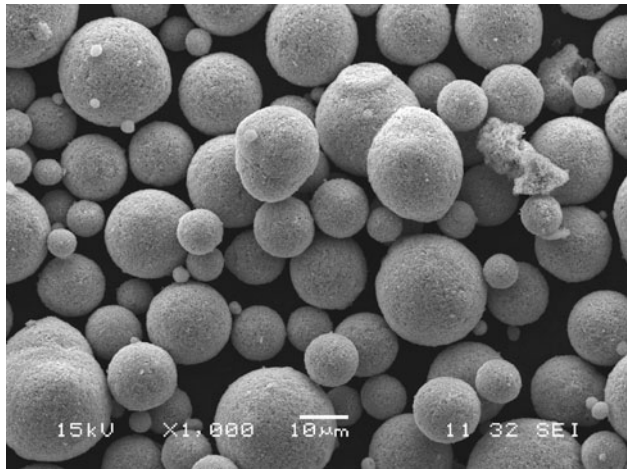

Fig. 3 Secondary electron SEM picture of spray dried $MnCo_{1.8}Fe_{0.2}O_4$ powder

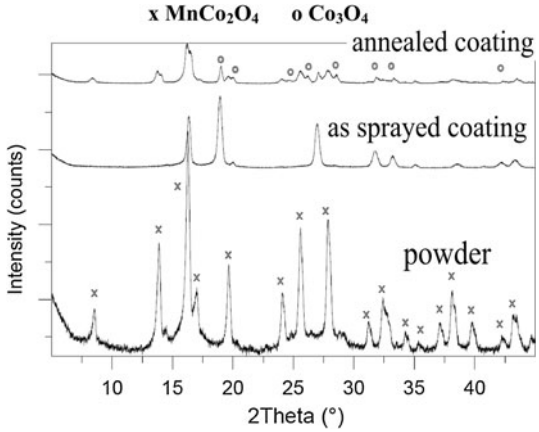

Fig. 4 XRD curves of $MnCo_{1.8}Fe_{0.2}O_4$ powder, coating in as-sprayed state and coating annealed for 2 h at 850 °C. All peaks in the as-sprayed coating correspond to simple cubic phase. The unmarked peaks in annealed coating correspond to the spinel phase $Mn_{1.5}Co_{1.5}O_4$ and $MnCo_2O_4$

the ball milling stage. For instance, chemical synthesis route using dissolved raw materials would ensure homogeneity of the end product.

The $MnCo_{1.8}Fe_{0.2}O_4$ powder prepared by spray drying had typical spherical particle shape which ensures good and constant powder feed rate during spraying. SEM pictures of the powders are presented in the Fig. 3. Only small amount of fine satellites can be seen on larger particles surface. This amount was not considered to cause any problems for HVOF spraying; dusting and feed issues were minimal. Using regular shape powder increases the deposition efficiency and decreases the amount of defects in the coating.

Illustrated in Fig. 4, the XRD pattern of $MnCo_{1.8}Fe_{0.2}O_4$ powder sintered at 1150 °C corresponds to the $MnCo_2O_4$ spinel structure. The XRD pattern of the coating in its as-sprayed state shows that the phase structure is changed during the coating process to simple cubic

structure corresponding for example to the structure of CoO and MnO (space group *Fm*-3*m*). This structure is a metastable state formed because of rapid cooling of the spray droplets during thermal spraying. The XRD curve of the coating after 2 h of annealing at 850 °C shows that the coating crystal structure transforms mainly to the spinel structures $Mn_{1.5}Co_{1.5}O_4$, Co_3O_4, and $MnCo_2O_4$. Exposure for longer time to the actual SOFC environment will fully transform the crystal structure to $MnCo_2O_4$ (Ref 32).

3.2 Exposure Tests

Figure 5 shows a typical microstructure of a $MnCo_2O_4$ as-sprayed protective coating made by HVOF; the coating shows typical lamellar structure and adequate density. Some alumina particles can be observed in the steel-coating interface from the grit blasting procedure. Oxidized steel with a HVOF $MnCo_{1.8}Fe_{0.2}O_4$ coating of 15-18 μm thickness is shown in Fig. 6 after exposure to air for 1000 h at 700 °C; the microstructure is shown in Fig. 6(a) and (b) and elemental profile from an EDS line scan is shown in Fig. 6(c). The Cr oxide layer formed between the steel and the coating during the exposure is about 0.5 μm. During high-temperature exposure, the coating sinters and loses its lamellar structure. Some closed porosity remains visible still after 1000 h of exposure with a decreasing porosity toward the surface. There is little or no Cr gradient in the coating (Fig. 6c), which means that the diffusion of Cr is effectively hindered. As a reference on oxidation, a non-coated Crofer 22 APU sample exposed to the same oxidizing conditions showed in microscopy an oxide layer of 2.5-3 μm of thickness, which is five times higher than for the coated sample. Therefore, the coating solution effectively reduces the oxidation of the steel interconnect.

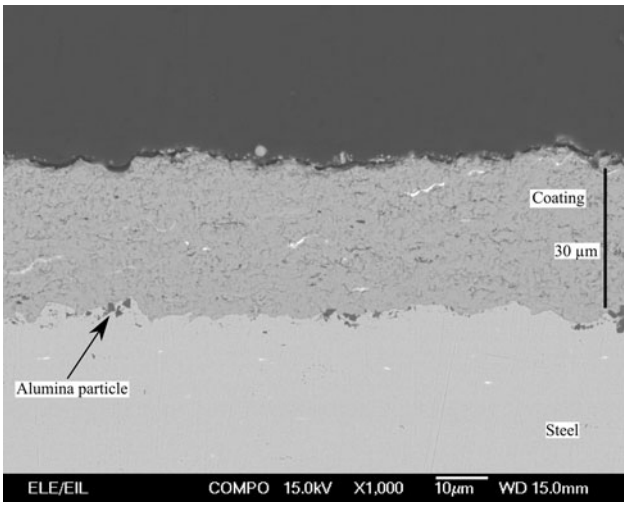

Fig. 5 A BSE SEM image of an as-sprayed HVOF $MnCo_2O_4$ coating on Crofer 22 APU substrate

3.3 ASR Measurements

The ASR measurements against time for coated and uncoated Crofer 22 APU steel are illustrated in Fig. 7. The reported ASR represents half of the ASR measured for one repeating unit in the sample stack shown in Fig. 1. The different components contributing to the ASR value consist of the steel substrate, the Cr oxide scale developing on the steel substrate surface, the protective coating, the contact resistance of the interface between the coating and the ceramic cathode material and the resistance of the ceramic cathode material (i.e., the resistance of 500 μm of LSM cathode material). The reason for the step change in the ASR taking place at 220 h is not completely understood, but is probably related to a structural instability. The change taking place at 720 h of the test in the $MnCo_{1.8}Fe_{0.2}O_4$ sample which was tested in a second test run is due to a small unintentional change in the test temperature (10 °C) due to a power shutdown. For the three samples, the test temperature was between 690 and 710 °C during the long-term test.

The ASRs of the $MnCo_{1.8}Fe_{0.2}O_4$ (15-18 μm thick) and the $MnCo_2O_4$ (20-28 μm thick) coatings are initially 20-30 mΩ cm^2 and decrease slightly to about 20 mΩ cm^2 during the first few hundred hours and then remain stable over the tested period. These results show that the coating solution is adequate to prevent degradation of the electric properties of the interconnect during SOFC operation. Comparisons of ASR values between different studies are delicate because the experimental parameters such as ASR measurement temperature, aging time, and type of spacer used are inconsistent throughout the literature. However, these ASR results are in line with results reported for similar types of coatings (Ref 6) or using a similar test arrangement (Ref 17, 34). The improvements of the ASRs during the first few hundred hours of test are attributed to the sintering of the initially lamellar coating.

The ASR of the bare Crofer 22 APU in contact with LSM is initially about 100 mΩ cm^2 and decreases throughout the tested period to reach 45 mΩ cm^2 after 1000 h of test. The observed decrease of ASR over time is mainly due to improvement in the electrical contact between steel and LSM. Both coatings show initially much lower ASRs compared to the bare Crofer 22 APU. The main source of the difference between the bare Crofer 22 APU and the coated samples is believed to originate from a lower contact resistance of the coated samples.

3.4 Mechanical Behavior of the Coating on Corrugated Geometry

The effect of the corrugated geometry on the mechanical behavior of HVOF $MnCo_2O_4$ coatings was investigated with SEM by looking at different locations of the corrugated geometry. The coating at the top of the corrugation ridges experiences a compressive force when the mechanical loading is applied. The load tends to straighten the corrugation by causing permanent plastic deformation (creep). Consequently, the coating at the bottom of the corrugation groove experiences a tensile

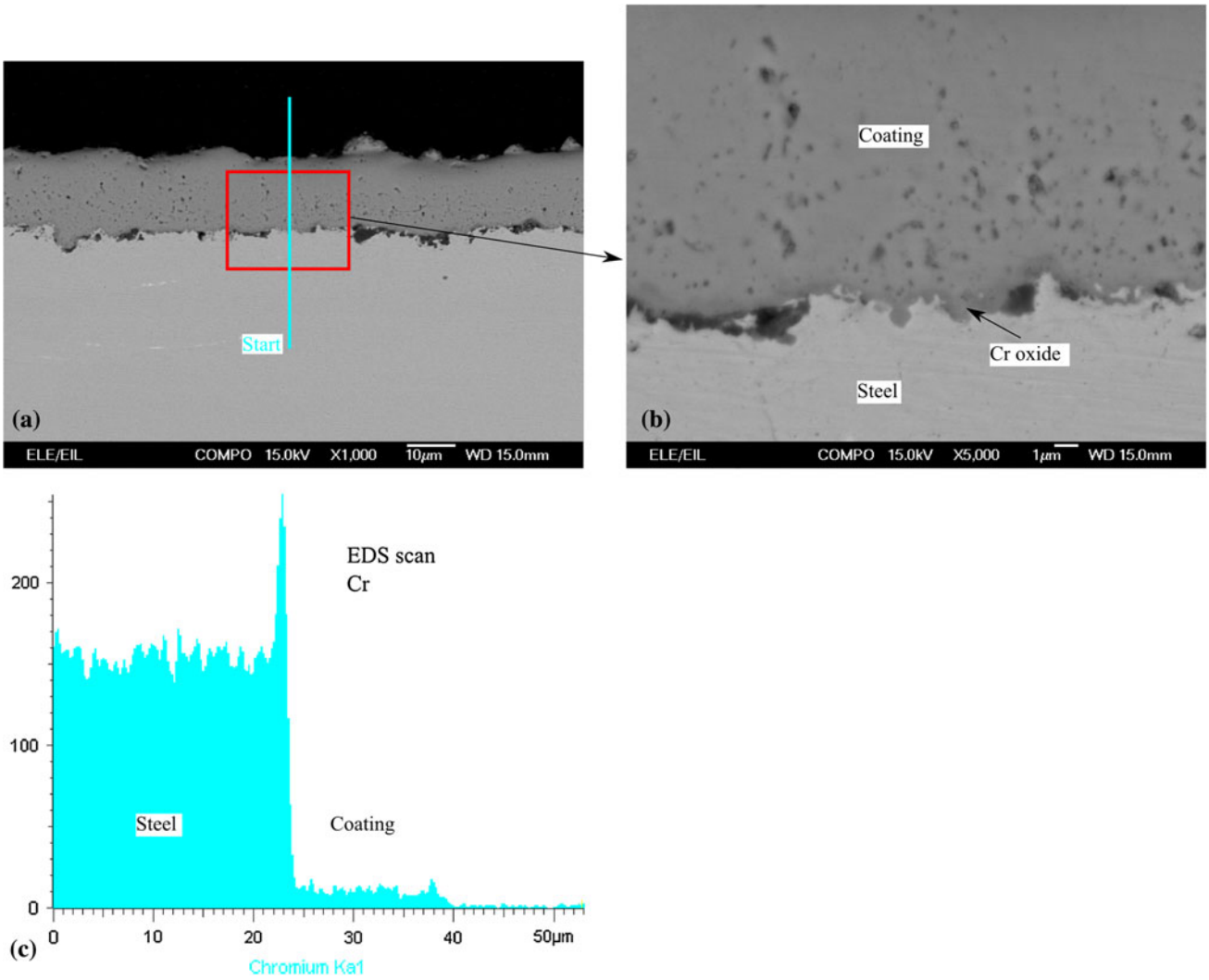

Fig. 6 (a) and (b) BSE SEM images of a HVOF $MnCo_{1.8}Fe_{0.2}O_4$ coating on Crofer 22 APU substrate exposed to air at 700 °C for 1000 h at different magnifications. (c) Measured Cr EDS profile

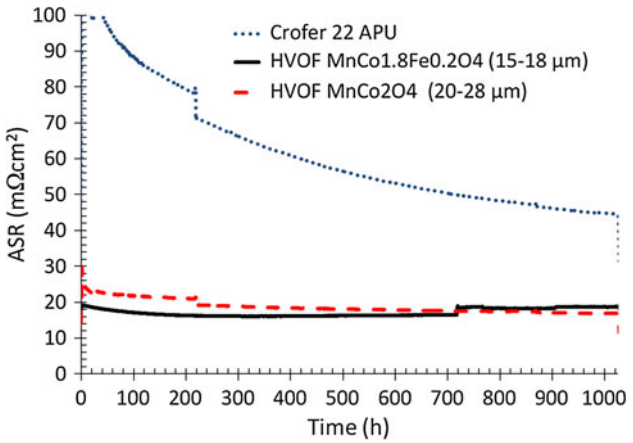

Fig. 7 Measured ASR in a 4-point DC measurement of Crofer 22 APU, coated and uncoated, all in contact with a LSM spacer. The coatings are $MnCo_{1.8}Fe_{0.2}O_4$ and $MnCo_2O_4$

stress. After a 1000 h exposure test at 700 °C, the HVOF coating at the top of the corrugation was largely intact as depicted in the SEM micrograph in Fig. 8(a). Conversely, several through-coating cracks were observed at the bottom of the groove due to tensile stress combined with the intrinsic brittleness of $MnCo_2O_4$ material and coating structure, Fig. 8(b). The stress needed for the fracture of the coating will depend closely on the distribution of flaws in the scale as well as the stress field, but it seems evident that the stresses had in this case been relaxed by through-coating cracks in the HVOF coating. Therefore, while the basic protective function of the HVOF coatings are well fulfilled, they may not be optimal for stack designs having metallic interconnects made of thin corrugated steel plates because of their propensity for cracking under tensile stress due to mechanical load. Although the steel interface at the bottom of the cracks do not show any accelerated corrosion in the present case, such effects or Cr release through the cracks could possibly take place in long-term operation. However, crack formations could possibly be

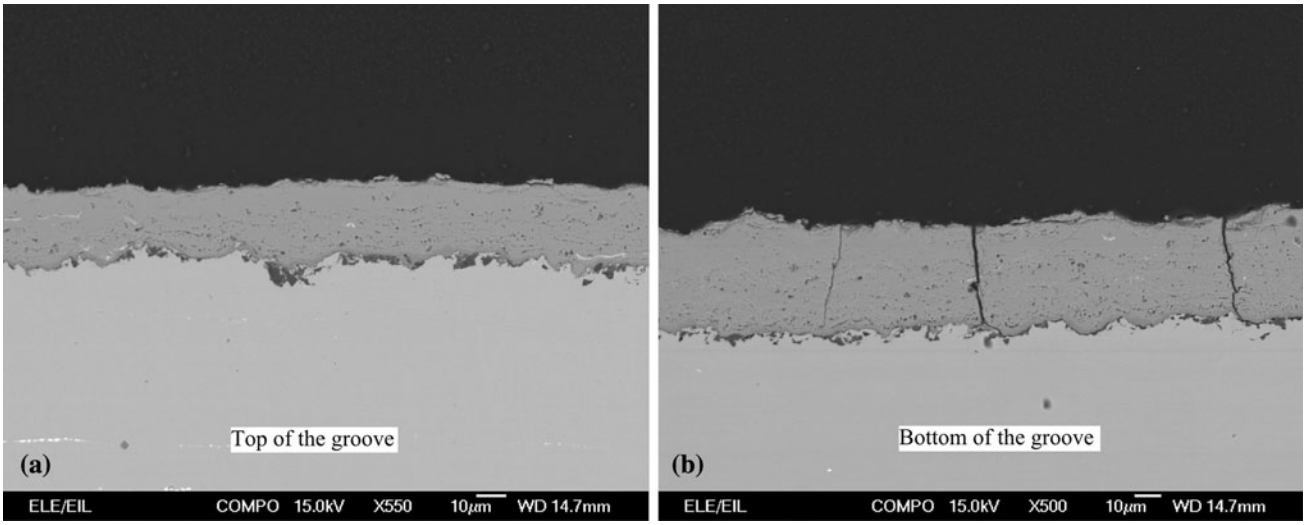

Fig. 8 SEM images from the top (a) and bottom (b) of the corrugated profile exposed to a vertical mechanical load in a high-temperature exposure test with a HVOF $MnCo_2O_4$ coating (1000 h at 700 °C in air)

avoided by adjusting the design of the corrugation and thickness of the interconnect.

3.5 Single-Cell Stack Post-mortem Analysis

Four BSE SEM images of the single-cell stack are presented in Fig. 9. Figure 9(a) shows a low-magnification view of the cathode side of the single-cell stack where the air channel and the contact location between the interconnect and the cathode are visible. It is clear that the coating covers the interconnect completely, including the geometrically challenging features such as the edges of the interconnect ribs. The gap between the cathode and electrolyte and the cracks found in the coating at the air channels are due to sample preparation.

Figure 9(b) shows the contact location between the cathode side of the cell and the coated interconnect with $MnCo_{1.8}Fe_{0.2}O_4$. The micrograph shows good contact between cathode and interconnect. The Cr-oxide scale at the surface of the interconnect metal is about 1 μm in thickness after 6000 h at 700 °C in air. This result can be compared to the exposure tests presented in section 3.2 where the Cr-oxide layer of coated steel was about 0.5 μm thick and the Cr-oxide layer of the unprotected steel was about 2.5-3 μm after 1000 h in air at 700 °C. Therefore, it can be concluded that the coating acts as an effective protection and reduces oxidation of the interconnect in a long-term test in SOFC environment. No cracks are visible in the coating itself, however closed porosity is still present. EDS analysis was performed on the area shown in Fig. 9(b) and no Cr was found neither in the coating nor in the cathode which indicates that Cr diffusion and evaporation through the coating is effectively hindered.

Figure 9(c) shows another micrograph of the coating at an air channel location. The coating presents no cracks but some closed porosity similarly to Fig. 9(b). The Cr-oxide layer under the coating is also about 1 μm thick and no Cr could be detected in the coating. Figure 9(d) illustrates the cathode located at an air channel and a EDS Cr concentration profile. As already mentioned, there is a large gap between cathode and the electrolyte (out of the picture) due to sample preparation and therefore the cathode stands alone in the epoxy. An EDS analysis of the cathode reveals that Cr was present in the cathode at this air channel location. Cr distribution is inhomogeneous and peaks at 2.1 at.%. However, most of the Cr is located away from the active cathode area which is located close to the electrolyte; therefore, the deposited Cr has probably not affected the electrochemical performance of the cathode. The Cr contamination can be either coming from the stainless steel interconnect through the protective coating or from the uncoated Crofer 22 APU air manifold and Inconel 600 air inlet pipe upstream of the cell. However, Cr deposit was located at the air channel (corresponding to Fig. 9d) and not at the contact location with the interconnect (corresponding to Fig. 9b), which supports the hypothesis that Cr has originated from the uncoated air manifold and inlet pipe. Additionally, from the EDS analysis performed across the coating, negligible Cr diffusion appears to take place across the coating. Stainless steel components and manifold upstream of the cells have been previously identified as Cr contamination sources in SOFC stacks (Ref 10, 35). From these results, the coating solution is adequate for steel interconnect protection as it reduces effectively both Cr evaporation and steel interconnect oxidation.

4. Conclusions

Protective $MnCo_2O_4$ and $MnCo_{1.8}Fe_{0.2}O_4$ coatings were manufactured on SOFC steel interconnects by HVOF coating. Exposure tests showed that a 1000 h oxidation in air at 700 °C resulted in a Cr oxide layer of 0.5 μm for the steel protected by HVOF coating. In

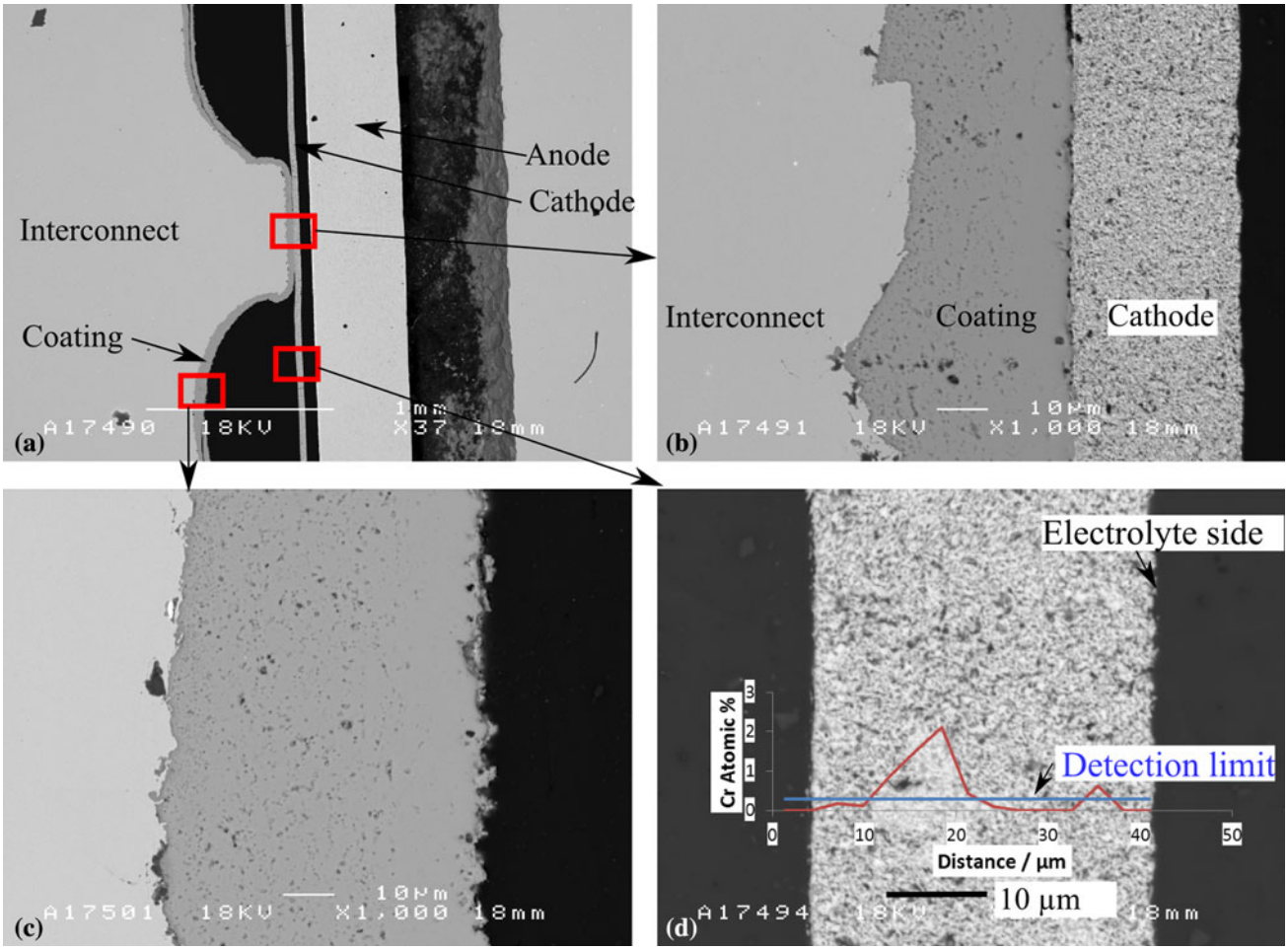

Fig. 9 BSE SEM cross section from the single-cell stack at different locations. (a) Low-magnification image of the air side of the single-cell stack. The interconnect coating composition is $MnCo_{1.8}Fe_{0.2}O_4$. (b) Contact area between coated interconnect and cathode. (c) Surface of the interconnect at an air channel location. (d) Cathode with an EDS Cr profile

comparison, uncoated steel sample developed a 2.5-3 µm Cr oxide layer in the same conditions.

ASR measurements were carried out at 700 °C for 1000 h on coated steel samples in contact with LSM spacers. The results confirmed low ASR values for coated samples of about 20-30 mΩ cm^2 with no degradation over time. These results show that the HVOF coating method developed at VTT is a suitable candidate to be used in SOFC stacks. The mechanical behavior of the coating was evaluated by applying a mechanical load on a coated corrugated thin plate. It was found that the stress arising from deformation of the plate leads to crack formation where the coating is under tension. Therefore, if such corrugated geometry is used for interconnect, more crack-resistant coating solution should be developed.

The protective coating showed adequate corrosion protection and retention of Cr in a single-cell stack test up to 6000 operation hours. The Cr oxide layer was about 1 µm thick and the coating was crack-free and Cr-free. A low concentration of Cr was detected in the fuel cell cathode; however, the uncoated steel manifold and piping upstream of the stack test setup are known to be a source of volatile Cr and are likely to be the origin of the Cr found in the cathode.

Acknowledgments

Financial support from the Finnish Funding Agency for Technology and Innovation, Tekes and the European Commission (Contract 28967, SOFC-Coat) is gratefully acknowledged. Markku Lindberg, Mika Jokipii and Seija Kivi from VTT are acknowledged for sample preparation and Vesa Vuorinen from Aalto University and Risto Parikka from VTT Expert Services Oy are acknowledged for SEM analysis.

References

1. J. Wu and X. Liu, Recent Development of SOFC Metallic Interconnect, *J. Mater. Sci. Technol.*, 2010, **26**(4), p 293-305
2. J.W. Fergus, Metallic Interconnects for Solid Oxide Fuel Cells, *Mater. Sci. Eng. A*, 2005, **397**(1–2), p 271-283

3. W.Z. Zhu and S.C. Deevi, Development of Interconnect Materials for Solid Oxide Fuel Cells, *Mater. Sci. Eng. A*, 2003, **348**(1–2), p 227-243
4. Z. Yang, K.S. Weil, D.M. Paxton, and J.W. Stevenson, Selection and Evaluation of Heat-Resistant Alloys for SOFC Interconnect Applications, *J. Electrochem. Soc.*, 2003, **150**(9), p A1188-A1201
5. M. Stanislowski, E. Wessel, K. Hilpert, T. Markus, and L. Singheiser, Chromium Vaporization from High-Temperature Alloys, *J. Electrochem. Soc.*, 2007, **154**(4), p A295-A306
6. N. Shaigan, W. Qu, D.G. Ivey, and W. Chen, A Review of Recent Progress in Coatings, Surface Modifications and Alloy Developments for Solid Oxide Fuel Cell Ferritic Stainless Steel Interconnects, *J. Power Sources*, 2010, **195**(6), p 1529-1542
7. H. Tu and U. Stimming, Advances, Aging Mechanisms and Lifetime in Solid-Oxide Fuel Cells, *J. Power Sources*, 2004, **127**(1–2), p 284-293
8. M.C. Tucker, H. Kurokawa, C.P. Jacobson, L.C. De Jonghe, and S.J. Visco, A Fundamental Study of Chromium Deposition on Solid Oxide Fuel Cell Cathode Materials, *J. Power Sources*, 2006, **160**(1), p 130-138
9. J.A. Schuler, H. Yokokawa, C.F. Calderone, Q. Jeangros, Z. Wuillemin, A. Hessler-Wyser, and J. Van Herle, Combined Cr and S Poisoning in Solid Oxide Fuel Cell Cathodes, *J. Power Sources*, 2012, **201**, p 112-120
10. O. Thomann, M. Pihlatie, J.A. Schuler, O. Himanen, and J. Kiviaho, Method for Measuring Chromium Evaporation from SOFC Balance-of-Plant Components, *Electrochem. Solid-State Lett.*, 2012, **15**(3), p B35-B37
11. J.W. Fergus, Effect of Cathode and Electrolyte Transport Properties on Chromium Poisoning in Solid Oxide Fuel Cells, *Int. J. Hydrogen Energy*, 2007, **32**(16), p 3664-3671
12. N.H. Menzler, P. Batfalsky, L. Blum, M. Bram, S.M. Groß, V.A.C. Haanappel, J. Malzbender, V. Shemet, R.W. Steinbrech, and I. Vinke, Studies of Material Interaction After Long-Term Stack Operation, *Fuel Cells*, 2007, **7**(5), p 356-363
13. K. Hilpert, D. Das, M. Miller, D.H. Peck, and R. Weiß, Chromium Vapor Species Over Solid Oxide Fuel Cell Interconnect Materials and their Potential for Degradation Processes, *J. Electrochem. Soc.*, 1996, **143**(11), p 3642-3647
14. M. Stanislowski, J. Froitzheim, L. Niewolak, W.J. Quadakkers, K. Hilpert, T. Markus, and L. Singheiser, Reduction of Chromium Vaporization from SOFC Interconnectors by Highly Effective Coatings, *J. Power Sources*, 2007, **164**(2), p 578-589
15. Y. Larring and T. Norby, Spinel and Perovskite Functional Layers Between Plansee Metallic Interconnect (Cr-5 Wt% Fe-1 Wt% Y_2O_3) and Ceramic (La0.85Sr0.15)0.91MnO_3 Cathode Materials for Solid Oxide Fuel Cells, *J. Electrochem. Soc.*, 2000, **147**(9), p 3251-3256
16. X. Chen, P.Y. Hou, C.P. Jacobson, S.J. Visco, and L.C. De Jonghe, Protective Coating on Stainless Steel Interconnect for SOFCs: Oxidation Kinetics and Electrical Properties, *Solid State Ion.*, 2005, **176**(5–6), p 425-433
17. Z. Yang, G. Xia, G.D. Maupin, and J.W. Stevenson, Conductive Protection Layers on Oxidation Resistant Alloys for SOFC Interconnect Applications, *Surf. Coat. Technol.*, 2006, **201**(7), p 4476-4483
18. Y. Fang, C. Wu, X. Duan, S. Wang, and Y. Chen, High-Temperature Oxidation Process Analysis of $MnCo_2O_4$ Coating on Fe-21Cr Alloy, *Int. J. Hydrogen Energy*, 2011, **36**(9), p 5611-5616
19. A. Balland, P. Gannon, M. Deibert, S. Chevalier, G. Caboche, and S. Fontana, Investigation of La_2O_3 and/or (Co, $Mn)_3O_4$ Deposits on Crofer22APU for the SOFC Interconnect Application, *Surf. Coat. Technol.*, 2009, **203**(20–21), p 3291-3296
20. J. Puranen, J. Lagerbom, L. Hyvärinen, T. Mäntylä, E. Levänen, M. Kylmälahti, and P. Vuoristo, Formation and Structure of Plasma Sprayed Manganese-Cobalt Spinel Coatings on Preheated Metallic Interconnector Plates, *Surf. Coat. Technol.*, 2010, **205**(4), p 1029-1033
21. K. Uusi-Esko, E. Rautama, M. Laitinen, T. Sajavaara, and M. Karppinen, Control of Oxygen Nonstoichiometry and Magnetic Property of $MnCo_2O_4$ Thin Films Grown by Atomic Layer Deposition, *Chem. Mater.*, 2010, **22**(23), p 6297-6300
22. L. Mikkelsen, M. Chen, P.V. Hendriksen, Å. Persson, N. Pryds, and K. Rodrigo, Deposition of La0.8Sr0.2Cr0.97V0.03O_3 and $MnCr_2O_4$ Thin Films on Ferritic Alloy for Solid Oxide Fuel Cell Application, *Surf. Coat. Technol.*, 2007, **202**(4–7), p 1262-1266
23. M.J. Lewis and J.H. Zhu, A Process to Synthesize (Mn, $Co)_3O_4$ Spinel Coatings for Protecting SOFC Interconnect Alloys, *Electrochem. Solid-State Lett.*, 2011, **14**(1), p B9-B12
24. V.I. Gorokhovsky, P.E. Gannon, M.C. Deibert, R.J. Smith, A. Kayani, M. Kopczyk, D. Vanvorous, Z. Yang, J.W. Stevenson, S. Visco, C. Jacobson, H. Kurokawa, and S.W. Sofie, Deposition and Evaluation of Protective PVD Coatings on Ferritic Stainless Steel SOFC Interconnects, *J. Electrochem. Soc.*, 2006, **153**(10), p A1886-A1893
25. X. Montero, N. Jordán, J. Pirón-Abellán, F. Tietz, D. Stöver, M. Cassir, and I. Villarreal, Spinel and Perovskite Protection Layers between crofer22APU and La 0.8Sr0.2FeO_3 Cathode Materials for SOFC Interconnects, *J. Electrochem. Soc.*, 2009, **156**(1), p B188-B196
26. J. Puranen, J. Lagerbom, L. Hyvärinen, M. Kylmälahti, O. Himanen, M. Pihlatie, J. Kiviaho, and P. Vuoristo, The Structure and Properties of Plasma Sprayed Iron Oxide Doped Manganese Cobalt Oxide Spinel Coatings for SOFC Metallic Interconnectors, *J. Therm. Spray Technol.*, 2011, **20**(1–2), p 154-159
27. D.P. Lim, D.S. Lim, J.S. Oh, and I.W. Lyo, Influence of Post-Treatments on the Contact Resistance of Plasma-Sprayed La 0.8Sr 0.2MnO_3 Coating on SOFC Metallic Interconnector, *Surf. Coat. Technol.*, 2005, **200**(5–6), p 1248-1251
28. H. Zhai, W. Guan, Z. Li, C. Xu, and W.G. Wang, Research on Performance of LSM Coating on Interconnect Materials for SOFCs, *J. Korean Ceram. Soc.*, 2008, **45**(12), p 777-781
29. M.J. Garcia-Vargas, M. Zahid, F. Tietz, and A. Aslanides, Use of SOFC Metallic Interconnect Coated with Spinel Protective Layers Using the APS Technology, *ECS Trans.*, 2007, **7**, p 2399
30. M. Casteel, P. Willson, T. Goren, P. O'Brien, and D. Lewis, Novel Method for Measuring Chromia Evaporation from SOFC Interconnect Materials, *ECS Trans.*, 2009, **2**(5), p 1411
31. R.N. Basu, F. Tietz, O. Teller, E. Wessel, H.P. Buchkremer, and D. Stöver, LaNi0.6Fe0.4O_3 as a Cathode Contact Material for Solid Oxide Fuel Cells, *J. Solid State Electrochem.*, 2003, **7**(7), p 416-420
32. J. Lagerbom, T. Varis, J. Puranen, M. Pihlatie, O. Himanen, V. Saarinen, J. Kiviaho, and E. Turunen, $MnCo_2O_4$ Spinel Chromium Barrier Coatings for SOFC Interconnect by HVOF, *9th Liège Conference on Materials for Advanced Power Engineering,* 2010, p 925–932
33. J.R. Hoyes and S. Bond, Gaskets for Sealing Solid Oxide Fuel Cells, *Seal. Technol.*, 2007, **8**, p 11-14
34. L. Mikkelsen, K. Neufeld, and P.V. Hendriksen, Interface Resistance Between FeCr Interconnects and La0.85Sr0.15Mn1,1O_3, *ECS Trans.*, 2009, **25**, p 1429
35. J.A. Schuler, Z. Wuillemin, A. Hessler-Wyser, C. Comminges, N.Y. Steiner, and J. Van Herle, Cr-Poisoning in (La, Sr)(Co, Fe)O_3 Cathodes After 10,000 h SOFC Stack Testing, *J. Power Sources*, 2012, **211**, p 177-183

PUBLICATION II

Method for measuring chromium evaporation from SOFC balance-of-plant components

Electrochemical and Solid-State Letters 2012,
Vol. 15, No. 3, pp. B35–B37.

Electrochemical and Solid-State Letters, **15** (3) B35-B37 (2012)
1099-0062/2012/15(3)/B35/3/$28.00 © The Electrochemical Society

Method for Measuring Chromium Evaporation from SOFC Balance-of-Plant Components

O. Thomann,[a,z] M. Pihlatie,[a] J. A. Schuler,[b] O. Himanen,[a] and J. Kiviaho[a]

[a] *VTT Technical Research Centre of Finland, FI-02044 VTT, Espoo, Finland*
[b] *EPFL Ecole Polytechnique Fédérale de Lausanne, LENI-CIME, CH-1015 EPFL, Lausanne, Switzerland*

Cr poisoning is a well-identified performance degradation process in solid oxide fuel cells (SOFC). While stainless steel (SS) interconnects have been identified to be a significant source of Cr, the Cr contribution from balance-of-plant (BoP) components located upstream of the cathode still needs to be ascertained. A method to measure Cr concentration level from BoP components was developed in this work. The volatile Cr species were collected by air sampling through a quartz tube coated with sodium carbonate. SEM observations enabled to correlate changes in the oxide layer microstructure of BoP alloys to their Cr evaporation rate.

Manuscript submitted October 21, 2011; revised manuscript received November 29, 2011. Published January 9, 2012. This was Paper 719 presented at the Montreal, QC, Canada, Meeting of the Society, May 1–6, 2011.

Cr poisoning is a significant degradation process in solid oxide fuel cells (SOFC), limiting the lifetime of SOFC systems.[1–5] Sources of volatile Cr species are stainless steel (SS) components found in the balance-of-plant (BoP) and as metallic interconnectors (MIC). The volatile Cr species are carried in the air stream and deposit on electrochemically active cathode regions hence leading to performance degradation.

In the presence of humidity, the dominant species is Cr oxyhydroxide[6] which is formed according to Equation 1.

$$Cr_2O_3(s) + 2H_2O(g) + 3/2O_2(g) \rightarrow 2CrO_2(OH)_2(g) \quad [1]$$

MIC have been identified to be an important Cr source in current SOFC designs and solutions have been developed to mitigate Cr evaporation by using protective coatings.[7–9] Recently, BoP components have drawn attention as an additional Cr source.[10,11]

On the one hand, ferritic SS are used as MIC materials because of their low thermal expansion coefficient (TEC) mismatch with the common yttria-stabilized zirconia (YSZ) electrolyte material.[12] On the other hand, austenitic SS are preferred for high temperature components in the BoP of SOFC systems due to their better mechanical and corrosion properties. As BoP components, such as heat exchangers, exhibit more complex geometries involving complex manufacturing processes, Cr-evaporation barrier coatings developed for MIC are unsuitable for the BoP. Assessment of Cr evaporation rates from BoP components is therefore seen as a prerequisite for the development of solutions to reduce this effect, such as materials selection, surface treatment, coatings or Cr trapping,[13] as well as the evaluation of improvements brought by such solutions; an area where this work aims to contribute by a dedicated measurement technique.

Cr evaporation quantification is generally evaluated on small metal coupons,[7,9,14] wherefrom it is difficult to extrapolate the actual amount for a real, complex-shaped component (uneven temperature profile and large surface area), as the evaporation rate depends on several factors such as the flow rate, flow regime and (local) temperature. The present work focuses on the methodology development for direct quantification of volatile Cr in the hot gas stream of a BoP component, i.e. a SS pipe here. The presented method is based on the denuder-technique previously taken by Froitzheim et al.[9]

Silicon evaporation is not addressed here because its evaporation rate is five orders of magnitude lower than the Cr evaporation rate.[11]

Experimental

The experimental setup is schematically illustrated in Fig. 1. A 1.2 m long SS pipe (253MA, Sandvik, inner diameter 15.8 mm, composition available in ref. 15) was exposed to a high temperature in a furnace. Humidified air (1.8 vol-% H_2O) was fed into the pipe at a flow rate of 10 l_N/min. A quartz tube (diameter 5.2 mm and length 500 mm) was inserted into the steel pipe near its end. A fraction of the flow (15–35% of the main flow) was sampled through this quartz tube by a diaphragm pump and a rotameter. The inner wall of the quartz tube was dip-coated with sodium carbonate from a surfactant-containing solution. Equation 2 describes the reaction between sodium carbonate and volatile Cr species. According to HSC,[16] the equilibrium constant of equation 2 is above 10^{10} from ambient to 800°C.

$$CrO_2(OH)_2(g) + Na_2CO_3(s) \rightarrow Na_2CrO_4(s) + H_2O(g) + CO_2(g) \quad [2]$$

Each measurement lasted 24 hours, after which the coated quartz tube was replaced without cooling down the furnace, enabling repeated measurements. The coating was dissolved after sampling with 10% nitric acid, diluted to obtain a suitable Cr concentration, and analyzed by inductively coupled plasma mass spectrometry (ICP-MS, Thermo Scientific ELEMENT 2).

The effect of the SS pipe temperature on the Cr evaporation rate was investigated by triplicated Cr evaporation measurements, carried out at 650, 700 and 750°C.

The effect of the SS pipe's heat-treatment history on its Cr evaporation rate was also investigated. For this purpose, Cr evaporation measurements were carried out on a pipe at 750°C before and after an exposure to an elevated temperature of 800°C for 100 hours. Scanning electron microscopy and energy-dispersive X-ray spectroscopy (SEM and EDX, same as in Ref. 11) were used to investigate the correlation between microstructure and Cr evaporation rate.

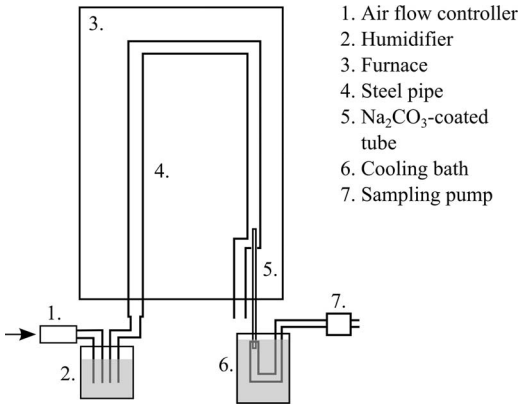

Figure 1. Schematic drawing of the experimental setup.

[z] E-mail: olivier.thomann@vtt.fi

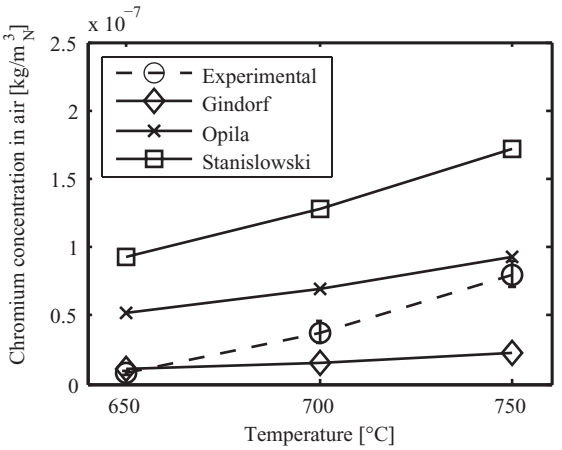

Figure 2. Measured amounts and standard deviations of evaporated Cr at different temperatures. The experimental data are compared with predictions based on thermodynamics data from different sources (data extracted from[7]).

Results and Discussion

In order to verify that most of the volatile Cr species react in the tube, coating dissolution was carried out in three steps, each corresponding to a third of the tube length. Only 7.3% of the total amount of Cr collected was found in the last third of the tube (the furthest from the Cr source), which indicates that the coated tube is sufficiently long for Cr collection. Another study found that a collection efficiency of 95% could be achieved in a similar setup.[9]

Systematic error was calculated to be 6% of the measurement (based on measurement accuracy and collection efficiency uncertainty). Random error is 13% (two times the standard deviation). The overall uncertainty is thus 14% (confidence level of 95%).

Effect of temperature on Cr evaporation.— Fig. 2 illustrates the results from Cr evaporation measurements at 650, 700 and 750°C, three measurements at each temperature, with predictions based on thermodynamics. These predictions are based on three different thermodynamics datasets extracted from.[7] The experimental values of Cr evaporation obtained with the method presented here are coherent with the literature and its good repeatability is demonstrated by the low standard deviations.

Effect of heat-treatment history on Cr evaporation:.— It was found that the temperature history has a significant effect on the amount of evaporated Cr at 750°C. Before the heat-treatment, the average volatile Cr concentration was 8.0×10^{-08} kg/m^3. After the heat-treatment (800°C, 100 hours), this value decreased to 2.0×10^{-08} kg/m^3 which corresponds to a reduction by a factor of 4. In order to explain the reason behind the decrease in Cr evaporation, SEM cross section and EDX elemental mapping were performed on the oxide layer before and after the heat-treatment. For this purpose, two SS pipes were both first exposed at a temperature of 750°C for Cr evaporation measurements. Additionally one pipe was exposed at 800°C for 100 hours before repeating Cr evaporation measurement at 750°C.

Fig. 3a and 3b show backscattered-electron (BSE) imaging of cross sections of the inner surface of the SS pipe before and after exposure at 800°C. Before exposure, a thin oxide layer (1 μm), mainly composed of Cr oxide is revealed by EDX (Fig. 3c). During exposure at 800°C, the scale has grown to 10 μm thickness; its outer oxide layer has become Cr depleted (Fig. 3d) and Fe oxide enriched (Fe EDX mapping not shown).

The reduction of Cr evaporation is explained by the growth of a thicker corrosion layer, which is Cr depleted at its surface. This Fe rich oxide layer formed during exposure at 800°C predicts a high

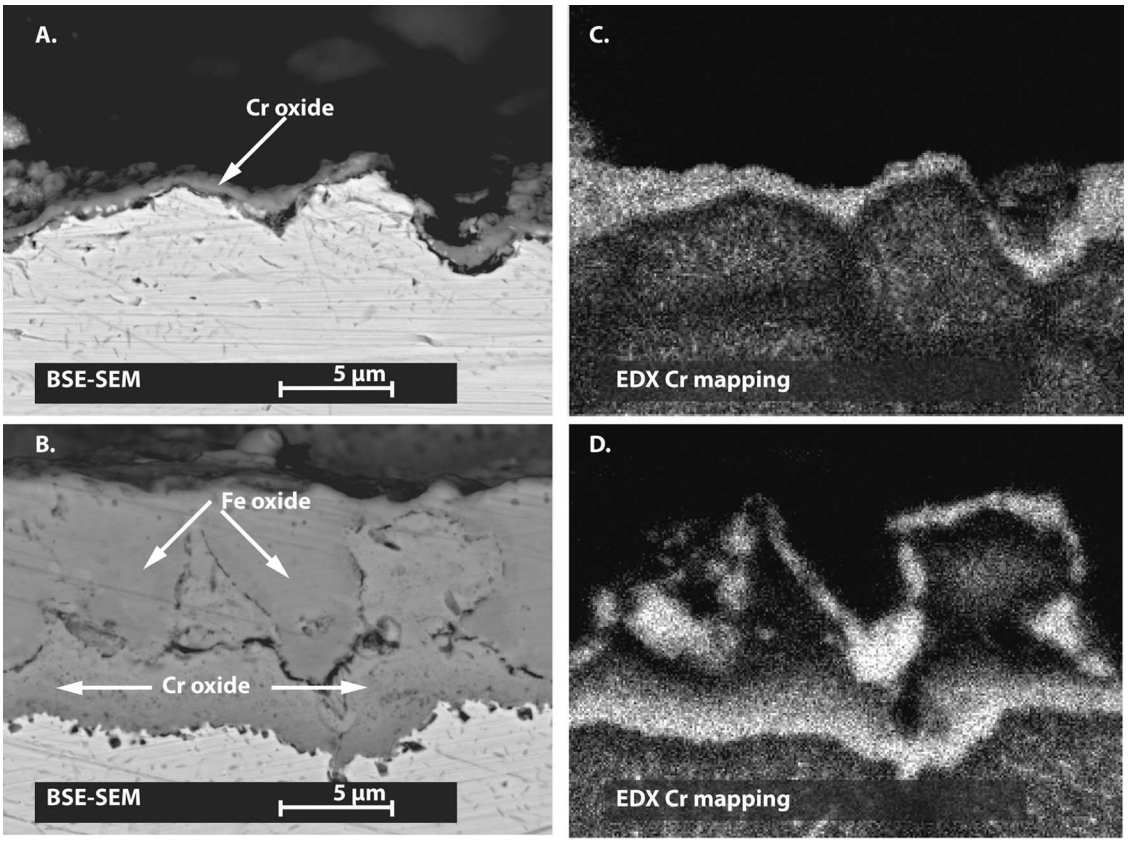

Figure 3. A. and B. SEM-BSE cross section of the SS before and after the 800°C heat-treatment. C. and D. EDX Cr mapping of the corresponding views.

corrosion rate and is thus not beneficial for SOFC applications despite a reduction of Cr evaporation by a factor 4.

Although the reason for the formation of such an oxide layer is not yet ascertained, this result is presented here to illustrate the ability of the Cr quantification method to notice an unexpected oxide layer growth through change in Cr evaporation rate. Alloy 253MA being designed to withstand higher temperature, this corrosion behavior is unexpected.

Conclusions

To gain insight on corrosion behavior of SOFC system components, a method to quantify Cr evaporation from BoP components was developed and evaluated on a heat-exchanger-imitating steel pipe.

The principle is to collect volatile Cr species by sampling hot air directly from a pipe (or any other BoP component) through a quartz tube coated with sodium carbonate. The coating is then dissolved and its Cr content analyzed by ICP-MS.

The experimental assembly is robustly designed in a way that enables its implementation at various places within a SOFC system. This makes possible the assessment of local Cr concentrations, such as at the stack air inlet or exhaust location, or after BoP components suspected to be a significant Cr source. Hence, the method enables identification of the major Cr sources of the system.

The method presented was sensitive enough to detect a heat-treatment induced decrease in evaporation rate caused by an oxide scale growth. The precision and repeatability of this measurement technique being proven, it will be used to quantify Cr evaporation from a stainless steel heat exchanger in system-relevant conditions.

Acknowledgments

This work has been supported by SofcPower 2007-2011 project funded by Tekes and Finnish industries. The authors thank Maija Lipponen of VTT for the ICP-MS analyzes.

References

1. K. Hilpert, D. Das, M. Miller, D. H. Peck, and R. Weiβ, *J. Electrochem. Soc.*, **143**, 3642 (1996).
2. H. Tu and U. Stimming, *J. Power Sources*, **127**, 284 (2004).
3. J. W. Fergus, *Int. J. Hydrogen Energy*, **32**, 3664 (2007).
4. M. C. Tucker, H. Kurokawa, C. P. Jacobson, L. C. De Jonghe, and S. J. Visco, *J. Power Sources*, **160**, 130 (2006).
5. N. H. Menzler, P. Batfalsky, L. Blum, M. Bram, S. M. Groß, V. A. C. Haanappel, J. Malzbender, V. Shemet, R. W. Steinbrech, and I. Vinke, *Fuel Cells*, **7**, 356 (2007).
6. C. Gindorf, L. Singheiser, and K. Hilpert, *J. Phys. Chem. Solids*, **66**, 384 (2005).
7. M. Stanislowski, E. Wessel, K. Hilpert, T. Markus, and L. Singheiser, *J. Electrochem. Soc.*, **154**, A295 (2007).
8. M. Stanislowski, E. Wessel, T. Markus, L. Singheiser, and W. J. Quadakkers, *Solid State Ionics*, **179**, 2406 (2008).
9. J. Froitzheim, H. Ravash, E. Larsson, L. G. Johansson, and J. E. Svensson, *J. Electrochem. Soc.*, **157**, B1295 (2008).
10. Z. Wuillemin, N. Nakajoa, A. Müllera, A. Schuler, S. Diethelm, J. Van Herle, and D. Favrat, *ECS Trans.*, **25**, 457 (2009).
11. J. A. Schuler, C. Gehrig, Z. Wuillemin, A. J. Schuler, J. Wochele, C. Ludwig, A. Hessler-Wyser, and J. Van Herle, *J. Power Sources*, **196**, 7225 (2011).
12. J. W. Fergus, *Mater. Sci. and Eng. A.*, **397**, 271 (2005).
13. J. A. Schuler, A. J. Schuler, D. Penner, A. Hessler-Wyser, C. Ludwig, and J. Van Herle, *Electrochem. Solid-State Lett.*, **14**, B132 (2011).
14. M. Casteel, P. Willson, T. Goren, P. O'Brien, and D. Lewis, *ECS Trans.*, **25**, 1411 (2009).
15. Sandvik, 253MA, http://www.smt.sandvik.com/en/materials-center/material-datasheets/tube-and-pipe-seamless/sandvik-253-ma/, (2011, accessed 16.11.2011).
16. Outotec. HSC Chemistry (2007).

PUBLICATION III

Effect of anode off-gas recycling on reforming of natural gas for solid oxide fuel cell systems

Fuel Cells 2012, Vol. 12, No. 5, pp. 754–760.

DOI: 10.1002/fuce.201200047

Fuel Cells

ORIGINAL RESEARCH PAPER

Effect of Anode off-gas Recycling on Reforming of Natural Gas for Solid Oxide Fuel Cell Systems

M. Halinen[1]*, O. Thomann[1], J. Kiviaho[1]

[1] VTT Technical Research Centre of Finland, P.O. Box 1000, FI-02044 VTT, Espoo, Finland

Received March 26, 2012; accepted June 08, 2012

Abstract

The effect of anode off-gas recycling (AOGR) on the characteristic performance of a natural gas reformer equipped with a precious metal catalyst is investigated experimentally. The reformer is operated both with synthetic AOGR gas and in steam reforming (SR) conditions. The characteristic performance in SR and AOGR mode are compared with equilibrium, and it is found that equilibrium is more readily achieved in AOGR mode. The reformer is used for extended periods of time (100–1,000 h) in conditions where carbon formation is thermodynamically possible to measure any changes in characteristic performance. No significant change in the performance is observed due to carbon formation or catalyst deactivation. The reformer could be successfully implemented in a 10 kW SOFC system with an anode off-gas recycling loop.

Keywords: Anode Off-gas Recycling, Natural Gas, Precious Metal Catalyst, Reforming, Solid Oxide Fuel Cell, Supported Catalyst

1 Introduction

Solid oxide fuel cells (SOFCs) are considered as a very promising technology in the future of energy production due to their high electrical efficiency. Additionally, SOFCs offer fuel flexibility and the fuel processing is simpler compared to fuel cells operating at lower temperature [1–3]. Fuel processing is simplified by the possibility to use hydrogen, carbon monoxide, and methane as a fuel and by the availability of recoverable heat for steam reforming (SR).

It is well known that SR of hydrocarbon fuel, typically natural gas, can be done internally in the SOFC stack [3]. This approach is advantageous due to the highly endothermal reforming reactions with hydrocarbon fuel which reduce the need for stack cooling with excess cathode air, decreases the parasitic loss caused by air blowers and can thus increase the electrical efficiency of the system. However, the temperature gradient caused by internal reforming can lead to excessive thermal stress which is detrimental for the lifetime of the stack components [4]. Moreover, there is a risk of carbon formation at the anode which can lead to a loss of performance and ultimately destruction of the stack [5, 6]. Lastly, internal reforming can decrease locally stack temperature and thus voltage resulting in sub-optimal operation. Therefore, pre-reforming of the hydrocarbon fuels is typically required in SOFC systems to mitigate these effects. The fuel is partially converted to syngas composed of methane, hydrogen, steam, carbon monoxide, and carbon dioxide in a reformer upstream of the stack. The optimum ratio between pre-reforming and internal reforming is dependent on the SOFC stack and system design, and selected operating parameters.

Recycling the hot anode off-gas to the reformer inlet is desirable in SOFC systems to provide steam for fuel reforming, since this can simplify the system design by eliminating the need of external water supply and steam generator during operation [7]. Additionally, recycling unused fuel back to the SOFC inlet can increase the electrical efficiency, since the system inlet fuel flow rate can be decreased and the system fuel utilization increased [8, 9]. Concurrently, the stack fuel utilization remains low, which has been shown to be beneficial for the lifetime of the stack [10].

Sufficient recycling ratio of anode off-gas is required to keep the SOFC, reformer, and other fuel system components free of carbon formation. It is a common engineering practice in SOFC system design to predict the gas composition, temperature, and possibility of carbon formation in a fuel reformer using thermodynamic equilibrium calculation. However, the activity of the reforming catalyst dictates both the charac-

[*] *Corresponding author, matias.halinen@vtt.fi*

teristic performance of the catalyst, and if carbon formation actually occurs to the extent that would threaten the system operation. Therefore, experimental investigation of the catalyst, reformer, and the whole fuel processing system at SOFC system relevant conditions is needed to assess the characteristic performance, measure possible deviations from the equilibrium, and to map the safe operating region without carbon formation.

Anode off-gas recycling (AOGR) has proven to be challenging to implement in actual systems due to various technical challenges, e.g., providing the motive force for recycling gas at high temperature, and identifying the suitable reforming catalyst with reliable and durable performance. Recycling blowers and ejectors suitable for SOFC system use cannot be found off-the-shelf and are still in the development phase [8]. SR of natural gas is traditionally performed with nickel-based catalyst and the effect of AOGR on such a catalyst has been previously reported in the literature. Peters et al. reported that AOGR caused a decrease of activity of a nickel-based catalyst which resulted in a decreased conversion of hydrocarbons [11]. On the other hand, Nummela and Noponen reported that AOGR had no negative effect on the performance of another pre-reformer nickel catalyst [12].

Little experimental data can be found in the literature on the effects of AOGR on a precious metal catalyst using natural gas as a fuel. Precious metal catalysts have been less investigated due to their higher price, despite having potential for higher resistance against sulfur poisoning, carbon formation, and ageing [13]. Powell et al. reported using a precious metal catalyst with natural gas in an SOFC system containing a recycling loop, but the study did not include the evaluation of the reformer performance with different operating conditions [14]. Precious metal catalyst was also used by Dietrich et al. who implemented successfully an anode off-gas recycling loop in an SOFC test setup using propane [8]. The reformer was used at high temperature (>800 °C) and at such high temperatures almost all hydrocarbons are reformed to syngas, and little is left for internal reforming reactions in the SOFC stack. In order to maintain the benefits of internal reforming in an SOFC system, it is relevant to strive for lower operating temperature for the reformer, where the conversion of methane is not complete, i.e., at temperatures between 500 and 700 °C.

This study contributes to the field of fuel processing in SOFC systems by assessing the characteristic performance of a precious metal-based reformer using natural gas in AOGR mode. Performance of the reformer in AOGR conditions is compared against SR conditions at an inlet temperature of 600 °C. Additionally, the effect of varying the recycling ratio is evaluated to determine its effect on the characteristic performance, and to identify the minimum recycling ratio that can be used safely in an SOFC system, i.e., corresponding to carbon formation-free operation. Results of this work led to the successful implementation of an anode off-gas recycling loop in a 10 kW SOFC demonstration unit, where the system is operated at nominal conditions without external water supply, and the motive force for AOGR is achieved by a recycling blower [15].

2 Experimental

2.1 Experiment Setup

The experimental setup includes a natural gas reformer and a gas analysis system. The reformer unit consists of mass flow controllers for natural gas (0–10.0 ± 0.2 L_N min^{-1}), carbon monoxide (0–1.50 ± 0.03 L_N min^{-1}), carbon dioxide (0–10.0 ± 0.2 L_N min^{-1}), hydrogen (0–5.0 ± 0.1 L_N min^{-1}), water (0–10.0 ± 0.1 g min^{-1}), nitrogen (0–10.0 ± 0.2 L_N min^{-1}), and air (0–10.0 ± 0.2 L_N min^{-1}), sulfur removal reactor filled with sulfur adsorbent (Süd-Chemie), water evaporator and mixer (CEM-303, Bronkhorst), superheater, reactor chamber equipped with a commercially available precious metal monolithic catalyst (Süd-Chemie), a particle filter and an heat exchanger (Alfa-Laval) to condensate water in the exhaust gas (Figure 1). Similar reformer catalyst has been used previously at VTT in a 5 kW SOFC demonstration unit [16]. Temperature of the process gas was measured after the evaporator (TI1 in Figure 1), at the reactor inlet (TI2), from the leading surface of the catalyst (TI3), at the center of the catalyst (TI4), from the trailing surface of the catalyst (TI5), at the reactor outlet (TI6), and after the filter (TI7). Pressure was measured before the evaporator unit (PI1), before the reactor (PI2), after the reactor (PI3), and after the particle filter (PI4). Reformer exhaust gas was analyzed with an online gas analyzer (Sick S710 series) and with gas chromatographs (Agilent 6890 N, Agilent 6850, and HP 5890 Series II).

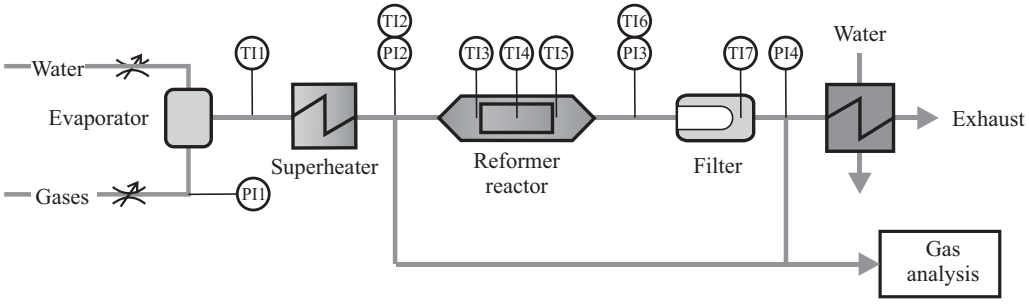

Fig. 1 Principle layout of the test equipment.

The natural gas used in Finland is of Russian origin and contains a high content of methane (ca. 98%) and low amount of higher hydrocarbon (typically 7,000 ppm of ethane, 2,000 ppm of propane, 680 ppm of butane, and trace amounts of pentane and hexane). Carbon monoxide (>99% purity), carbon dioxide (>99.7% purity), and hydrogen (>99.5% purity) were supplied from gas bottles and purified water (Millipore Elix system) was used to create the synthetic recycling gas mixture needed in the experiments.

Electric trace heating elements were used before and after the reactor to prevent cooling of the gas. The heat used in the SR reaction was provided by superheating the inlet gases with electric heaters. In order to achieve operation conditions as close to adiabatic as possible, the reactor was carefully insulated and an electric heater was enclosed around the insulation layer. The reactor and the catalyst were kept close to adiabatic conditions during the experiments, and the heating element around the reactor insulation was used only to minimize the heat losses through the inner insulation layer.

A filter thimble made of micro-quartz was installed in a metallic casing after the reactor. The filter was used to increase the probability to identify carbon formation in the reformer during the experiment. Although carbon can deposit at the surface of the catalyst, part of the carbon containing particles may be carried from the reactor downstream. The particles can be accumulated in the filter thimble gradually obstructing the gas flow. This would result as a measurable pressure increase before the filter and could be used to identify carbon formation in the reformer.

2.2 Experiment Conditions

In order to assess how the use of AOGR affects the performance of the reformer, the reformer was used both in AOGR mode and SR mode with an inlet temperature of 600 °C. The experiments with recycling gas were conducted by supplying a synthetic gas mixture. The AOGR gas mixture corresponds to the composition of a reformer inlet gas, when a varying fraction of the anode exhaust gases are recycled back to the inlet of the reformer and mixed with natural gas. The inlet gas composition and the gas hourly space velocity (GHSV) of the catalyst at different experimental conditions are given in Table 1.

The gas composition given in Table 1 was calculated prior to the experiments on the basis of equilibrated gas with an in-house developed code [9]. Since the results of this study were meant to be used to build a fuel processing unit of an SOFC demonstration unit [15], the experimental conditions given in Table 1 were constrained by a set of pre-defined boundary conditions for that specific system at nominal operating conditions. The reformer inlet temperature was defined to be ca. 600 °C due to heat exchanger present in the fuel system to pre-heat the inlet gas. Constant stack fuel utilization (FU_{SOFC} = 0.6), stack outlet temperature (T = 700 °C) and electric current for the SOFC were used in the calculations.

In an SOFC system, the reformer GHSV should be as high as possible to decrease the size of the reformer reactor, the catalyst and by that the amount of expensive catalytic material. Concurrently, the GHSV should be limited to a value where there is still sufficient catalytic activity to achieve equilibrium for the reformer outlet gas and the pressure drop at the reformer is limited. A GHSV value of ca. 20,000 h^{-1} with recycling ratio of 0.5 was selected as a reference condition for this study. GHSV was allowed to vary according to recycling ratio and other parameters to observe the effect on the reformer performance. The GHSV of the reformer catalyst increases with the recycling ratio which means that the residence time of the gas in the reformer reactor becomes shorter (Figure 2, left). Moreover, since the stack fuel utilization is kept constant in the calculations, less fuel is fed to the reformer when the recycling ratio is increased (Figure 2, right).

Additionally, the atomic oxygen-to-carbon ratio (O/C) of the gas and the conversion of methane at equilibrium are provided in Table 1. In AOGR mode, the O/C increases with the recycling ratio since more oxygen containing species of the anode off-gas are fed back to the reformer inlet. The conversion of methane at equilibrium is calculated for an adiabatic reactor with an inlet temperature of 600 °C. It should be noted that in AOGR mode equilibrium conversion of methane is generally lower compared to SR mode. However,

Table 1 Experimental conditions in SR and AOGR modes.

	Inlet gas composition (vol%)									
	H_2O/C	Recycling ratio	GHSV (h^{-1})	Natural gas	CO	CO_2	H_2	H_2O	O/C	Methane conversion (%)
	2.5	–	21,896	28.6	0.0	0.0	0.0	71.4	2.50	17
SR	2	–	18,781	33.3	0.0	0.0	0.0	66.7	2.00	15
	1.5	–	15,676	40.0	0.0	0.0	0.0	60.0	1.50	13
		0.2	10,209	56.7	5.5	8.8	14.1	14.8	0.53	5
		0.28	12,118	46.0	6.4	11.6	16.5	19.5	0.77	5
		0.36	14,470	37.1	6.9	14.0	17.9	24.0	1.02	6
		0.4	15,760	33.3	6.8	15.3	18.1	26.4	1.15	7
AOGR		0.5	19,974	25.0	6.7	18.3	17.9	32.2	1.51	9
		0.55	22,707	21.5	6.4	19.8	17.4	35.0	1.70	11
		0.6	26,053	18.2	6.0	21.2	16.5	38.0	1.90	13
		0.65	30,286	15.3	5.5	22.7	15.4	41.1	2.12	16
		0.7	35,833	12.5	5.0	24.1	14.1	44.3	2.34	19

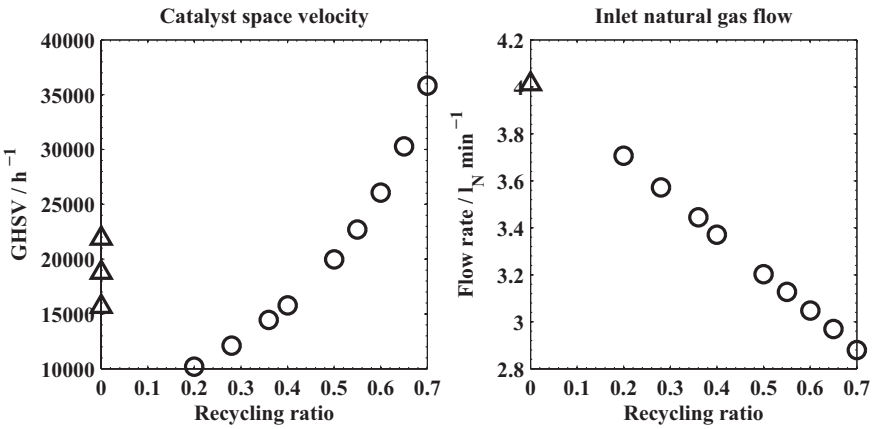

Fig. 2 The gas hourly space velocity (GHSV) of the reformer catalyst and the inlet natural gas flow rate in SR (△) and AOGR (○) modes.

above recycling ratio of ca. 0.30 the amount of methane in the reformer outlet gas becomes lower in AOGR mode than SR mode since the inlet natural gas flow rate decreases with recycling ratio (Figure 2, right). Thus, with recycling ratio above 0.30, less internal reforming would occur in the SOFC stack in AOGR than in SR mode.

The temperature limit of carbon formation in AOGR mode was calculated using HSC 6.1 [17] software to assess which experimental conditions could potentially lead to carbon formation in the reformer. According to the equilibrium calculations, the risk of carbon formation becomes more severe with lower recycling ratios (Figure 3). This is due to the lower oxygen-to-carbon ratio of the inlet gas, *i.e.*, with lower recycling ratios, less steam and other oxygen containing species are recycled back to the system inlet. With recycling ratio below 0.5, the temperature limit of carbon formation is already above the typical operating temperatures of anode supported SOFCs (above 700 °C). On the other hand, reformer can be operated at lower temperatures, e.g., 500–600 °C depending on the system design, and therefore is more prone to carbon formation since thermodynamics predict an increased risk of carbon formation for decreasing temperature.

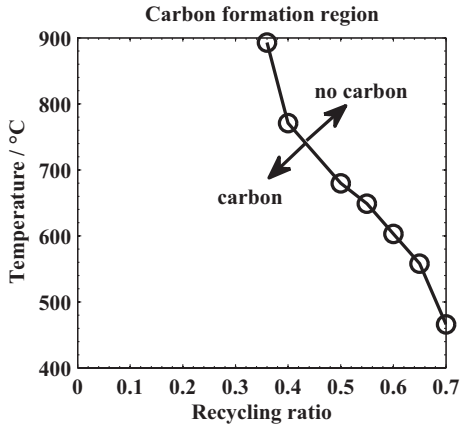

Fig. 3 Calculated temperature limit of carbon formation in AOGR mode.

To assess the characteristic performance of the reformer in AORG and SR modes the experimental results from gas analysis and the temperature measurement at the trailing edge of the catalyst were compared to the thermodynamic equilibrium at corresponding conditions. The equilibrium temperature and the composition of the reformate gas was calculated with Cantera toolbox [18] using GRI-Mech 3.0 reactions developed for natural gas combustion [19]. Equilibrium was solved for an adiabatic system, where the total enthalpy and pressure between reactants and products was kept constant, i.e., the total enthalpy of the inlet gases equals to the total enthalpy of the outlet gases and the sum of reaction enthalpies. Temperature measurement at the reactor inlet and measurements from mass flow controllers were used to define the inlet gas mixture temperature and composition for the calculations.

3 Results and Discussion

3.1 Performance of the Reformer in SR and AOGR Modes

The total duration of the experiment was over 2,500 h. During that time the reformer was used with a set of predefined operating conditions in SR and AOGR modes (Table 1). In order to achieve steady-state results, the reformer was left to stabilize for at least 24 h before each measurement. The measured inlet and outlet temperature, and the calculated reformer outlet temperature at equilibrium with different operating conditions are depicted in Figure 4. It can be seen that higher reformer outlet temperature can be achieved in AOGR mode than in SR mode. The measured and calculated equilibrium temperatures at reformer outlet correspond well in AOGR mode, where the difference between measured and calculated temperature is below 13 °C with every condition. However, in SR mode larger deviation exists between the measured and equilibrium outlet temperature, where the difference is 30–43 °C.

The measured and calculated molar fractions of methane and hydrogen in the reformer outlet gas are presented in Figure 5. The molar fractions are given on dry basis. Similarly to the reformer outlet temperature (Figure 4), there is a larger deviation between the measured and calculated values in SR than in AOGR mode. The difference between the values in SR mode cannot be explained only by the uncertainty related to the gas analysis (ca. 4% of the measured value).

Since both the outlet temperature and mole fraction of methane are higher than corresponding equilibrium values, kinetics are limiting the extent of the SR reaction. This indicates that either the space velocity should be decreased or the inlet temperature should be increased to achieve thermodynamic equilibrium. In AOGR mode and the same reactor inlet

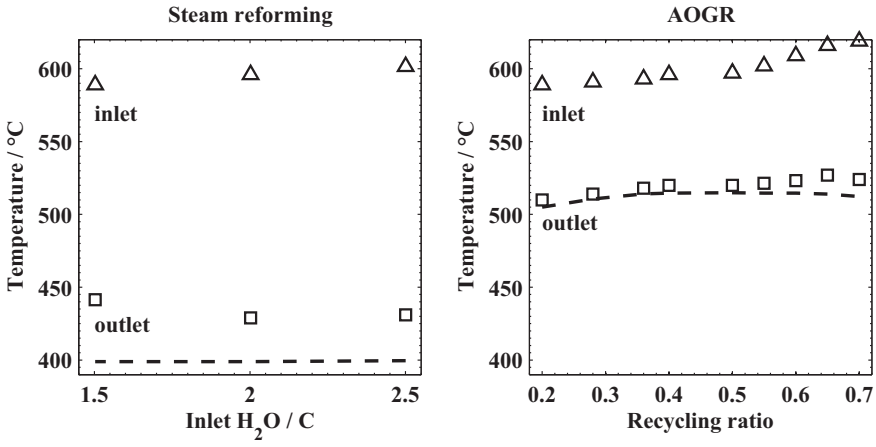

Fig. 4 Inlet and outlet temperature of the reformer in SR and AOGR modes. △: measured inlet temperature, □: measured outlet temperature, dashed line: calculated equilibrium outlet temperature.

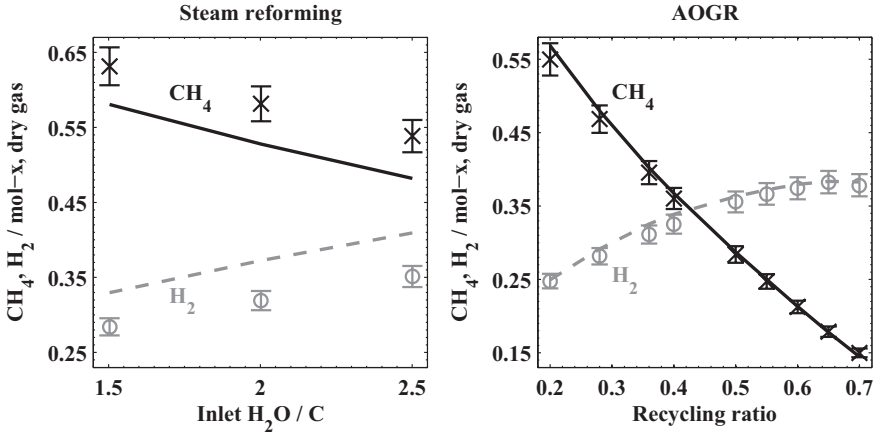

Fig. 5 Molar fraction of methane and hydrogen at reformer outlet with varying SR and AOGR conditions. Measured values are x: methane and ○: hydrogen. Calculated equilibrium values are solid line: methane and dashed line: hydrogen.

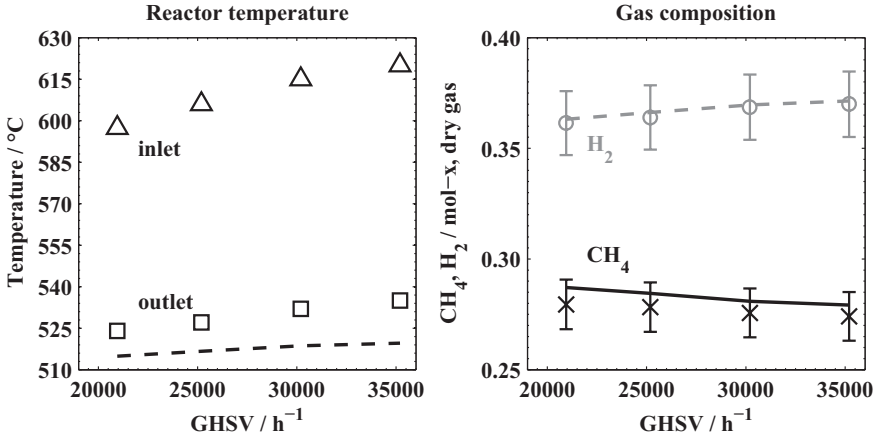

Fig. 6 Inlet and outlet temperature of the reformer operating in AOGR mode (left) and molar fraction of methane and hydrogen at the reformer outlet (right) with varying GHSV at recycling ratio of 0.5. Measured values are △: inlet temperature, □: outlet temperature, x: methane, and ○: hydrogen. Calculated equilibrium values are presented with lines.

temperature at 600 °C, the measured values match well with the calculated values. Equilibrium is reached regardless of the recycling ratio which shows good characteristic performance of the reformer in AOGR mode.

The difference in behavior of the reformer in SR and AOGR mode with respect to achieving equilibrium could be explained by the lower fuel inlet flow rate in recycling condition (e.g., 3.2 L_N min^{-1} of natural gas for a recycling ratio of 0.5) compared to SR condition (4 L_N min^{-1}, see Figure 2). In order to investigate this reason, experiments were conducted in AOGR mode (recycling ratio 0.5) with varying space velocity and thus fuel inlet flow rate. The flow rate of gases was increased to the maximum that was possible with the test equipment. The space velocity and the natural gas flow rate were increased up to 35,000 h^{-1} and 5.4 L_N min^{-1}, respectively. The results depicted in Figure 6 show that there is no increasing deviation between experimental and equilibrium values for temperatures and gas composition. Therefore, it can be concluded that some other rate limiting phenomena are preventing the achievement of equilibrium condition in the SR conditions tested. Additionally, these results show that relatively high space velocity can be achieved using this type of precious metal based catalyst in AOGR mode. As a comparison, nickel-based catalyst have been used at much lower space velocity in the range of 2,000–6,000 h^{-1} [12].

3.2 Performance of the Reformer in Carbon Formation Prone Conditions

Periodically, the reformer was used in certain AOGR conditions for a much longer time to observe any changes in performance of the reformer due to carbon formation and accumulation in the catalyst, or due to other catalyst deactivation processes. The longest hold period used in this study was 1,000 h. In addition to the recycling ratio, the reformer reactor inlet temperature and/or space velocity was varied for selected experiment conditions to see any short term changes in the performance (Table 2). The primary characteristic performance measurements that were monitored during these extended holds were the reformer outlet gas composition, gas temperature, and pressure drop over the catalyst and filter. Additionally, after each extended hold period, the entire test equipment was flushed with nitrogen and air to

Table 2 Operating conditions during extended holds.

Hold no.	Recycling ratio	Inlet temperature (°C)	GHSV (h^{-1})	Hold time (h)
1	0.60	609	26,053	122
2	0.50	597	19,979	121
3	0.50	598	19,965	117
4	0.50	513	19,981	67
5	0.50	600	19,981	1,000
6	0.20	589	10,209	165
7	0.20	646	20,260	165

oxidize possible carbon deposits, and to detect any oxidized carbon as CO and CO_2 with the online gas analysis equipment. It should be noted that carbon formation is thermodynamically possible at the measured reformer reactor outlet temperature with all the conditions given in Table 2 (see Figure 3).

The reactor outlet temperature and fraction of methane at the outlet gas during the periods of extended hold, along with the corresponding equilibrium values, are depicted in Figure 7. It should be noted that no significant changes in the outlet gas composition or gas temperature occurs during the different hold periods. Concurrently, a good correspondence with equilibrium values is maintained over the hold period. Toward the end of the experiments, at low recycling ratio of 0.2, a small increase of methane fraction is observed at higher inlet temperature. However, with this low recycling ratio, carbon can already form readily at the operating temperature of the SOFC and it is very unlikely that an actual system could be operated safely with such a low recycling ratio without additional steam supply.

Similarly to the outlet temperature and methane fraction, the pressure drop over the reformer reactor and filter remained unchanged (measured changes in pressure drop <1 mbar) during the different operating conditions. Additionally, no carbon deposits were detected at the catalyst and downstream with the oxidation procedure performed at the end of each hold period. It is possible that minor carbon deposits were accumulated to the superheater located upstream to the catalyst, but the amount of carbon was very small, only a few milligrams, and did not increase during longer hold periods. These results clearly demonstrate that carbon formation is not occurring in the experimental conditions tested to an extent that would compromise the operation of this reformer in an SOFC system.

4 Conclusion and Future Work

The performance of a natural gas reformer with a precious metal catalyst was experimentally evaluated using a set of operating conditions in SR and AOGR modes. The experiments revealed that thermodynamic equilibrium was achieved in AOGR mode. On the other hand, in SR mode, equilibrium was not achieved; both outlet temperature and methane mole fraction were higher than the values at thermodynamic equilibrium. These results indicate that the SR reactions were kinetically limited and that the space velocities used in the experiments were too high to reach equilibrium.

Therefore, it is clear that equilibrium is more readily achieved in AOGR mode than SR with this precious metal catalyst. When these results are utilized for SOFC system design and operation, it can be concluded that the size of the catalyst and the reformer can be decreased when an anode off-gas recycling loop is used for fuel processing instead of SR.

The reformer unit was used for over 2,000 h with operating conditions where carbon formation is predicted at thermodynamic equilibrium. Recycling ratios as low as 0.2 were used during the experiments, which are already beyond safe operating limits in an actual SOFC system since carbon formation at Ni-YSZ anode would be expected. However, no significant changes in performance were observed based on measurements of outlet gas composition, pressure drop, and temperature. Additionally, the periodic oxidation cycles did not reveal any significant carbon deposits in the reformer. Therefore, no significant carbon formation occurred during the experiment that would change the characteristic perfor-

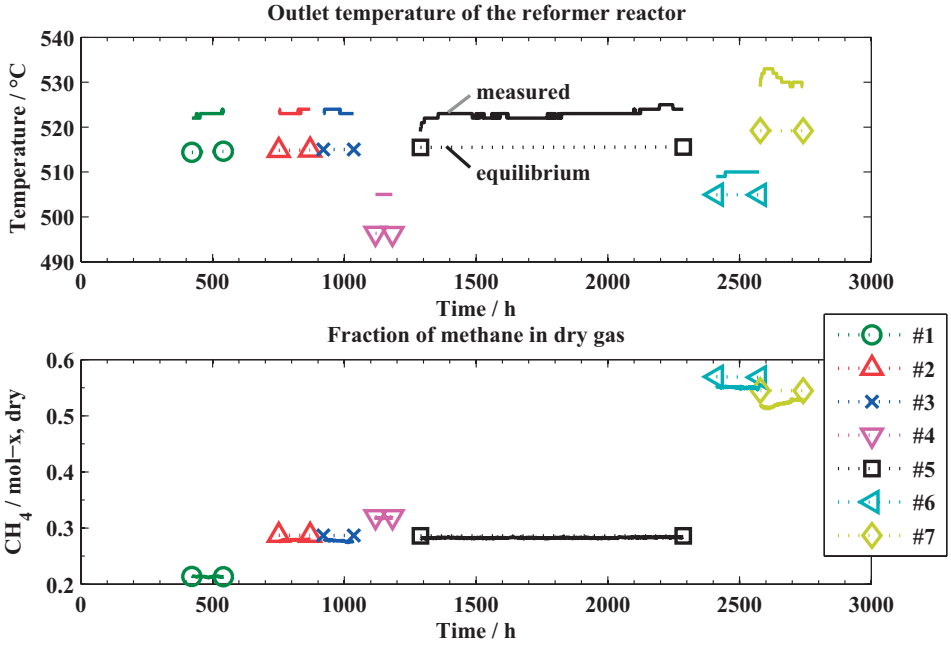

Fig. 7 Temperature (above) and mole fraction of methane (below) at reactor outlet during the experiment. The measured value is presented by a solid line and the calculated equilibrium value by a dashed line with markers at ends. Measured data in other process conditions is excluded to improve the clarity of the figure.

mance of the reformer and compromise operation in SOFC system conditions.

According to the results presented in this study, the reformer unit is suitable to be used in an SOFC fuel processing system which includes an anode off-gas recycling loop. Since good correspondence with equilibrium was always reached when AOGR mode was used, further experiments are needed to assess the operating parameters, e.g., maximum space velocity, where equilibrium is not reached anymore. Furthermore, the natural gas used in the experiments contains less than 1% of higher hydrocarbons than methane. Sufficient conversion of C_{2+} hydrocarbons has to be addressed by conducting future experiments with a fuel gas that contains higher hydrocarbon content.

Acknowledgements

The authors would like to acknowledge Kaisa Lanttola for conducting the GC analysis. Markus Rautanen, Timo Murtonen, and Kai Nurminen are thanked for assisting in the experiments. Anna Kunnas from Wärtsilä Finland Oy is thanked for collaboration and useful discussions. Funding for this study was obtained from SofcPower – project. Finnish Funding Agency for Technology and Innovation, as well as the companies participating in the project are gratefully acknowledged for their financial support.

List of Symbols

$\mathrm{RR} = \dfrac{\dot{V}^{\mathrm{recycled}}}{\dot{V}^{\mathrm{out}}_{\mathrm{SOFC}}}$ Recycling ratio

$\mathrm{GHSV} = \dfrac{\dot{V}^{in}_{\mathrm{reformer}}}{V_{\mathrm{reformer}}}$ GHSV of the reformer at NTP, h^{-1}

$$\mathrm{FU_{SOFC}} = \frac{\mathrm{I}}{F\left(2\dot{n}^{recycled}_{H_2} + 2\dot{n}^{recycled}_{CO} + 8\dot{n}^{recycled}_{CH_4} + z_{NG}\dot{n}_{NG}\right)}$$

Fuel utilization of the SOFC

$\mathrm{FU_{SYS}} = \dfrac{I}{z_{\mathrm{NG}}F\dot{n}_{\mathrm{NG}}}$ Fuel utilization of the whole SOFC system

$\mathrm{O/C} = \dfrac{\dot{n}_{CO} + 2\dot{n}_{CO_2} + \dot{n}_{H_2O}}{\dot{n}_{CH_4} + \dot{n}_{CO} + \dot{n}_{CO_2}}$ Oxygen-to-carbon ratio

F Faraday's constant, 96,485 A s mol^{-1}
I Current, A
$\dot{n}$ Molar flow, mol s^{-1}
V_{reformer} Geometrical volume of the reformer
$\dot{V}$ Volume flow in NTP, m^3 s^{-1}
z_{NG} Valence number for natural gas

References

[1] Y. Yi, A. D. Rao, J. Brouwer, G. S. Samuelsen, *J. Power Sources* **2005**, *144*, 67.
[2] S. L. Douvartzides, F. A. Coutelieris, A. K. Demin, P. E. Tsiakaras, *AIChE J.* **2003**, *49*, 248.
[3] D. Mogensen, J.-D. Grunwaldt, P. V. Hendriksen, K. Dam-Johansen, J. U. Nielsen, *J. Power Sources* **2011**, *196*, 25.
[4] R. Peters, R. Dahl, U. Klüttgen, C. Palm, D. Stolten, *J. Power Sources* **2002**, *106*, 238.
[5] N. J. J. Dekker, J. P. Ouweltjes, G. Rietveld, *ECS Trans.* **2007**, *7*, 1465.
[6] H. Timmermann, W. Sawady, D. Campbell, A. Weber, R. Reimert, E. Ivers-Tiffé, *J. Electrochem. Soc.* **2008**, *155*, B356.
[7] E. Riensche, J. Meusinger, U. Stimming, G. Unverzagt, *J. Power Sources* **1998**, *71*, 306.
[8] R.-U. Dietrich, J. Oelze, A. Lindermeir, C. Spitta, M. Steffen, T. Küster, S. Chen, C. Schlitzberger, R. Leithner, *J. Power Sources* **2011**, *196*, 7152.
[9] M. Noponen, M. Halinen, J. Saarinen, J. Kiviaho, *ECS Trans.* **2007**, *5*, 545.
[10] D. Larrain, J. Van herle, D. Favrat, *J. Power Sources* **2006**, *161*, 392.
[11] R. Peters, E. Riensche, P. Cremer, *J. Power Sources* **2000**, *86*, 432.
[12] A. Nummela, M. Noponen, *European Fuel Cell Forum*, Lucerne, Switzerland **2009**, p. B0301.
[13] D. Shekhawat, D. A. Berry, J. J. Spivey, *Fuel Cells: Technologies for Fuel Processing*, Elsevier Ltd., Oxford, UK **2011**, p. 555.
[14] M. Powell, K. Meinhardt, V. Sprenkle, L. Chick, G. McVay, *J. Power Sources* **2012**, *205*, 377.
[15] M. Halinen, M. Rautanen, J. Saarinen, J. Pennanen, A. Pohjoranta, J. Kiviaho, *ECS Trans.* **2011**, *35*, 113–120.
[16] M. Halinen, J. Saarinen, M. Noponen, I. C. Vinke, J. Kiviaho, *Fuel Cells* **2010**, *10*, 440–452.
[17] Outotec. HSC Chemistry 6.1. 2007.
[18] D. G. Goodwin, in *Chemical Vapor Deposition XVI and EUROCVD 14* (Eds. M. Allendorf, F. Maury, F. Teyssandier), PV 2003-08, The Electrochemical Society Proceeding Series, Pennington, NJ, USA **2003**, 155.
[19] G.P. Smith, GRI-MECH 3.0, can be found under http://www.me.berkeley.edu/gri_mech/, accessed **2012**.

PUBLICATION IV

Experimental study of SOFC system heat-up without safety gases

International Journal of Hydrogen Energy 2014,
Vol. 39, No. 1, pp. 552–561.

Available online at www.sciencedirect.com

ScienceDirect

journal homepage: www.elsevier.com/locate/he

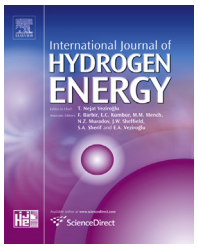

Experimental study of SOFC system heat-up without safety gases

*M. Halinen**, *O. Thomann*, *J. Kiviaho*

VTT Technical Research Centre of Finland, Espoo, Finland

ARTICLE INFO

Article history:
Received 13 August 2013
Received in revised form
2 October 2013
Accepted 7 October 2013
Available online 8 November 2013

Keywords:
Solid oxide fuel cell
System
Reformer
Heat-up
Start-up
Anode off-gas recycling

ABSTRACT

Premixed safety gas is conventionally used to keep the anode of a solid oxide fuel cell (SOFC) under reducing conditions during heat-up. This article presents the results of an experimental study to heat up a SOFC system and stack without the said premixed safety gases, i.e. by utilizing a natural gas pre-reformer and anode off-gas recycling (AOGR). Firstly, ex-situ experiments were conducted to investigate the operability of a pre-reformer during system heat-up. It was found that any oxygen fed to the reformer hinders the reforming reactions at low temperatures. Secondly, based on the ex-situ findings, series of heat-up cycles were conducted with a complete 10 kW system using AOGR and a planar SOFC stack. In these experiments it was found that the system heat-up is possible with fuel gas and steam only, without the need for premixed reducing safety gases. Use of the fuel gas instead of a premixed safety gas did not result in a significant performance loss in the SOFC stack. Therefore, such a heat-up strategy was developed for SOFC systems that reduces the need of premixed safety gas storage space and thus decreases the system cost.

1. Introduction

Solid oxide fuel cells (SOFCs) enable energy production from different hydrocarbon fuels with high efficiency. SOFCs require high operating temperatures, e.g. 700–800 °C for anode supported cell types. Thus the fuel cell stack and other system components have to be heated up to operating temperature before the electricity production can begin. Lengthy heat-up times of several hours may be required to maintain the temperature gradient and the thermal stresses in the stack at acceptable level [1].

The nickel in the SOFC anode substrate has to remain at reduced state at elevated temperatures. This is accomplished by supplying sufficient amount of fuel or other reducing gas to the stack. If the reducing gas supply is discontinued, then the nickel in the anode substrate will start to re-oxidize, which will first deteriorate the cell performance and eventually destroy the SOFC by cracking the cell [2]. First signs of the oxidation of the nickel cermet anode have been measured as low as 290 °C [3], and it has been shown that the oxidation of the anode substrate proceeds more rapidly as the temperature increases [4]. Permanent damage to the cell may occur in a matter of minutes if there is forced oxygen supply to the anode [5]. Indeed, without the forced oxygen supply and by minimizing the time under oxidizing conditions at elevated temperatures, the redox tolerance of the stack can increase significantly [6]. Ideally, the re-oxidation could be avoided, if no oxygen is transported to anode. However, the anode supported SOFC stack is not a hermetically sealed device, and some air will eventually leak from the cathode side of the stack via the electrolyte or stack seals [7]. Additionally, ambient air can leak to the anode through other fuel system

* *Corresponding author.*
E-mail address: matias.halinen@vtt.fi (M. Halinen).
0360-3199/$ – see front matter
http://dx.doi.org/10.1016/j.ijhydene.2013.10.043

Table 1 – Test gas mixtures used for determining the light-off temperature.

Run		1	2	3	4	5	6	7
Gas flow/NLPM	Natural gas	0.5	0.5	0.5	0.5	0.5	0.5	0.5
	H_2O	10	10	10	10	10	10	10
	N_2	10	10	10	10	10	10	10
	H_2	–	–	0.2	0.05	0.1	0.15	0.4
	Air	–	0.5	0.5	0.5	0.5	0.5	0.5
H_2/O_2			0	2	0.5	1	1.5	4

components (e.g. reformer or heat exchanger) or through connecting piping from the air system. Therefore, it is necessary to feed reducing gas to the stack during the heat-up cycle to displace the oxygen in the fuel system and to protect the stack from re-oxidation. Furthermore, it may be necessary to sustain the flow of reducing gas for several hours during the system heat-up and cool-down, while the stack temperature is still high enough for significant re-oxidation and cell damage.

SOFC system concepts based on the anode off-gas recirculation (AOGR) achieve higher efficiencies and potentially simpler design when compared to systems without AOGR [8]. Therefore, they are considered technically advantageous, and there are studies where the AOGR has been successfully used in SOFC systems [9–11]. However, for a planar stack with cross-over leakage (air is leaking to fuel side and vice versa), utilization of AOGR complicates the heat-up procedure since there is a forced supply of oxygen to the fuel system due to the leakages. Furthermore, prior to starting the SOFC system electricity production, all fuel system components have to be heated up above the dew point before the recirculation of the anode off-gas with high steam content can be initiated. Otherwise, water could condensate to the system components (e.g. reformer catalysts and recirculation blowers), which would have detrimental effects on their operation.

The most straightforward way to provide a reducing gas supply is to utilize gas containers of premixed safety gas e.g. hydrogen–nitrogen mixtures. Indeed, due to its simplicity, this approach has been adopted by the majority of research laboratories that conduct research on solid oxide fuel cells or stacks. For example, the 10 kW demo unit at VTT [9] would consume ca. 5 bottles (50 L, 200 bars) of premixed safety gas with 4 vol-% of hydrogen during a heat-up cycle. In commercial products however, this approach is not desirable, due to large amount of gases needed for heat-up cycles spanning several hours. The gas containers require additional space, and increase the cost of both installation and servicing of the system. Thus it would be beneficial if the reducing gas could be generated with the existing Balance-of-Plant equipment which is fundamental for system operation. The most obvious solution would be to utilize the fuel supply (e.g. natural gas), the pre-reformer and the start-up steam generator to produce hydrogen-containing natural gas reformate.

In this article, the heat-up of a SOFC system and stack without using the premixed safety gases is investigated experimentally. Firstly, ex-situ experiments are conducted in a stand-alone reformer test bench. The experiments were done to realize the restrictions of reforming at low temperature in a system with AOGR and air leakage (i.e. forced oxygen supply to the fuel system). Secondly, series of heat-up cycles were done with a complete 10 kW SOFC system using AOGR and a planar SOFC stack. The results of the ex-situ experiments were applied to devise a safe heat-up procedure that would not damage the stack and removes the need for premixed safety gas. The performance of the stack was investigated after each heat-up to evaluate possible damage to the stack due to these heat-up procedures. There are several studies where the heat-up of a SOFC has been investigated by modelling [1,12–18], but to the authors' knowledge, no experimental work with a complete planar SOFC system utilizing AOGR has been published previously.

2. Experimental

2.1. *Ex-situ reformer experiments*

The ex-situ experiments were conducted in a separate reformer test bench described in detail in Ref. [19]. The aim of the experiment was to assess the activity of the catalyst at low temperature in steam reforming (Eq. (1)) using different inlet gas mixtures. This information is highly relevant to conduct the heat-up experiment on the SOFC system. The light-off temperature was determined by the reformer inlet gas temperature at which the reformer starts to convert methane to hydrogen according to Eq. (1).

$$CH_4 + H_2O \Leftrightarrow CO + 3H_2 \quad (1)$$

The reformer included a commercial precious metal monolithic catalyst (Süd-Chemie). The gas composition at the reformer outlet was monitored continuously with an online gas analysis equipment (IR-based for CH_4, thermal conductivity for H_2 and paramagnetic for O_2, Sick Maihak S700 series). Due to different channels cross-sensitivity, the analyser results should be used to evaluate trends and not as quantitative measurements. The temperature of the inlet gas was ramped up from 200…250–550 °C with a rate of ca. 2 °C min^{-1}. The gas hourly space velocity (GHSV i.e. gas volume flow at NTP divided by catalyst volume) used was ca. 32,000 h^{-1}. The different inlet gas mixtures investigated (Table 1) are relevant to SOFC system operated on natural gas including an anode-off gas recycling (AOGR) loop during first stages of the heat-up, where the fuel and steam supply have just been initiated. At that time, the temperature of both the pre-reformer and the stack are low and little or no reforming activity is expected to occur. Without reforming reactions, the gas

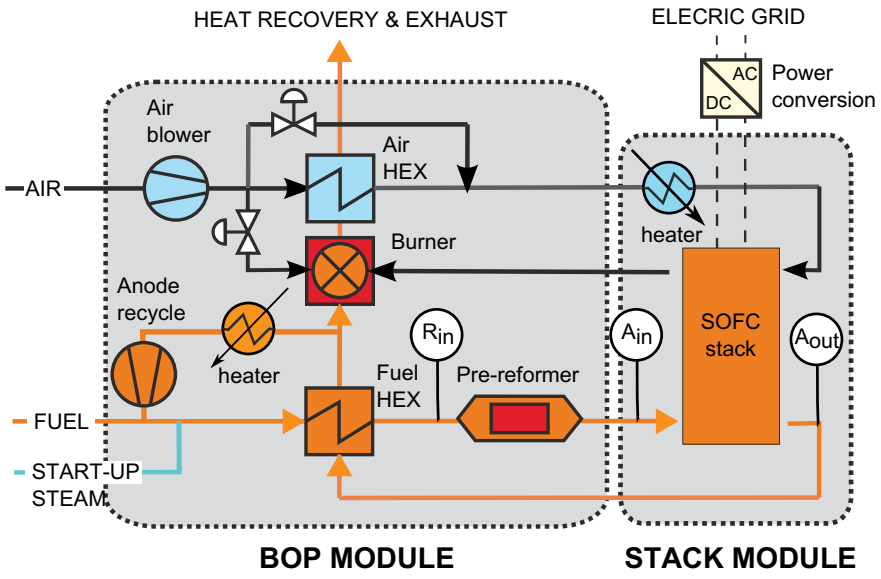

Fig. 1 – VTT 10 kW demo unit layout with fuel system gas sampling locations. Reproduced and adapted from Ref. [9]. Copyright 2011, The Electrochemical Society.

recirculating in the fuel system consists of the inlet flows i.e. fuel gas and steam as well as air originating from stack leakages. The test gas in run 1 consisted of natural gas (ca. 98% methane [19]), steam and nitrogen. A small fraction of air was introduced in the run 2–7 to simulate the effect of the presence of oxygen originating from air leakage to the fuel system and into the recycled gas. In the other test gases (run 3–7), hydrogen was added with varying H_2/O_2 ratio from 0 to 4 according to the Eq. (2).

$$O_2 + 2H_2 \Leftrightarrow 2H_2O \quad (2)$$

2.2. *System heat-up experiments*

The heat-up experiments were conducted on VTT's 10 kW SOFC demo unit [9]. The VTT demo unit consists of two interconnected modules, the balance of plant (BoP) module and the stack module, containing a planar SOFC stack (Fig. 1). The fuel system utilizes an AOGR loop, which enables operation without external steam supply when the stack current and single-pass fuel utilization are high enough. Ambient air is fed to the air system with a blower and filtered with a particle filter. Other system components include e.g. heat exchangers, catalytic burner and reformer which are necessary to maintain the thermal balance of the system and stack during operation. The SOFC stack was designed, manufactured and installed into the demo unit by Versa Power Systems (VPS), and it consisted of 64 planar anode supported cells with 550 cm^2 of active area [20]. The SOFC stack is located inside a thermally insulated and gas-tight module designed by VPS. Internal temperature of the stack is measured with thermocouples inserted at various locations inside the stack. Voltage is measured from each cell.

Fuel system gases were analysed at reformer inlet (R_{in}), anode inlet (A_{in}) and anode outlet (A_{out}) (Fig. 1). Anode outlet gas is recycled back to system inlet thus the recycling gas has

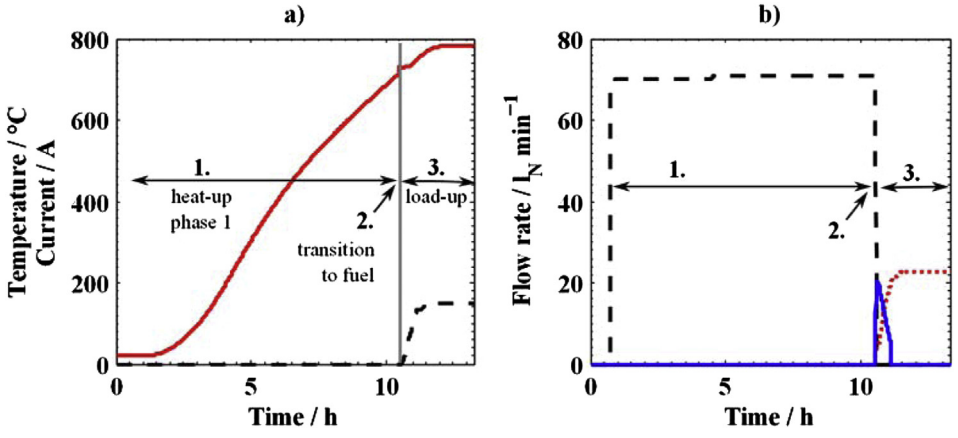

Fig. 2 – Standard start-up (a) Stack temperature (solid line) and current (dashed line) (b) Flow rate of premixed safety gas (dashed line), fuel (dotted line) and steam (solid line).

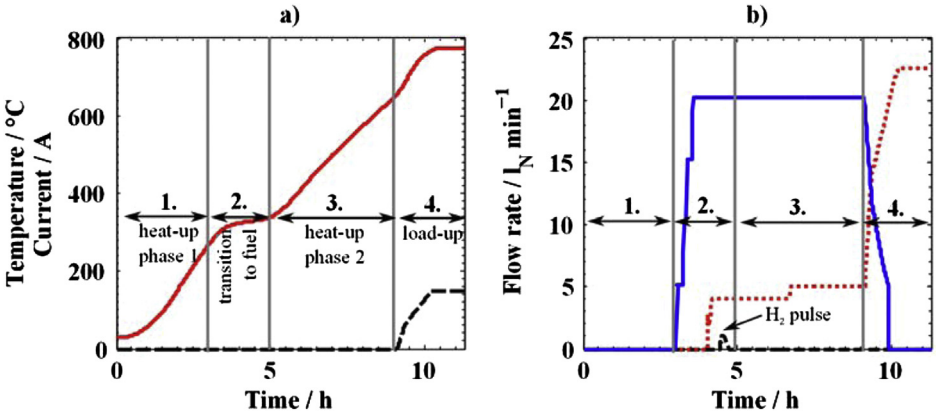

Fig. 3 – Experimental start-up (a) Stack temperature (solid line) and current (dashed line) (b) Flow rate of hydrogen pulse gas (dashed line), fuel (dotted line) and steam (solid line).

the same composition. Continuous gas analysis for CH_4, CO, CO_2, H_2 and O_2 is done with online gas analysis equipment.

The heat-up of the stack and the system was accomplished primarily with the electric heater of the stack module, which heated up the inlet stack air as well as the stack and the surroundings close to the operating temperature (Fig. 1). Secondarily, the heat-up was assisted by a smaller electric heater present in the AOGR loop. The reformer did not have an electric heater thus necessitating the need of temporary hydrogen pulse to start the reforming reactions in the pre-reformer and the stack, which is described in more detail in the following chapters. The rate of temperature change of the stack was below 3 °C min^{-1} during all heat-up cycles.

A standard laboratory style heat-up and start-up cycle has been previously established for this particular SOFC system (Fig. 2). The standard start-up consists of three different phases.

1. Heat-up phase. Premixed safety gas of 4 vol-% hydrogen and 96 vol-% of nitrogen (70 NLPM) is supplied to the fuel system, and air is supplied to air system with a blower (500 NLPM). AOGR is used continuously with an AOGR flow rate above 90 NLPM at all times.
2. Transition to fuel. After the heat-up phase, once the stack temperature is ca. 700 °C, a gradual transition from the premixed safety gas to fuel and steam supply is initiated. Once the transition is completed, premixed safety gas supply is stopped whereas 5 NLPM of natural gas and 20 NLPM of steam are supplied to fuel system.
3. Load-up phase. After transition to fuel gas, a load-up phase is commenced, where the stack current is first ramped up to 150 A, and later to 200 A which is the nominal operating current. During the load-up phase, the natural gas, steam and AOGR flow rates are changed proportionally to the stack current. The external steam supply is stopped at 115 A, once sufficient stack fuel utilization and concurrent transport of oxygen via the cell electrolyte are established. At higher currents, the fuel flow rate is increased, and the fuel system and the stack are kept free of carbon formation by AOGR alone.

In the experimental heat-up cycles devised for this study, the standard heat-up procedure was altered by dividing the heat-up into two distinct phases (Fig. 3).

1. Heat-up phase 1. Firstly, the stack is heated above 200 °C and all other components in the fuel system, e.g. reformer, AOGR blower and heat exchangers, to at least 100 °C (Fig. 3(a)). Similarly to the standard heat-up, AOGR is in operation and cathode air is fed with a blower.
2. Transition to fuel. Firstly, the steam supply is started once the minimum stack temperature is above 200 °C (Fig. 3). For safety reasons, the supply of hydrocarbon fuel was initiated only once the minimum measured in-stack temperature has reached 300 °C. This approach was chosen to eliminate the risk of accidental formation of toxic nickel carbonyl compounds in the SOFC stack. Reformer light-off was accomplished by a short-term hydrogen pulse.

Table 2 – Summary of different system heat-up cycles (HUs).

	Standard	HU1	HU2	HU3
HU phase 1 gas supply	Safety gas	Safety gas	None	None
Stack max. temperature at transition to fuel	700 °C	320 °C	350 °C	400 °C
HU phase 2 gas supply	–	Fuel & steam	Fuel & steam	Fuel & steam

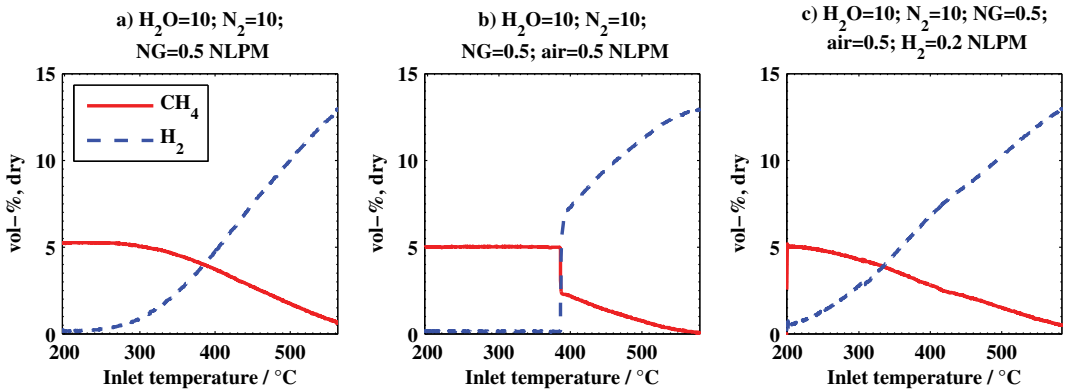

Fig. 4 – Reformer dry outlet gas composition against reformer inlet gas temperature. (a) fuel and steam (run 1), (b) addition of air (run 2) and (c) addition of air and hydrogen at stoichiometric ratio (run 3).

3. Heat-up phase 2. The system is heated up close to stack operating temperature with fuel reformate used as reducing safety gas.
4. Load-up. The load-up procedure remains similar for both standard and experimental heat-up cycles.

In order to assess the feasibility to heat-up a system without premixed safety gases, the demo unit and the SOFC stack were subjected to three different experimental heat-up cycles (HUs). The operational conditions were changed successively to more severe with respect to the possibility of re-oxidizing the stack (Table 2) i.e. higher stack maximum temperature was allowed before the transition to reducing fuel gas was done. Another important distinction between different heat-up cycles should be emphasized. Premixed safety gas (70 NLPM) was supplied during phase 1 only in HU1 (see Table 2). For HU2-3 there was no premixed safety gas supplied at all (see Table 2 and Fig. 3(b)). Instead, the gas during phase 1, circulating in the fuel system by the AOGR blower, was originating from whatever gas was leaking into the fuel system, through the stack or from other sources.

3. Results and discussion

3.1. *Ex-situ reformer experiments*

Fig. 4 illustrates the different qualitative results obtained in the ex-situ experiments. In Fig. 4(a), it can be seen that the catalyst exhibits some activity in steam reforming at temperature as low as 235 °C with test gas of run 1. The conversion of methane increases gradually with the inlet temperature. The inlet temperature at which the methane conversion by steam reforming starts is further referred to as the reformer light-off temperature. In Fig. 4(b), air is added to the test gas, simulating the effect of air leakage to fuel system. The catalyst behaviour is qualitatively very different compared to test gas of run 1, as no methane is reformed before ca. 390 °C. At ca. 390 °C, methane conversion starts abruptly, in other words, reformer light-off occurs.

Apparently, the presence of oxygen in air has an inhibitive effect on the steam reforming reactions at low temperature on this catalyst. In Fig. 4(c), hydrogen is added to the gas stream at stoichiometric ratio with oxygen. In this case, the catalyst exhibits some activity already at 200 °C and the conversion of methane increases gradually with the inlet temperature. This behaviour is qualitatively similar as the one obtained with the test gas of run 1 (Fig. 4(a)), performed with only natural gas and steam and in the absence of oxygen. It appears that the combustion reaction of hydrogen (Eq. (2)) takes place already at 200 °C. As a consequence, molecular oxygen and its inhibiting effect on steam reforming are removed by the reaction (Eq. (2)). Therefore, this enables methane conversion at reformer inlet temperature as low as 200 °C.

Fig. 5 illustrates the effect of the H_2/O_2 ratio on the light-off temperature. The light-off temperature is approximately 390 °C when H_2/O_2 ratio is zero and it decreases with increasing H_2/O_2 ratio to fall below 200 °C at H_2/O_2 ratio of two (corresponding to the stoichiometric ratio of H_2 and O_2).

The results show that methane conversion can be triggered by two ways in the reformer during the heat-up of a SOFC system. Firstly, if no hydrogen is supplied, the reformer inlet gas temperature has to be ca. 400 °C because of the inhibitive effect of oxygen originating from air leakages and recycled by the AOGR loop. Alternatively, the light-off temperature can be decreased by supplying a relatively small amount of hydrogen. Thus the hydrogen production can start already at

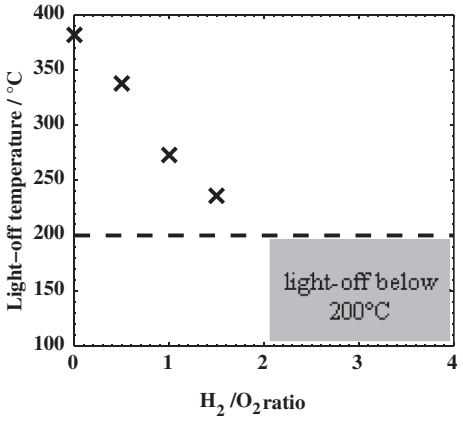

Fig. 5 – The effect of the H_2/O_2 ratio on the light-off temperature of the reformer, results from run 2–7.

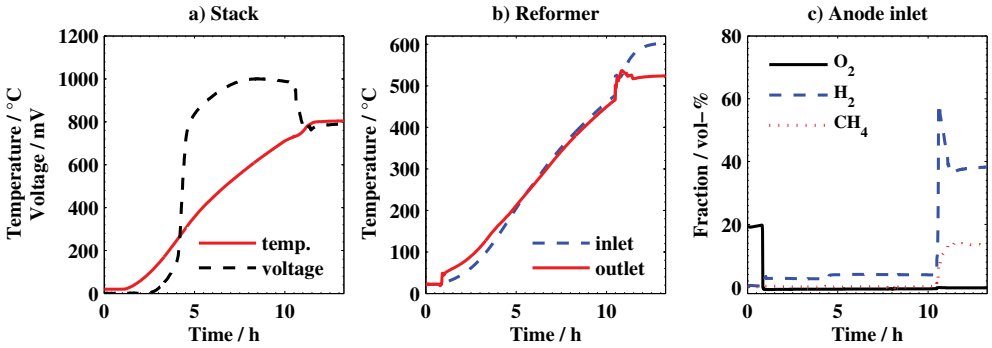

Fig. 6 – Standard heat-up cycle with premixed safety gas (a) stack temperature and average cell voltage, (b) inlet and outlet temperature of the reformer (c) fraction of methane, hydrogen and oxygen in the anode inlet gas on dry basis.

temperature as low as 200 °C. These results suggest that during the heat-up of a SOFC system, a small amount of hydrogen can be supplied to the reformer inlet to trigger the activity of the reformer at low temperature and accomplish the light-off. This is advantageous because the hydrogen produced in the reformer protects the SOFC anode from the damaging effects of re-oxidation. These results are further exploited to design the experiments on system level presented in the next Section 3.2.

3.2. *System heat-up experiments*

3.2.1. *Standard heat-up*

A more detailed planning of the heat-up (HU) cycles was done based on results of the ex-situ experimental results presented in Chapter 3.1. At the time of the experiments, there was no possibility to pre-heat the reformer inlet gas to 400 °C in the 10 kW demo unit, since the pre-heating of the reformer inlet gas was realized only with the fuel system heat exchanger (see Fig. 1). Therefore, it was decided to accomplish the reformer light-off in HUs 2–3 with short-term hydrogen pulse of ca. 1 NLPM during the heat-up cycle.

Firstly, the characteristics of the stack and the reformer during a standard heat-up cycle are depicted in Fig. 6. Before the heat-up is commenced, the hydrogen-containing reducing safety gas supply and AOGR are activated. This is evident at test time ca. 1 h in Fig. 6(c), where the fraction of oxygen is decreased from 21 vol-% to zero and replaced by hydrogen (and nitrogen). Interestingly, the introduction of hydrogen containing safety gas can be observed also by an increase of the reformer T_{outlet} (Fig. 6(b)). This can be explained by the high activity of the precious-metal catalyst used in the pre-reformer. The reaction (Eq. (2)) between the oxygen, leaking into the fuel system (through stack or otherwise), and hydrogen in the safety gas is occurring already at room temperature. Thus the pre-reformer is disposing all oxygen from the anode inlet gas (Fig. 6(c)).

In a standard heat-up, the voltage of the stack starts to increase already at ca. 150 °C stack T_{max} (Fig. 6(a), $t = 3$ h). Significant and faster increase in the stack voltage is present between 250 and 300 °C stack T_{max} (Fig. 6(a), $t = 4–5$ h). The increase of the stack voltage can be interpreted as the start and progression of the reduction process. Additionally, the difference between the reformer outlet and inlet temperature diminishes to zero once the stack temperature reaches 400 °C (Fig. 6(b), $t = 5$ h), and no oxygen is detected anymore in the anode outlet gas, which indicates that oxygen is reacting with hydrogen already in the stack.

After the heat-up, the transition from safety gas to fuel gas and the load-up procedure are observed as an increase of both hydrogen and methane fractions at the anode inlet (Fig. 6(c), $t = 10$ h), and as a decrease in stack voltage (Fig. 6(a)).

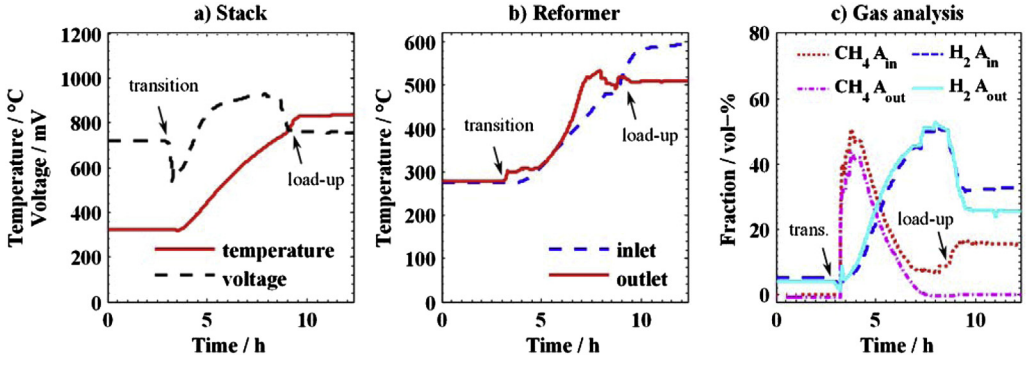

Fig. 7 – Heat-up cycle 1 (a) stack temperature and average cell voltage, (b) inlet and outlet temperature of the reformer (c) fraction of methane and hydrogen in the anode inlet/outlet gas on dry basis.

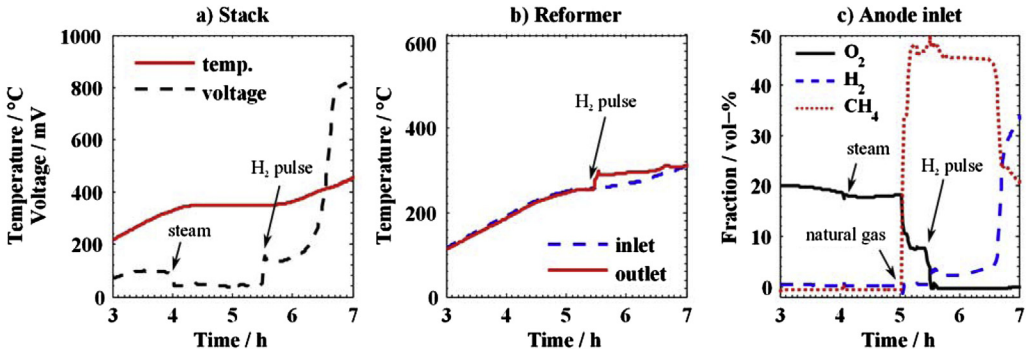

Fig. 8 – Fuel transition of heat-up cycle 2 with no premixed safety gas (a) stack temperature and average cell voltage, (b) inlet and outlet temperature of the reformer (c) fraction of methane, hydrogen and oxygen at the anode inlet on dry basis.

Concurrently, the endothermic steam reforming reactions cause that the T_{outlet} of the pre-reformer decreases ca. 80 °C below the T_{inlet} (Fig. 6(b)).

3.2.2. *Heat-up experiment 1*

The experimental heat-up cycle 1 (HU1) is depicted in Fig. 7. In HU1 the premixed safety gas was still used during heat-up phase 1 (see Table 2) and transition to fuel was done with the stack T_{max} of 320 °C by decreasing the premixed safety gas flow from 70 NLPM to zero and increasing the natural gas and steam flow rates to 5 and 20 NLPM, respectively. The transition to fuel is evident as a drop in the stack voltage (Fig. 7(a), $t = 3$ h), increase in reformer T_{outlet} (Fig. 7(b), $t = 3$ h) and increase in the CH_4 fraction of the fuel system gases (Fig. 7(c), $t = 3$ h). Lower voltage in HU1 compared to standard heat-up can be explained by the higher amount of steam in the fuel gas which decreases the Nernst potential of the cell. The stack voltage increases with the stack temperature as the H_2 fraction of the fuel gas increases ($t = 3$–5 h).

It should be noted that the steam reforming reactions and therefore the majority of the hydrogen production occurs in the SOFC stack throughout the heat-up cycle, since the temperature of the pre-reformer remains lower than the stack. Nearly all methane is converted to hydrogen in the stack once the stack T_{max} reaches 650 °C (Fig. 7(c), $t = 7$ h) and the resulting hydrogen-rich gas is fed back to reformer inlet with AOGR. Concurrently, the reformer inlet temperature is still at ca. 400 °C at that time (Fig. 7(b), $t = 7$ h). The combination of hydrogen-rich inlet gas and low temperature causes that exothermic methanation reaction (reverse to Eq. (1)) takes place in the pre-reformer instead of steam reforming. This can be observed (Fig. 7(b), $t = 6$–9 h) as a second increase of the reformer T_{outlet} above T_{inlet} before the load-up ($t = 8.5$ h) after the first increase caused by oxidation of hydrogen in the reformer (Fig. 7(b), $t = 3$–5 h).

Similarly to the standard heat-up, steam reforming in the pre-reformer starts during the load-up, once more fuel is supplied to the system, and the reformer T_{inlet} increases above 500 °C (Fig. 7(b)). Even though the Ni-cermet of the SOFC stack makes it a very efficient steam reformer during the heat-up process, the amount of hydrogen remains relatively low, below 10 vol-% (dry basis) at the beginning of the heat-up cycle. Marked increase of hydrogen starts to occurs only at higher temperatures, when the stack T_{max} is above 400 °C (Fig. 7(c), $t = 4$ h). Since the pre-reformer has the capability for steam reforming as well, it would be beneficial to operate the reformer at higher temperature during that time i.e. when relatively little methane is reformed in the stack. Therefore, when the fuel supply is started, the reformer T_{inlet} should preferably be above 550 °C to accomplish both reformer light-off and immediate production of H_2-rich gas. However, a pre-reformer is required and very useful also when it is used at lower temperature than the stack, since it removes any oxygen from the anode inlet gas.

3.2.3. *Heat-up experiments 2 and 3*

The experimental heat-up cycle 2 (HU2) is depicted in Fig. 8. It was observed that the system characteristics were similar to HU1 soon after the transition to fuel was done, thus the measurements depicted in Fig. 8 are shown only for this transition phase. In HU2, the stack T_{max} was ca. 350 °C when the transition to fuel gas was done ($t = 4$–5.5 h) and, additionally, no premixed safety gas was supplied to system at all. The reformer light-off was accomplished by a 10 min duration H_2 pulse. The transition to fuel was initiated by starting the steam supply at $t = 4$ h. At $t = 5$ h natural gas supply was started, and at $t = 5.5$ h the hydrogen pulse was done (see Fig. 8 for annotations).

During the phase 1 of the HU2, prior to fuel transition, the oxygen fraction in the fuel system gas is measured to be ca. 21 vol-%, which clearly shows that air is circulating in the fuel system and through the stack (Fig. 8(c), $t = 3$ h). The oxygen concentration is observed to decrease by ca. 1 vol-% before fuel transition at stack $T_{max} > 200$ °C ($t = 3$–4 h), which indicates that oxidation of the Ni-cermet starts to occur. Additionally, the cell voltage decreases once steam supply of 20 NLPM is started (Fig. 8(a), $t = 4$ h). The O_2 fraction decreases significantly, from 18 to 7.5 vol-%, upon introduction of 4 NLPM of natural gas (Fig. 8(c), $t = 5$ h) and the CH_4 fraction in the fuel system gas increases to nearly 50 vol-%, a sign that the flow rate of the air leaking into the fuel system is of the same magnitude i.e. 4 NLPM.

Similarly to the ex-situ reformer experiments no light-off occurred in the pre-reformer even at 250 °C reformer T_{inlet} due to oxygen present in the fuel system (Fig. 8(b), $t = 3$–5.5 h). The reformer light-off and production of H_2 is commenced

only after the H_2 pulse at t = 5.5 h, where a simultaneous decrease of O_2 fraction accompanied with a step-wise increase in the stack voltage, reformer T_{outlet} and H_2 fraction is observed. Interestingly, after turning off the H_2 pulse, the H_2 fraction at the anode outlet and inlet, as well as stack voltage show little or no further increase in nearly 1 h. After t = 6.5 h, a drastic increase in the stack voltage is observed which is explained by faster progressive reduction of the Ni-cermet. Concurrently, the fraction of CH_4 decreases and the H_2 increases suddenly at anode inlet and outlet gas, which is a sure indication of the activation of steam reforming reactions in the SOFC stack.

The experimental heat-up cycle 3 (HU3) was otherwise similar to HU2, but the duration of the H_2 pulse was longer, nearly 1 h, and the stack T_{max} was allowed to increase to 400 °C before starting the natural gas supply into the system. The results with respect to the behaviour of the reformer are alike to HU2 (Fig. 8). Therefore, detailed presentation of the measurements during HU3 is omitted to avoid repetition of the discussion. Instead, the difference of HU3 compared to other heat-up cycles is discussed next in Chapters 3.2.4 and 3.3.

3.2.4. *Reduction and reforming activity of the anode during heat-up*

There are specific differences between the HU1 (safety gas used) and HU2-3 (no safety gas used) with respect to (i) reduction/oxidation behaviour of the stack and (ii) the activity of the Ni-cermet to catalyse steam reforming reactions. This phenomenon is illustrated with Fig. 9, where the flow of fuel and hydrogen, as well as the average cell voltage and the H_2 fraction at anode outlet, are presented for HU1-3. The measurements are plotted as a function of stack T_{max}, a common denominator for the phenomenon under discussion. It should be noted that the stack T_{max} is relative to test time as well, since heating of the stack occurred at relatively steady rate of ca. 2 °C min^{-1} from 300 to 500 °C.

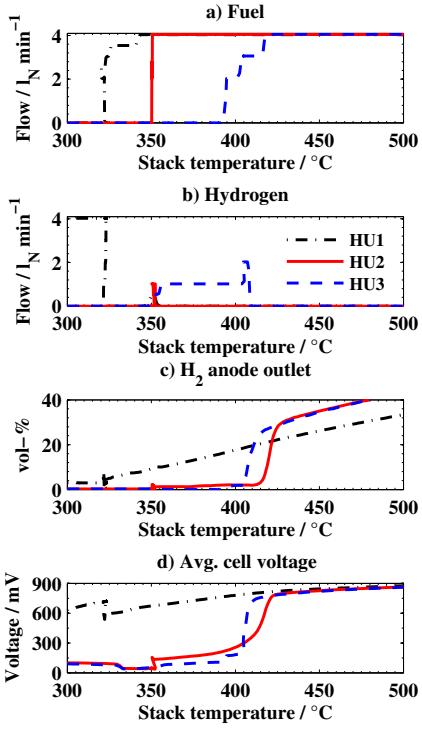

Fig. 9 – Reduction and reforming in the stack for HU1-3 (a) fuel flow (b) hydrogen flow, (c) fraction of H_2 in anode outlet gas and (d) average cell voltage.

Qualitatively, it is evident that in HU1 the stack is already more reduced (stack voltage is higher) and also catalytically active with respect to steam reforming. In HU1, the H_2 fraction at the anode outlet as well as voltage increases steadily with the stack temperature (Fig. 9(c–d)), occurring immediately when the H_2 supply is stopped and fuel supply started (Fig. 9(a–b)). Moreover, the results show that the steam reforming reactions and H_2 production in the stack can start already at 300–350 °C.

In HU2, the short-term H_2 pulse of 10 min duration is triggering both reduction and reforming activity in the stack, observed as a stepwise transition for both H_2 and stack voltage (Fig. 9(c–d)). However, the stack has to heat up ca. 70 °C more to 420 °C (in 1 h, see also Fig. 8) until the reduction of the stack has proceeded to a level where a notable recovery of the stack voltage, as well as in increased reforming activity is observed.

In HU3, however, the recovery of stack voltage as well as reforming activity is occurring nearly simultaneously with the introduction of the natural gas. Faster recovery can be related to longer duration of the H_2 pulse. The H_2 flow is started once the stack temperature reached 350 °C, and the reduction process of the stack can proceed while the stack heats up to 400 °C (Fig. 9(b)). Thus the reduction is completed faster in HU3 once the natural gas supply is initiated. However, the 1 NLPM of H_2 in HU3 is insufficient to reduce the entire active cell area since no H_2 is detected in the anode outlet gas at first. The H_2 is present in anode outlet gas only after transition to fuel is complete.

Based on the results it is clear that in HU2-3 both the electrochemical, as well as steam reforming activity, are first inhibited by the oxidation of the Ni-cermet already at lower temperature than 350 °C for stack T_{max}. Additionally, to realize the reduction of the Ni-cermet after oxidation has occurred at low temperature, all oxygen has be removed from the anode inlet gas (see Fig. 8) and replaced with high enough amount of hydrogen, so that there is hydrogen present at the anode outlet gas as well. Otherwise, it appears that the Ni-cermet of the stack will remain in oxidized state and will not start the steam reforming reactions, and the accompanied production of reducing hydrogen gas.

3.3. *Effect of the heat-up experiments on the SOFC performance*

Voltage characteristics of the SOFC stack is commonly used as a performance indicator. Thus the effects of the different heat-up cycles on the SOFC can be assessed by observing changes in the stack or individual cell voltages [6]. If the experiments cause permanent damage to the cells e.g. due to re-oxidation, it would be recorded as a stack voltage decrease.

Voltage characteristics of the SOFC stack were investigated by conducting a load-up cycle to 150 A (0.273 A cm^{-2}) after each heat-up experiment and allowing the system to stabilize for 20 h (Fig. 10(a–c)). After the stabilization, the individual

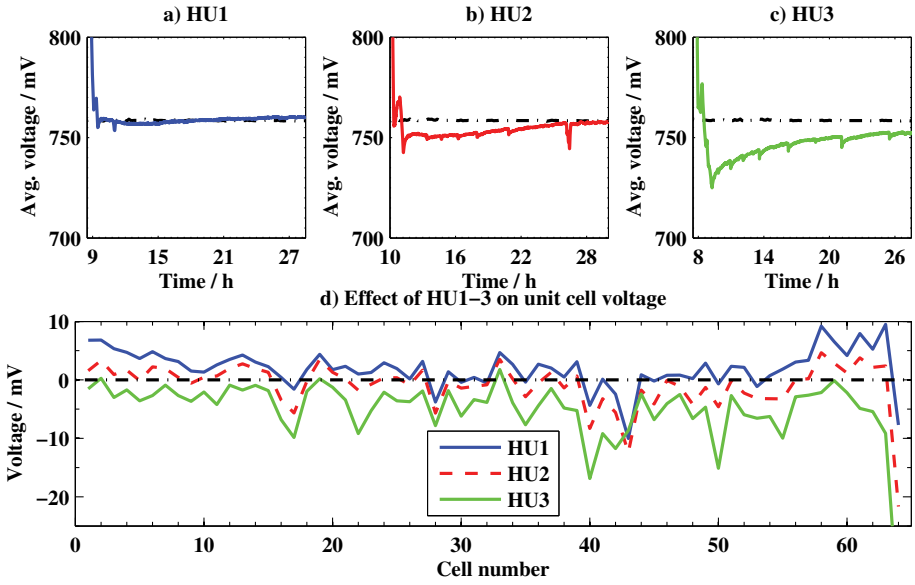

Fig. 10 – Effect of HU1-3 on stack performance. (a–c) average cell voltage after load-up for HU1-3 (solid line) and prior to experiments (dashed line) (d) difference in unit cell voltages after each heat-up cycle.

voltage measurements from all 64 cells of the stack were averaged for a period of 1 h. Then, a difference was calculated to the measurements at 150 A prior to performing any of the experiments HU1-3 (Fig. 10(d)). The average cell voltage prior to HU1-3 is also shown in Fig. 10(a–c).

The majority of the cells in the stack do not show any performance deterioration after the HU1-2 compared to the values recorded at 150 A prior to experiments (Fig. 10(a),(b) and (d)). However, after the HU3 the average cell voltage is ca. 6 mV lower at the end of the stabilization period (Fig. 10(c)), and nearly all cells exhibit voltage decrease (Fig. 10(d)). In the HU3 the stack maximum temperature was allowed to increase up to 400 °C before the supply of fuel gas was started. Thus it is possible that the higher temperatures used in HU3 may have caused too severe oxidation of the anode, thus damaging the stack.

However, the differences of the cell voltages compared to prior measurements in Fig. 10(d) are small and within 10 mV for the majority of the cells. Moreover, some of the cells exhibit increased voltage compared to prior measurement. This indicates that the resulting differences in the voltage between the heat-up cycles can be partly explained by other effects as well e.g. by the variation of the in-stack temperature distribution due to small hysteresis of the plant controllers. Additionally, deep thermal cycling of a SOFC stack down to room temperature can cause damage and performance loss of the stack even with premixed reducing gas, and this phenomena can also contribute to the apparent lower cell voltage with increased number of heat-up cycles.

Therefore, this comparison of the cell voltage distribution with respect to the effect of the heat-up cycles should be treated as indicative rather than conclusive since there are other mechanisms which can affect the performance of cells. However, the results show that the stack can withstand a heat-up cycle with fuel reformate and AOGR without any significant performance deterioration. Moreover, stack temperatures below 350 °C appears to be a more beneficial region to introduce the fuel gas and trigger the reforming reactions to produce hydrogen-rich reducing gas because (i) performance loss was measured after HU3 when the stack was heated up to 400 °C before starting the fuel supply and (ii) the Ni-cermet is oxidized already below 350 °C which prevents steam reforming reactions.

4. Conclusions

The results of this study clearly show that it is essential to investigate the characteristic operation of the system pre-reformer to accomplish a safe heat-up cycle. Furthermore, the interactions with other system components e.g. air leakages and the choice for system layout, such as the use of AOGR, will affect the feasibility of any heat-up strategy and have to be taken into account.

The light-off temperature, i.e. start of the reforming reactions in a pre-reformer, is significantly affected by the use of AOGR and any leakages of air to the fuel system, through stack or otherwise. The light-off temperature is increased by ca. 200 °C when oxygen is present in the reformer inlet gas. However, it is possible to accomplish lower reformer light-off temperatures by adding hydrogen to the reformer inlet.

SOFC stack is an efficient steam reformer due to high amount of catalytically active nickel in the anode cermet, and thus is an obvious solution to produce the hydrogen-rich reducing gas from the fuel during system heat-up. It is observed, that the SOFC stack can start sufficient steam reforming and production of hydrogen-rich reducing gas at temperatures above 400 °C. However, oxidation of the anode Ni-cermet in system conditions can proceed already below 350 °C, which inhibits the reforming activity of the anode. Thus, the usage of a pre-reformer to remove trace oxygen from the anode inlet gas is required with AOGR, since any air

leakages to fuel system will retain the anode in oxidized state. Moreover, some performance loss was measured when the stack was heated to 400 °C before fuel supply was started. Therefore, it is recommended that the supply of hydrogen-rich reducing gas is started already below 350 °C, or as low temperature as possible, to prevent oxidation of the Ni-cermet.

During the system experiments it was noted that sufficient temperatures for pre-reformer light-off were not possible by relying only on the heat recuperated from the fuel system heat exchanger. Thus electrically or otherwise assisted heating of the pre-reformer (i) to 400 °C enables reformer light-off without the short-term hydrogen pulse, thus simplifying the system layout even further and (ii) above 500 °C shifts the hydrogen production from the stack to pre-reformer, which increases the amount of hydrogen when the reforming activity of the stack is still low and thus enhances the quality of the reducing gas. Additionally, if the pre-reformer would be mainly responsible of the hydrogen production, the stack temperature can potentially be lower than 300 °C when the fuel is introduced to the system. This would significantly decrease the risk of oxidizing the Ni-cermet anode.

The results show that a heat-up from room temperature to the operating temperature of SOFC stack is possible without premixed gas and without significant loss of stack performance. This finding allows reducing the premixed gas storage capacity in a SOFC system and thus the physical size of the system as well capital and servicing costs.

Acknowledgements

Funding for this study was obtained through the projects SofcPower and RealDemo. The Finnish Funding Agency for Technology and Innovation (TEKES) as well as the companies participating in the project are gratefully acknowledged for their financial support. M. Halinen would like to thank T. Hottinen from Wärtsilä Finland and M. Pastula from Versa Power Systems for the helpful discussions related to the system experiments. M. Rautanen from VTT is acknowledged for his essential assistance in the experiments.

REFERENCES

[1] Selimovic A, Kemm M, Torisson T, Assadi M. Steady state and transient thermal stress analysis in planar solid oxide fuel cells. J Power Sources 2005;145:463–9.
[2] Ettler M, Timmermann H, Malzbender J, Weber A, Menzler NH. Durability of Ni anodes during reoxidation cycles. J Power Sources 2010;195:5452–67.
[3] Jeangros Q, Faes A, Wagner JB, Hansen TW, Aschauer U, Van herle J, et al. In situ redox cycle of a nickel–YSZ fuel cell anode in an environmental transmission electron microscope. Acta Mater 2010;58(14):4578–89.
[4] Pihlatie M, Kaiser A, Mogensen M. Redox stability of SOFC: thermal analysis of Ni–YSZ composites. Solid State Ionics 2009;180:1100–12.
[5] Laurencin J, Roche V, Jaboutian C, Kieffer I, Mougin J, Steil MC. Ni-8YSZ cermet re-oxidation of anode supported solid oxide fuel cell: from kinetics measurements to mechanical damage prediction. Int J Hydrogen Energy 2012;37:12557–73.
[6] Brabandt J, Fang Q, Schimanke D, Heinrich M, Mai BE, Wunderlich C. System relevant redox cycling in SOFC stacks. ECS Trans 2011;35(1):243–9.
[7] Rasmussen JFB, Hendriksen PV, Hagen A. Study of internal and external leaks in tests of anode-supported SOFCs. Fuel Cells 2008;8(6):385–93.
[8] Peters R, Deja R, Blum L, Pennanen P, Kiviaho J, Hakala T. Analysis of solid oxide fuel cell system concepts with anode recycling. Int J Hydrogen Energy 2013;38(16):6809–20.
[9] Halinen M, Rautanen M, Saarinen J, Pennanen J, Pohjoranta A, Kiviaho J, et al. Performance of a 10 kW SOFC demonstration unit. ECS Trans 2011;35(1):113–20.
[10] Dietrich RU, Oelze J, Lindermeir A, Spitta C, Steffen M, Küster T, et al. Efficiency gain of solid oxide fuel cell systems by using anode offgas recycle – results for a small scale propane driven unit. J Power Sources 2011;196(17):7152–60.
[11] Powell M, Meinhardt K, Sprenkle V, Chick L, McVay G. Demonstration of a highly efficient solid oxide fuel cell power system using adiabatic steam reforming and anode gas recirculation. J Power Sources 2012;205:377–84.
[12] Rancruel D, von Spakovsky M. Investigation of the start-up strategy for a solid oxide fuel cell based auxiliary power unit under transient conditions. Int J Thermodyn 2005;8(2):103–13.
[13] Apfel H, Rzepka M, Tu H, Stimming U. Thermal start-up behaviour and thermal management of SOFC's. J Power Sources 2006;154:370–8.
[14] Ki J, Kim D. Computational model to predict thermal dynamics of planar solid oxide fuel cell. J Power Sources 2010;195:3186–200.
[15] Jiang W, Fang RF, Khan J, Dougal R. Control strategies for start-up and part-load operation of solid oxide fuel Cell/Gas turbine hybrid system. J Fuel Cell Sci Technol 2010;7:0110161–9.
[16] Damm LD, Fedorov AG. Reduced-order transient thermal modeling for SOFC heating and cooling. J Power Sources 2006;159:956–67.
[17] Chen MH, Jiang TL. The analyses of the start-up process of a planar, anode-supported solid oxide fuel cell using three different start-up procedures. J Power Sources 2012;220:331–41.
[18] Petruzzi L, Cocchi S, Fineschi F. A global thermo-electrochemical model for SOFC systems design and engineering. J Power Sources 2003;118:96–107.
[19] Halinen M, Thomann O, Kiviaho J. Effect of anode off-gas recycling on reforming of natural gas for solid oxide fuel cell systems. Fuel Cells 2012;12(5):754–60.
[20] Borglum B, Tang E, Pastula M. Development of solid oxide fuel cells at versa power systems. ECS Trans 2011;35(1):63–9.

PUBLICATION V

Glass coated compressible solid oxide fuel cell seals

Journal of Power Sources 2014,
Vol. 247, pp. 243–248.

Journal of Power Sources 247 (2014) 243–248

Contents lists available at ScienceDirect

Journal of Power Sources

journal homepage: www.elsevier.com/locate/jpowsour

Glass coated compressible solid oxide fuel cell seals

M. Rautanen*, O. Thomann, O. Himanen, J. Tallgren, J. Kiviaho

VTT Technical Research Centre of Finland, Fuel Cells, P.O. Box 1000, Biologinkuja 5, Espoo, FI-02044 VTT, Finland

HIGHLIGHTS

- A novel sealing material for solid oxide fuel cell stacks: conformable Thermiculite 866 core with thin glass coating.
- A method to coat thin glass layers using an organic carrier.
- Leak test results of glass coated seals.
- Stack test results using glass coated seals.

ARTICLE INFO

Article history:
Received 8 May 2013
Received in revised form
23 July 2013
Accepted 21 August 2013
Available online 31 August 2013

Keywords:
SOFC
Seal
Thermiculite 866
Glass
Leak
Stack

ABSTRACT

With the growing footprint of solid oxide fuel cell stacks, there is a need to extend the operating range of compressible gaskets towards lower stress levels. This article describes a method to manufacture SOFC seals by coating a compressible sealing material (Thermiculite 866) with glass to obtain good sealing performance even at compression stresses as low as 0.1 MPa. Glass layer can be coated using an organic carrier consisting of terpineol, ethanol and ethyl cellulose. The coated seals can be heat treated by simply ramping the temperature up to operating temperature at 60 Kh^{-1} and therefore no extra steps, which are typical to glass seals, are required. Coated seals were manufactured using this route and evaluated both ex-situ and in a real stack. Leak rates of 0.1–0.3 ml $(m\ min)^{-1}$ were measured at 2–25 mbar overpressure using 50/50 H_2/N_2. A 30-cell stack was manufactured and tested using coated seals. At nominal operating conditions of 0.25 A cm^{-2} and 650 °C average cathode temperature, 46% fuel utilization and 20% air utilization the stack had a total hydrogen cross leak of 60 ml min^{-1} corresponding to 0.7% of the inlet hydrogen flow rate.

1. Introduction

Traditionally solid oxide fuel cell (SOFC) stack seals have been either bonding seals (glass/glass-ceramic or brazes) or non-bonding (compressible) seals [1,2]. Bonding seals wet adjacent surfaces forming a very gas tight structure with little interfacial leakages. The usual drawback is that the bonding seals are susceptible to thermo-mechanical stresses especially in thermal cycling. Properties of glasses or glass-ceramics, such as coefficient of thermal expansion (CTE), viscosity and porosity, often change over time. During long term operation these changes can create additional thermo-mechanical stresses leading to seal failure [3,4]. Non-bonding compressible seals are more resistant to thermo-mechanical stresses as they are not rigidly bonded to adjacent components. However, their leak rates are usually higher and dominated by the interfacial leak paths, especially at low compression stresses [5,6]. Compressible seals also require much higher compressive stresses compared to bonding seals, usually at least 2 MPa [7–9]. For example, in the results presented by Thomann et al. [10], with a cell footprint of 100 cm^2, the applied load on the stack was 2000 kg corresponding to roughly 4 MPa on the seals. If this stack was scaled up, the need for the applied load would naturally increase further complicating the mechanical design of the compression system.

Compressive stress is needed in SOFC stacks to ensure adequate sealing performance and to establish a good electrical contact between cells and interconnects. A general trend in SOFC stacks is towards larger cells and therefore towards larger stack footprints creating a need for higher compression on stacks, particularly the ones using compressible seals. This leads to heavier and more complicated compression systems. Compression rods usually need to go through the stack module heat insulation creating additional heat losses. Less compression would enable the use of thinner, less robust stack components. Therefore minimizing compressive stress required on the stack seals while maintaining the easy handling and assembly of the compressible seals would be beneficial.

* Corresponding author. Tel.: +358 405387552; fax: +358 207227048.
E-mail address: markus.rautanen@vtt.fi (M. Rautanen).

0378-7753/$ – see front matter © 2013 Elsevier B.V. All rights reserved.
http://dx.doi.org/10.1016/j.jpowsour.2013.08.085

In recent years, there has been some activity to develop composite seals combining properties from both compressible seals and glass-ceramic seals. The idea is to have a seal which would inherit its mechanical properties from the compressible core but, as opposed to standard compressive seals, would have very low interfacial leak rates because of the compliant surface coating. This would enable the compressible core to deform as a function of thermo-mechanical stresses without causing failure of the seal. Chou et al. have been experimenting with the hybrid sealing concept using different micas as substrates and glass or silver foil to seal the interfacial leak paths [5,6,11–15].

The hybrid seal developed at VTT Technical Research Centre of Finland is a composite structure consisting of compressible Thermiculite 866 [16] core coated with glass using an organic carrier. This method enables easy stack manufacturing as the seal can be coated beforehand and then cut and handled exactly in the same way as traditional compressible gaskets. The organic carrier is burned out in the first heat up and the remaining glass forms a thin conformable interlayer between the seal core and adjacent stack parts. The seal core is able to deform when subjected to stress and therefore can compensate e.g. differences in thermal expansion coefficients of adjacent components. A major advantage of the conformable core is also its ability to compensate for manufacturing tolerances of the adjacent components. Thermiculite 866 core is also less permeable compared to commonly used mica papers since voids between the platelets are filled with a fine grade of steatite. This paper presents a manufacturing method for the coated seals, ex-situ leakage test results and stack test results from a stack utilizing the sealing materials presented in this article.

2. Experimental

2.1. Seal manufacturing

Materials for the hybrid seals were chosen to target stack operation at around 700 °C. The chosen core material was Thermiculite 866 (Flexitallic Ltd) [16]. The glass layer was chosen to be relatively thin (<20 μm) so that the glass itself could be quite low in viscosity. The glass chosen for this study was a commercial glass material having a softening temperature of 650 °C.

Coating of the Thermiculite 866 seals was conducted using a mixture of glass powder and organic carrier. The organic carrier consisted of terpineol (mixture of isomers, Merck), ethanol (ETAX B, Altia) and ethyl cellulose (Fisher Scientific). Ethyl cellulose was mixed with terpineol and ethanol at 35 °C with a magnetic stirrer for 24 h. After that, glass powder was added and the mixture was stirred for 1 h. Table 1 presents typical compositions of the organic carriers and glass to organic ratios used in this study. When coating with brush/spatula/roller, a thicker coating paste proved easy to use and good coverage was achieved easily with a single layer. When using wet spraying, the carrier was diluted with more ethanol to achieve a lower viscosity of around 10–30 cSt which was suitable for the spray gun (U-POL Maximum HVLP mini with 1.0 mm nozzle). Several layers were sprayed from a distance of 10–20 cm.

Table 1
Typical composition of organic carrier and glass to organic ratio with different coating methods.

Coating method	Terpineol/w%	Ethanol/w%	Ethyl cellulose/w%	Glass to organic ratio/w/w
Brush/spatula/roller	81	15	4	2:1
Wet spraying	24	75	1	1:2

After applying the coating, the coated Thermiculite 866 sheets were dried at 75 °C for 2 h and then cut to the required shape. All the seals were heated from room temperature up to 700 °C using 60 Kh^{-1} ramp rate.

2.2. Ex-situ leak tests

Ex-situ leak tests were conducted on ring-shaped seals having 40 mm outer diameter and 5 mm width. The seal was placed on top of 20 mm thick Crofer 22 H (Thyssenkrupp VDM) plate. A 1 mm thick Crofer 22 H plate was placed on top of it and weight plates on top of the 1 mm plate. Gas was fed to the middle of the seal through the thick bottom plate. Fig. 1 presents the experimental setup for ex-situ leak rate measurements. Mass flow controllers fed a chosen gas mixture to the sample line and exhaust line. Sample pressure was controlled with a pressure controller which vents a sufficient flow of gas to the exhaust to keep the upstream pressure at a set level. During heat up, air was fed to the samples to ensure a complete organic burn off.

After heat up, samples were exposed to a 25 mbar overpressure using 50/50 mix of H_2/N_2 at 700 °C. Periodical leak rate measurements were conducted by shutting off the valve V 1 and measuring the pressure decay. A vessel of a known volume was connected to the sample enabling leak rate as a function of pressure to be calculated from the pressure decay curve. Based on the ideal gas assumption, the leak rate is proportional to the slope of the pressure decay curve and therefore the leak rate can be written

$$\dot{Q} = V\frac{T_{\mathrm{ntp}}}{Tp_{\mathrm{ntp}}}\frac{\mathrm{d}p}{\mathrm{d}t},$$

where V is the combined volume of the vessel and the sample, T is the average temperature of the gas in the volume and T_{ntp} and p_{ntp} are normal temperature and pressure. To calculate the leak rate one needs to evaluate dp/dt over the measurement data. If one wants to calculate leak rate at a specific pressure from the data which is a set of points taken at regular intervals, one could approximate dp/dt by

$$\frac{\mathrm{d}p}{\mathrm{d}t} \cong \frac{p_i - p_{i-1}}{t_i - t_{i-1}}.$$

If the sampling rate has been sufficient, the difference $p_i - p_{i-1}$ is bound to be small. As the uncertainty of dp/dt is proportional the uncertainty of the pressure measurement

$$\varepsilon\left(\frac{\mathrm{d}p}{\mathrm{d}t}\right) \propto 2\varepsilon(p),$$

this approach would yield very inaccurate results. To overcome this, a third degree polynomial was fitted to the $p(t)$ − data using least squares method thus minimizing the random uncertainty of the $p(t)$ measurement. Goodness of the fits were analyzed by calculating relative standard deviation of residuals and in case those were over

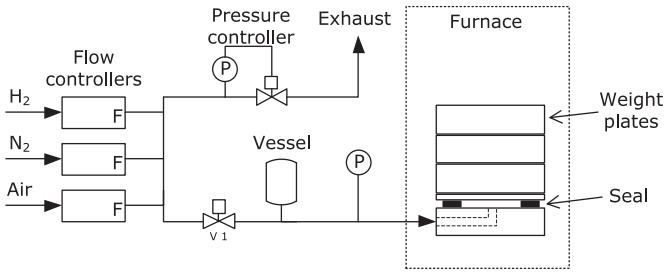

Fig. 1. Measurement setup for the ex-situ leak rate test. Four samples were tested simultaneously, although in here only one is shown for clarity.

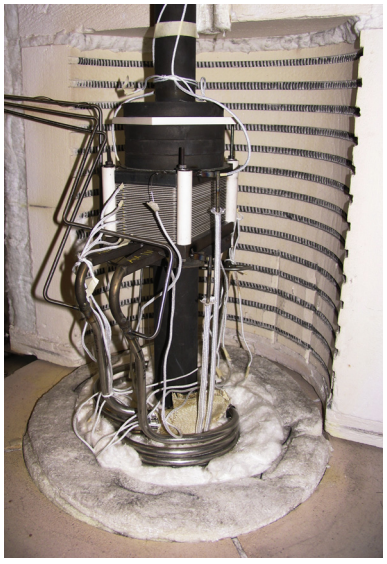

Fig. 2. The 30-cell stack before testing.

1.0% fits were discarded. The fitted polynomial was then differentiated to obtain leak rate as a function of pressure. As the accuracy of the pressure transducer is very good (±0.5 mbar) it can be concluded that the accuracy of the pressure measurement has negligible effect on the results. The accuracy of the gas temperature measurement was ±15 °C corresponding to a leak rate uncertainty of 5%.

Quantifying leak rate using the pressure decay methodology described above offers the advantage of relatively simple measurement which can be easily automated. The disadvantage of the method is that by using it one only measures leak rate indirectly by measuring the pressure inside the volume, which is dependent on the flow rates of species through the seal boundary. By using other gas than air, there is always a concentration difference over the seal and therefore also a flux of species from outside to inside by diffusion, which has an effect on the observed flow rate.

2.3. Stack test

In addition to the ex-situ tests, a 30-cell stack was manufactured and tested together with Elcogen. The stack utilized Elcogen ASC-10B cells and ferritic steel interconnects. The seals were made of coated Thermiculite 866 except for the seal against the electrolyte which was made of glass, as it needed to be thinner than the thinnest coated seal that was achievable at the time the work was carried out. Fig. 2 shows the 30-cell stack in a furnace before testing. The compression on the stack was provided through a pipe seen at the upper end of the picture. Pipe coils seen at the bottom of the furnace acted as pre-heaters for air and fuel. On the right side of the picture current collectors attaching to the end plates are seen. Pipelines to measure stack pressures are seen to exit the furnace to the left. The stack was heated up using air flow at both anode and cathode. After reaching the operating temperature, nitrogen was fed to the anode side and afterwards reduction was carried out with hydrogen in nitrogen mixture. During stack polarization, hydrogen and air flows were increased while increasing current and nitrogen flow was kept constant at 8.5 NLPM.

Cross leakages were quantified by measuring steam and oxygen content from cathode and anode outlets. Steam was measured with Vaisala Humicap HMT-337 relative humidity meter (±1% RH) and oxygen with Sick TRANSIC100LP (±0.2% – units O_2). Zero level of the oxygen probe was calibrated with nitrogen and the accuracy was determined to be 0.05% – units below 1% O_2. Oxygen cross leak was calculated before reduction as

$$\dot{Q}_{O_2}^{\text{cross}} = X_{O_2}^{A,\text{out}} \dot{Q}_{N_2}^{A,\text{in}}$$

The hydrogen cross leak after reduction was calculated as

$$\dot{Q}_{H_2}^{\text{cross}} = \left(X_{H_2O}^{C,\text{out}} - X_{H_2O}^{C,\text{in}}\right)\left(\dot{Q}_{\text{air}}^{C,\text{in}} - n_{\text{cells}}\frac{I}{4F}\frac{RT_{\text{ntp}}}{p_{\text{ntp}}}\right),$$

where terms denoted with X are measured oxygen and steam volumetric fractions, n_{cells} is the number of cells in the stack (30), I is the current drawn from the stack and F is the Faradic constant. These calculations are based on the assumption that the leak rates between ambient and anode/cathode and the nitrogen cross leak are small compared to total flow rates.

3. Results and discussion

3.1. Seal manufacturing

Samples for the SEM analysis were cut out of coated Thermiculite 866 sheets and placed between two 1 mm Crofer 22 H sheets. The samples underwent a heat treatment described in Section 2.1 with a 50 h dwell at 700 °C. Fig. 3 shows SEM cross sections of the prepared samples. The horizontal platelets in the Thermiculite 866 are exfoliated vermiculite and the filler between them is steatite. The figure shows the advantage of this material over conventional mica papers as the inherent voids in the flaky mica structure are filled with steatite and therefore the gas tightness is improved. The compressibility of this material is also superior to conventional mica papers [9]. Thin glass layers of 2–10 μm are seen at the interfaces of Thermiculite 866 and Crofer 22 H plates. It can be noted that the glass has accommodated very well to the surface roughness of the Thermiculite 866 and even penetrated into its

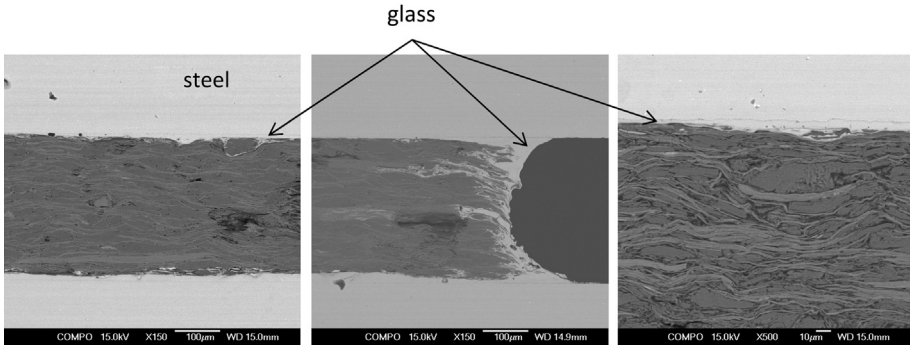

Fig. 3. SEM cross sections of the coated seals. From left to right: middle section of the seal, end of the seal and close up of the steel/glass/Thermiculite 866 interface.

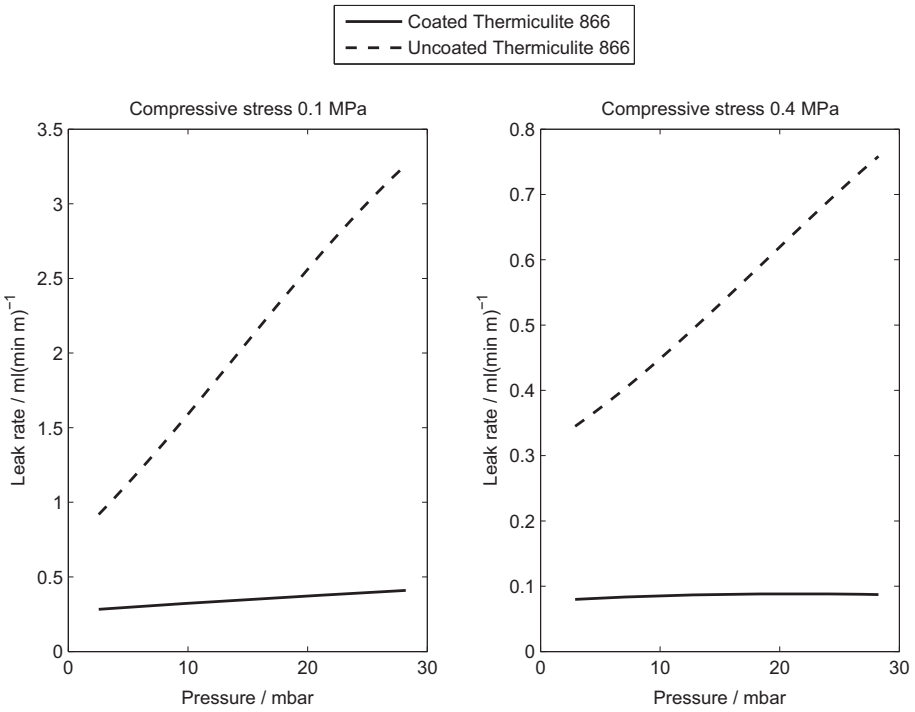

Fig. 4. Leak rates of coated and uncoated Thermiculite 866 at compressive stress of 0.1 MPa (left) and 0.4 MPa (right) with 50/50H_2/N_2. Note the different scales of the vertical axes.

pores. The low initial viscosity of the glass layer provides good conformability to the Thermiculite 866 core and to any surface imperfections on the adjacent components.

3.2. Ex-situ leak tests

Fig. 4 presents leak rates of the samples as a function of pressure at 0.1 MPa and 0.4 MPa compressive stress. From this figure it can be noticed that the surface coating decreases the leak rate of Thermiculite 866, especially at low compression stress levels. The coated Thermiculite 866 seals show leak rates of 0.1–0.3 ml (m min)$^{-1}$, which is a reduction of 60–90% compared to uncoated samples which showed leak rates of 0.3–3 ml (m min)$^{-1}$. Chou et al. have measured leak rates below 1 ml (m min)$^{-1}$ using mica papers with glass interlayers at compressive stresses of 0.04–0.7 MPa and less than 0.1 ml (m min)$^{-1}$ using glass sealing [5,12,15,17]. The tests have been carried out either with helium or 2.64% H_2 in humidified Ar. Although different conditions make direct comparison difficult, it is clear that the results presented in this paper are at a comparable level to the hybrid seals developed by Chou et al.

Fig. 5 presents leak rates of coated and uncoated Thermiculite 866 with different gas compositions and overpressures. The leak rate of the uncoated sample clearly depends on both overpressure and the hydrogen concentration but the leak rate of the coated sample only depends on the hydrogen concentration. As the driving potentials, overpressure and concentration gradients, are same for both measurements, it can be concluded that the coating effectively

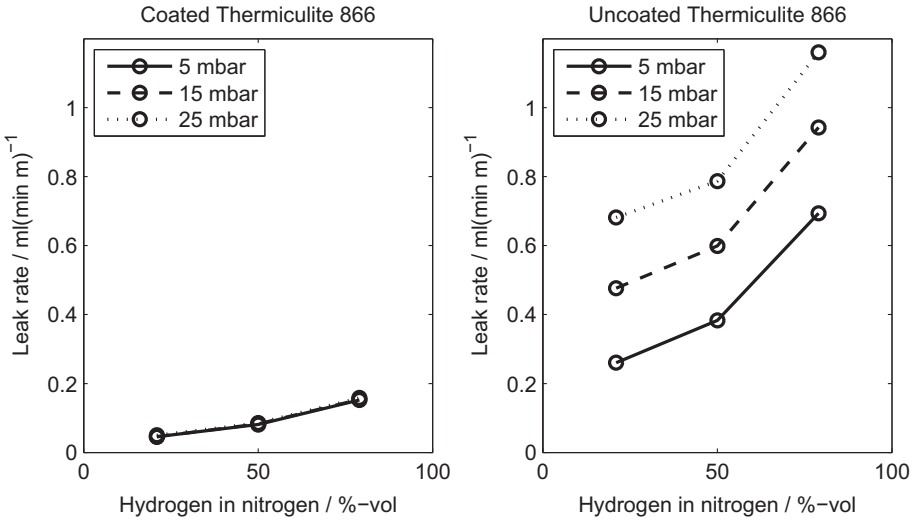

Fig. 5. Leak rates of coated (left) and uncoated (right) Thermiculite 866 at different overpressures as a function of hydrogen concentration. Compressive stress is 0.4 MPa.

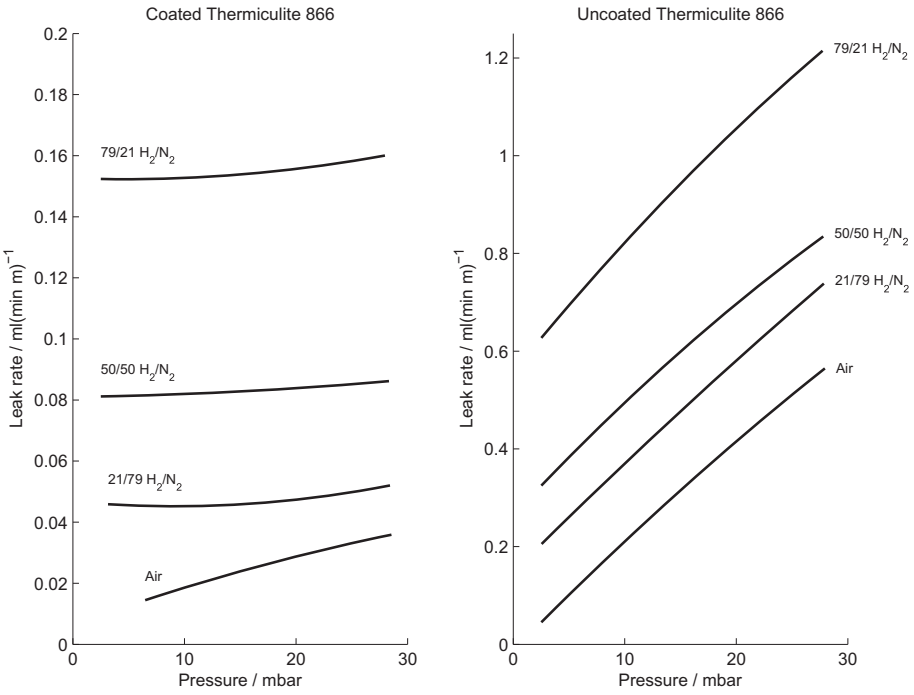

Fig. 6. Leak rates of coated (left) and uncoated (right) Thermiculite 866 as a function of overpressure with 0.4 MPa compression stress with different gas compositions.

blocks the direct leak paths and the remaining leak rate is due to diffusion rather than advection. This is further shown by looking at the curves measured with air (Fig. 6). Extrapolating the curves one obtains a zero leak rate at zero pressure difference when other gas compositions yield a non-zero leak rate also at zero pressure difference. The negligible dependency of the overpressure on the diffusive leak rate can understood by considering Fick's law of diffusion written for a component A using total concentration c_{TOT} total pressure p_{TOT} and the molar fraction x_A:

$$J_A = -D_{AB}\nabla c_A = -C_{TOT}D_{AB}\nabla x_A = -\frac{p_{TOT}}{RT}D_{AB}\nabla x_A.$$

From this equation one can notice that varying the absolute overpressure p_{TOT} in a range of ~1000–1030 mbar induces very little effect on the concentration driven leak rate. Although the real situation is more complex, the concentration dependency of the leak rates should be carefully considered as different research groups use very different gas compositions and overpressures for leak tests, such as 3% H_2 in nitrogen or argon, 100% H_2 or 100% He.

3.3. Stack test

Hydrogen cross leak was measured with purge gas and at nominal operating conditions (Table 2). Table 3 shows stack flows, measured values and the calculated cross leaks at different operating conditions. The air inlet humidity was constant 0.08%. Before reduction, the O_2 cross leak was 8 ml min^{-1}. After reduction the H_2 leak rate using purge gas was 10 ml min^{-1} and 60 ml min^{-1} at nominal operating conditions. Fig. 7 shows the hydrogen cross leak as a function of average hydrogen concentration between anode inlet and outlet during the test. The concentration dependency of the leak rate can be clearly noticed as in the ex-situ tests. During nominal operating conditions the overpressure at cathode was higher than the pressure at anode and therefore the measured hydrogen leak is against the pressure gradient which suggests that the remaining leak rate is due to diffusion rather than advection through the direct flow paths. However, as the measured quantity in stack test is hydrogen leak rather than total leak, even if the leak was totally advective of nature, the hydrogen leak rate would increase as a function of hydrogen concentration in the gas which makes it difficult to draw the final conclusions. At nominal operating conditions of 0.25 A cm^{-2} current density, 46% fuel utilization and 20% air utilization the stack had a total hydrogen cross leak of 60 ml min^{-1}. The hydrogen cross leak value at nominal operating conditions corresponds to a loss of 0.7% of the inlet hydrogen flow, which can be considered a very promising result for the first test using coated Thermiculite 866 seals in a real SOFC stack.

Table 2
Nominal operating conditions.

Cells	30 pcs Elcogen ASC-10B
Flow configuration	Co-flow
Active area	81 cm^2
Cathode inlet temperature	590 °C
Cathode outlet temperature	700 °C
Current density	0.25 A cm^{-2}
Air utilization	22%
Fuel utilization	46%
Pressure difference over anode	3 mbar
Cathode inlet pressure	13 mbar
Cathode outlet pressure	Ambient

Table 3
Summary of the measurements and calculated cross leak rates at different operating conditions. The cathode inlet humidity was constant 0.08%.

	Flow rate/ml min^{-1}			Measured quantity	Calculated cross leak/ml min^{-1}
	H_2	N_2	Air		
Before reduction	0	4500	4500	0.18% O_2 (anode out)	8 ± 2 (O_2)
Purge gas	500	8500	8500	0.20% H_2O (cathode out)	10 ± 2 (H_2)
Nominal	9000	8500	50,000	0.20% H_2O (cathode out)	60 ± 12 (H_2)

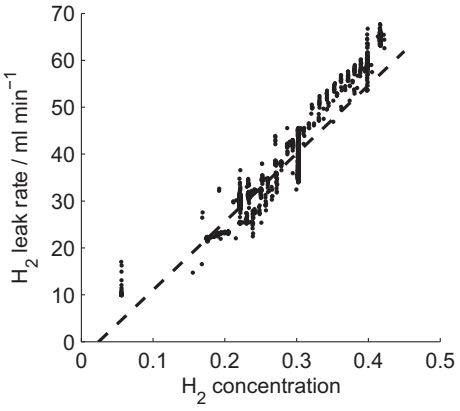

Fig. 7. Hydrogen cross leak as a function of average hydrogen concentration between anode inlet and outlet.

4. Conclusions

A coating method to deposit thin glass layers on compressible sealing materials was developed. Thermiculite 866 seals were coated with glass powder in organic carrier and were subsequently heat treated. The glass coating was conformable filling the surface imperfections of the Themiculite 866 core and the adjacent components effectively blocking interfacial leak paths. The coated Thermiculite 866 seals showed leak rates of 0.1–0.3 ml (m min)$^{-1}$, which is a reduction of 60–90% compared to uncoated samples which showed leak rates of 0.3–3 ml (m min)$^{-1}$. Leak rates of the coated seals as a function of overpressure were measured to be almost constant but very much dependent on the hydrogen concentration indicating that the coating effectively blocked the interfacial leak paths. The effect of gas composition to the leak rate should be considered carefully when comparing leak test results between different literature sources, as it can vary greatly.

A 30-cell stack was manufactured and tested to verify the feasibility of the coated seals in stack conditions. At nominal operating conditions of 0.25 A cm^{-2}, 46% fuel utilization and 20% air utilization the stack had a total hydrogen cross leak of 60 ml min^{-1} corresponding to 0.7% of the inlet hydrogen flow rate which can be considered a very promising result for the first stack test using these seals.

Acknowledgements

Finnish Funding Agency for Technology and Innovation in Finland (TEKES) and Elcogen Oy are acknowledged for financial support. Kai Nurminen and Kari Koskela of VTT Technical Research Centre of Finland and Jorma Stick of SataHitsaus are acknowledged for helping out with the experimental part of the work.

References

[1] J.W. Fergus, J. Power Sources 147 (2005) 46–57.
[2] P. Lessing, J. Mater. Sci. 42 (2007) 3465–3476.
[3] K. Weil, J. Miner. Metals Mater. Soc. (2006) 37–44.
[4] A. Shyam, R. Trejo, D. McGlurg, A. Ladoucceur, M. Kirkham, X. Song, J. Howe, E. Lara-Curzio, J. Mater. Sci. 48 (2013) 5880–5898.
[5] Y.S. Chou, J.W. Stevenson, L.A. Chick, J. Power Sources 112 (2002) 130–136.
[6] Y.S. Chou, J.W. Stevenson, L.A. Chick, J. Am. Ceram. Soc. 86 (2003) 1003–1007.
[7] M. Bram, S. Reckers, P. Drinovac, J. Mönch, R.W. Steinbrech, H.P. Buchkremer, D. Stöver, J. Power Sources 138 (2004) 111–119.
[8] S.P. Simner, J.W. Stevenson, J. Power Sources 102 (2001) 310–316.
[9] M. Rautanen, O. Himanen, V. Saarinen, J. Kiviaho, Fuel Cells (2009) 753–759.
[10] O. Thomann, M. Pihlatie, M. Rautanen, O. Himanen, J. Lagerbom, T. Varis, T. Suhonen, J. Kiviaho, J. Therm. Spray Technol. 22 (2013) 631–639.
[11] Y.S. Chou, J.W. Stevenson, J. Power Sources 191 (2009) 384–389.
[12] Y.S. Chou, J.W. Stevenson, Ceram. Trans. 161 (2005) 69–78.
[13] Y.S. Chou, J.W. Stevenson, J. Power Sources 157 (2006) 260–270.
[14] Y.S. Chou, J.W. Stevenson, J. Power Sources 135 (2004) 72–78.
[15] Y.S. Chou, J.W. Stevenson, P. Singh, J. Power Sources 152 (2005) 168–174.
[16] J. Hoyes, S. Bond, Sealing Technol. (2007) 11–14.
[17] Y.S. Chou, E.C. Thomsen, R.T. Williams, J.-P. Choi, N.L. Canfield, J.F. Bonnett, J.W. Stevenson, A. Shyam, E. Lara-Curzio, J. Power Sources 196 (2011) 2709–2716.

PUBLICATION VI

Post-experimental analysis of a solid oxide fuel cell stack using hybrid seals

Journal of Power Sources 2015,
Vol. 274, pp. 1009–1015.

Journal of Power Sources 274 (2015) 1009–1015

Contents lists available at ScienceDirect

Journal of Power Sources

journal homepage: www.elsevier.com/locate/jpowsour

Post-experimental analysis of a solid oxide fuel cell stack using hybrid seals

O. Thomann*, M. Rautanen, O. Himanen, J. Tallgren, J. Kiviaho

VTT Technical Research Centre of Finland, P.O. Box 1000, Biologinkuja 5, Espoo, FI-02044 VTT, Finland

HIGHLIGHTS

- Post-experimental analysis of a SOFC stack after 1800 h of operation.
- Microstructural analysis of the glass-coated hybrid seal.
- Materials interactions between glass-coated seals and Crofer 22 APU interconnects.
- Dual exposure of 0.2 mm thin Crofer 22 APU plates in stack operating conditions.

ARTICLE INFO

Article history:
Received 28 July 2014
Received in revised form
8 October 2014
Accepted 16 October 2014
Available online 23 October 2014

Keywords:
SOFC
Seal
Thermiculite 866
Dual exposure
Interconnect
Post-experimental analysis

ABSTRACT

A post-experimental analysis of a SOFC stack is presented. The stack was operated for 1800 h at 700 °C with air and hydrogen and contained hybrid glass-Thermiculite 866 seals. The goal of this work was to investigate the sealing microstructure and possible corrosion during mid-term operation. It was found that hybrid seals could effectively compensate for manufacturing tolerances of cells and other components due to the compliance of the glass layer. Additionally, different interfaces were investigated for corrosion. Corrosion was not observed at two-phase interfaces such as Crofer 22 APU/glass, glass/electrolyte and glass/Thermiculite 866. The three-phase interface between Crofer 22 APU/glass/hydrogen exhibited no corrosion. Some evidence of non-systematic corrosion was found at the Crofer 22 APU/glass/air interface. The possible reasons for the corrosion are discussed. Lastly, dual exposure to humid hydrogen and air of the 0.2 mm Crofer 22 APU interconnect had no detrimental effect on the corrosion compared to air exposure. Overall the hybrid seals used in combination with the thin interconnects were found to be a promising solution due to the low leak rate and limited material interactions.

1. Introduction

Currently, key challenges for successful commercialization of SOFC are to extend their lifetime and to reduce their cost. To achieve that, effective sealing solutions that address all the seals requirements are paramount [1,2]. Seals need to withstand simultaneous exposure to the air side and to the fuel side at temperature between 650 and 850 °C. In addition, they should withstand hundreds to thousands of thermal cycles for stationary and mobile applications respectively. Additionally, seal materials should be chemically compatible with the adjacent components like metallic interconnects and cell materials. Their electrical resistivity should also be high and stable. Lastly, the seals should also be inexpensive, easy to assemble and have to compensate for manufacturing tolerances of the other stack components. Presently, glass ceramic seals are widely used in SOFC stacks. Because they are rigidly bonded to the adjacent surfaces, their coefficient of thermal expansion needs to match closely the one of the neighbouring components. They exhibit very low leak rates [3] but can be prone to degradation with thermal cycling [4]. Compressible seals composed of mica-type paper have been investigated as an alternative [5–7]. The drawback of compressive seals is that in order to achieve acceptable leak rate, a compression stress of the order of several MPa has to be applied on the stack [5]. However, it was found that the leak rate remains significantly higher compared to glass ceramic seals and that the needed level of compression and the necessary compression system becomes technically challenging for large footprint stack. These inherent issues can be addressed by adding compliant layers of glass or metal on both sides of a compressible seal [3,8,9]. The compliant layers block the main leak

* Corresponding author. Tel.: +358 401247497.
E-mail address: olivier.thomann@vtt.fi (O. Thomann).

http://dx.doi.org/10.1016/j.jpowsour.2014.10.100
0378-7753/

path between the seal and the interconnects which leads to a leakage reduction of up to 90% [9]. Additionally, Rautanen et al. showed that a compression stress as low as 0.1 MPa can be used with hybrid seals [9].

Sealing material interaction studies have been previously published but most of the articles have been focusing on glass ceramic seals interaction. Batfalsky et al. performed post-experimental investigation on stacks that had undergone rapid performance degradation [10]. They found that the interconnects had so severely corroded in the vicinity of the glass ceramic seals that the corrosion product had formed electrical bridges between adjacent interconnects and caused short-circuiting after 200 h at 800 °C. They attributed the accelerated corrosion to the presence of PbO in the glass. Menzler et al. presented results of post-experimental investigation of a stack operated for 6400 h at 800 °C [11]. They showed that the corrosion of the interconnects was enhanced in the vicinity of the glass ceramic seals but that the extent of corrosion did not compromise the performance of the stack. Wiener et al. studied interactions between Thermiculite 866 materials (a composite of vermiculite and steatite [12]) and Crofer 22 APU at 800 °C in ex situ experiments [13]. They found that the Crofer 22 APU underwent accelerated corrosion and this was attributed to the decomposition of steatite at 800 °C and transport of Mg to the oxide layer. Bram et al. studied interaction of Thermiculite 866 with Crofer 22 APU in Ref. [14]. They found that the break-away corrosion of Crofer 22 APU took place at temperature as low as 600 °C in ex situ test. They attributed the accelerated corrosion due to the steam emitted by the Thermiculite 866 during heat-up. They found that such a corrosion reaction could be prevented by a pre-oxidation treatment of the interconnects. Interestingly, corrosion was most often found at the three-phase boundary between seal material, interconnect and gas (air or fuel) [10,11,13,14]. Only few material interactions studies have been published on hybrid seals. Chou et al. studied long-term interaction of hybrid seal materials in ex situ experiments [15]. They found that the phlogopite paper was reacting with the glass they used after 500 h at 800 °C, which compromised the performance of the seal during thermal cycling. Interactions between seal materials and ferritic stainless steel were not discussed in that paper. Chou et al. published the results of a post-experimental analysis of a 3-cell stack using hybrid seals operated at 800 °C [16]. They concluded that material interaction was limited and that their material selection for the seal and interconnect material was suitable for long-term operation. However, the three-phase interfaces between seal/interconnect/gases were not discussed.

Dual atmosphere exposure of interconnects has also drawn some attention in the literature. Skilbred et al. and Yang et al. studied the effect of dual atmosphere exposure at 800 and 850 °C on the corrosion of Fe–Cr–Mn steels and they showed that dual exposure affects the oxide scale composition with a higher concentration of Fe in the oxide scale on the air side. Exposure time was limited to 500 h and 300 h [17–19]. Holcomb et al. studied dual exposure of the austenitic steel 316L and found that heavy corrosion was taking place after 100 h at 700 °C. It was caused by the diffusion of oxygen and hydrogen in the alloy and the formation of steam in the metal alloy near the oxide layer, which formed a thick and porous oxide layer [20].

The amount of data available on dual exposure of interconnect steels is presently limited, which is partly explained by the fact that dual exposure tests are more complex than single atmosphere exposure tests. Additionally, the durations of the experiments are typically in the few hundred hours range. The hydrogen atmosphere is often lean with 5% hydrogen in argon for safety reason and the humidity restricted to 3%, whereas these values are typically higher inside a stack.

The thickness of the interconnects is also affecting their lifetime by decreasing the initial reservoir of Cr. Stainless steel alloys are protected from excessive corrosion by the formation of a Cr oxide layer. During operation, the Cr from the protective scale evaporates and is replaced by Cr diffusing from the bulk of the alloy. The Cr is consumed until it reaches a concentration of about 16% in the alloy, when break-away oxidation start to occur [21]. On the one hand, it is interesting to reduce interconnect thickness to reduce the cost associated with the interconnect steel, but on the other hand Asensio-Jimenez et al. showed that the corrosion rate of interconnect steel increases for thinner plate thickness [22]. Therefore data on the corrosion of thin interconnect are valuable.

This present paper contributes to the field with the results of the post-experimental analysis of a SOFC stack using hybrid seal consisting of a Thermiculite 866 compressible core with compliant glass layers. The seal cross-section has been extracted from a single-cell stack that was operated for 1800 h at 700 °C. The in situ nature of the experiment provides exposure conditions to the seals and interconnects that are closer to stack operation compared to ex situ experiments. For example, the steam content in this work was 20% at anode outlet, which is higher compared to ex situ seals (usually maximum 3%). However, even higher steam content is expected in a stack in an actual system environment (from 60 to 80% steam content).

The goals of the post-experimental analysis were: i) to investigate the microstructure of the hybrid seals, ii) to evaluate material interactions between the seal materials and the interconnects and iii) to investigate the effect of dual exposure on thin 0.2 mm interconnects. The stack presented here is a stack prototype developed at VTT Technical Research Centre of Finland in which hybrid seals were used. After this work, the hybrid seal design has been significantly improved by a 10-fold reduction of the amount of glass and the cost associated to it [9].

2. Experimental

The single cell stack used a co-flow configuration. Crofer 22 APU (ThyssenKrupp, Germany) was used for interconnects and end-plates. The interconnects were 0.2 mm in thickness. The anode-supported cell was manufactured by Elcogen AS (Estonia) and is 10×10 cm^2. Hybrid seals were used for all seals located between Crofer 22 APU plates and are made with consolidated Thermiculite 866 (Flexitallic LTd, the United-Kingdom) [12] between two glass tapes of 220 μm green thickness. The glass used belongs to the system MO (M = Mg, Ca)–Al_2O_3–BaO– SiO_2–B_2O_3 (GM31107, Schott, Germany [23]). The Thermiculite 866 is composed in nearly equal amount of vermiculite and steatite, which compositions are $[(K, Mg, Fe)_3(Si,Al)_4O_{10}(OH)_2]$ and $[(Mg_3Si_4(OH)_2]$ respectively. The seal between the cell electrolyte (yttria-stabilized zirconia (YSZ)) and Crofer 22 APU plate was made of glass without Thermiculite 866. 40 kg of weight was added on the stack, which corresponds to a compressive stress of ca. 0.1 MPa assuming that all the weight was carried by the seals and not by the cell.

Dry hydrogen and dry air were used as fuel and oxidant. Pure hydrogen was selected as fuel, which exposes the seals to a worst case condition as it has been shown that the leak rate through hybrid seal increases with the concentration of hydrogen [9]. The stack was operated at 700 °C for 1800 h. Average current density was 0.2 Acm^{-2} and fuel utilisation and air utilisation were 18%. The hydrogen cross leak value corresponded to a loss of 0.9% of the inlet hydrogen flow in these operating conditions, which is low. The cross leak value was calculated according to the method described in Ref. [9].

After the test, the stack was mounted in epoxy and a cross-section was extracted from the area close to the gas outlet for

SEM and EDS analysis. This area was selected because the exposure conditions are expected to be the most challenging due to the increased steam content.

Post-experimental analysis was carried out using SEM observation and energy-dispersive x-ray spectroscopy (EDS) on JSM-6400 Scanning Microscope from JEOL equipped with a Prism 2000 detector and Spirit 1.06.02 Analyzer software from Princeton Gamma-Tech (PGT). The oxide layer thickness was determined by measuring the area on the image corresponding to the oxide phase with ImageJ [24] and dividing it by the picture width according to the method described in Ref. [25].

3. Results and discussion

3.1. Glass compliance

A cross-section of two hybrid seals is illustrated in Fig. 1. It can be seen that the Thermiculite 866 material is significantly deformed by the die-cutting process forming protruding cutting burrs near the edges. Despite the unevenness of the Thermiculite 866, the glass has well accommodated the gap varying between 15 and 150 μm for the upper seal shown in Fig. 1. Pore formation took place only at the location were the Thermiculite 866 is at its thinnest, however these pores are closed and don't form a continuous leak path. Additionally, some excess glass was extruded out of the seal because of the compliance of the glass. This means that the glass tape thickness could be thinner or other methods to apply thinner glass coating could be used. Moreover, the clearances between the Crofer 22 APU plates are 710 and 580 μm at the location of measurement for the two seals shown and this difference in clearance didn't seem to have decreased the quality of the seals at these locations. This demonstrates the benefit of using hybrid seals over purely compressible seals. In short, similar hybrid seals were able to effectively seal gaps between 580 and 710 μm and the glass layer was able to compensate 140 μm thickness variation of the Thermiculite 866. Compressible seals would have required much larger compression stress to flatten the cutting burrs. Additionally, the gap clearance variation would have likely been an issue due to the limited compressibility of Thermiculite 866 [5]. There are many reasons that can lead to a variation of gap clearance in a stack, i.e. differences in cell and interconnect plate thickness, and variation of thickness of the compressible Thermiculite 866. These variations can be decreased to a certain level by more uniform manufacturing methods but cannot be totally avoided. Moreover, generally decreasing the manufacturing tolerance comes with a cost increase. It is therefore of high interest that the seals can accommodate the geometric variation in a stack.

3.2. Materials interactions between seal materials and interconnects

This section presents results of different material interactions, such as Crofer/glass, glass/Thermiculite 866 and glass/electrolyte interfaces. In addition, interactions at the three-phase interfaces such as Crofer/glass/air and Crofer/glass/hydrogen are detailed.

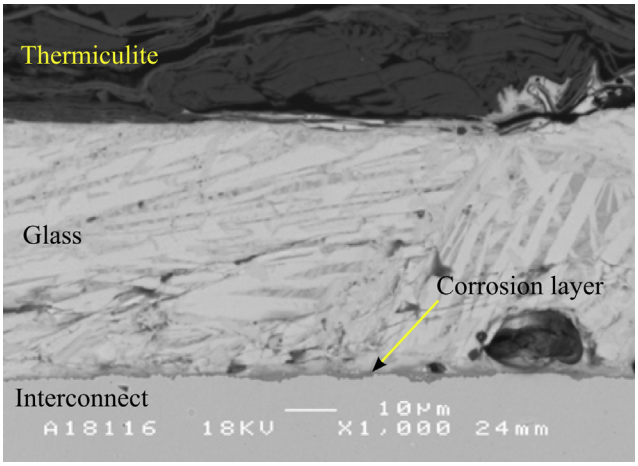

Fig. 2. SEM BSE cross-section of Crofer/glass and glass/Thermiculite 866 interfaces.

3.2.1. Crofer/glass and glass/Thermiculite 866 interfaces

The Crofer/glass and glass/Thermiculite 866 interfaces are illustrated in Fig. 2. This picture has been taken from the middle section of the seal, which means that its exposure to gas is limited to possible leakage through the seal. It appears that the materials have good chemical compatibility and only limited corrosion can be seen between glass and Crofer 22 APU with an oxide layer of less than 1 μm. As a comparison, the oxide layer thickness is thinner in contact with the glass compared to the case when the Crofer 22 APU is exposed to air at the same temperature (see results in Section 3.3). Therefore, it was concluded that the presence of glass did not accelerate the oxidation of the Crofer 22 APU plate at this interface.

3.2.2. Crofer/glass/air interface

Cross-section pictures from the Crofer/glass/air interface are illustrated in Fig. 3 and Fig. 4. The cross-section sample is taken near the air exhaust. The humidity in air downstream of the stack was measured to be ca. 0.4% during stack operation. The cracks present in the glass are due to sample preparation.

The location shown in Fig. 3(a) and (b) corresponds to the upper and lower corners of the seal which is exposed to the same cathode atmosphere, and they are therefore exposed to the same air atmosphere. However, their corrosion behaviour differed significantly. The upper side shows no sign of significant corrosion while the lower side has developed a 20 μm corrosion layer just at the location where the glass layer ends. The corrosion layer does not extend more than 200 μm from the three-phase interface. As it can be seen from the EDS analysis in Fig. 3(d), the oxide layer consists of a first layer of mixed oxide of Cr and

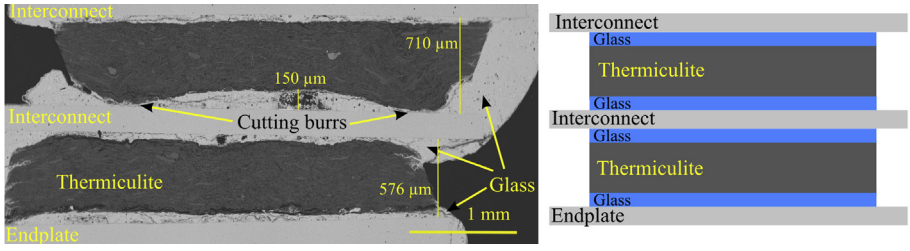

Fig. 1. SEM BSE cross-section of two frame seals. The seals are composed of a Thermiculite 866 core between two glass layers.

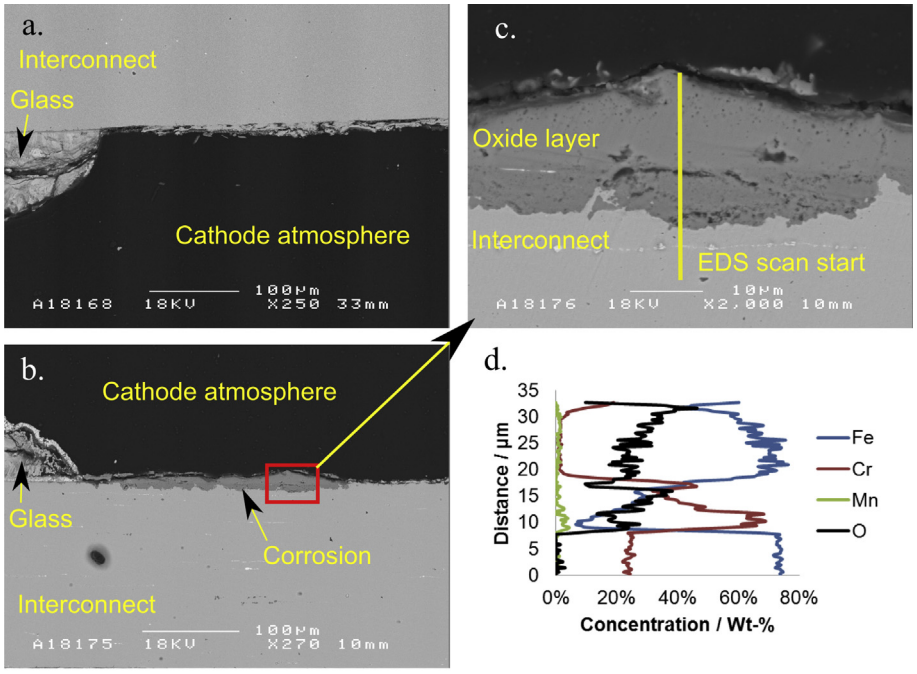

Fig. 3. SEM BSE cross-sections of two Crofer/glass/air interfaces (a and b) that are both exposed to cathode atmosphere. Magnified view of cross-section (c).

Mn and the top layer is mainly composed of Fe oxide. This is a clear example of break-away oxidation, i.e. when the Cr oxide layer cannot anymore protect the stainless steel because of too fast corrosion. It is however surprising that such extent of corrosion takes place only at one corner of the seal (Fig. 3(b)) and not at the other (Fig. 3(a)), despite the exposure condition being identical.

Similarly, pictures shown in Fig. 4(a and b) correspond to two different seals but exposed to the same atmosphere; the air exhaust manifold. Also in this case, no significant corrosion takes place at one side (Fig. 4(a)) and break-away oxidation took place at the other side (Fig. 4(b)), where the oxide layer is 20 µm thick. Accelerated corrosion was found to extend millimetres away from the seals into the air manifold towards the stack air outlet. The oxide layer was thicker 5 mm away from the seal, where it was about 120 µm thick and its top layer was composed mainly of Fe oxide (picture not shown). However, corrosion in the manifold of the thick end plate is not critical for the stack performance.

Different reasons can have caused the Crofer 22 APU to undergo break-away oxidation at some locations. Cr evaporation from the oxide layer is enhanced by the presence of water vapour in air [26,27] and if the evaporation rate of Cr is higher than the rate at which the Cr oxide layer is formed, the stainless steel undergoes break-away oxidation. It is possible that the steam content was locally higher where the break-away oxidation took place. Steam content can be locally higher in case there is a local leak of hydrogen. However this does not appear to be the case here because the seals shown in Figs. 3 and 4 are exposed to air on both sides. The heavy corrosion found deep in the air manifold could be attributed to the presence of contamination from lubricant used during machining of the manifolds. The endplates were heat-treated after machining (800 °C for 12 h) during which possible lubricant was burned, then the plates were polished and then cleaned in laboratory glassware washer and by wiping with ethanol impregnated tissues before use but it is difficult to remove lubricant or burned lubricant residues from the narrow manifolds. This hypothesis is supported by the fact that the heaviest corrosion was found deep in the manifold, several millimetres away from the seal. Lastly, it cannot be excluded that the corrosion could be caused by element evaporating from the glass or Thermiculite 866. Both are made of complex elemental formulations and have potentially many candidates for evaporation and subsequent interactions.

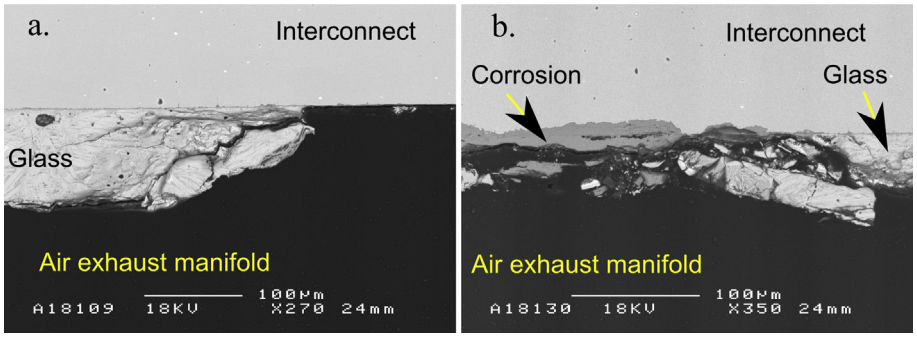

Fig. 4. SEM BSE cross-sections of two Crofer/glass/air interfaces (a and b) that are both exposed to the atmosphere of the air exhaust manifold.

However, if the corrosion mechanism would be from material interaction, one would expect it to happen systematically, which is not the case here.

Bram et al. found similar corrosion behaviour of Crofer 22 APU in their paper on material interactions between Thermiculite 866 and Crofer 22 APU [14]. In their work, they exposed Thermiculite 866 (without any glass) to air and dual atmosphere at 600 °C for 400 h and found that break-away oxidation was taking place at the air side. They attributed the corrosion behaviour of the Crofer 22 APU to the enhanced water concentration near the seal that was originating from vermiculite dehydration and steatite decomposition. This phenomenon was previously described and quantified by Wiener et al. [13]. According to Bram et al., the break-away oxidation behaviour can be suppressed by pre-oxidation of the interconnect plates.

The reason for the accelerated corrosion at the air side remains unclear and is the subject of further research. The main risk associated with the accelerated corrosion found near the seals is the formation of porous Fe oxide all the way through the 0.2 mm thin interconnects and creation of a leak path through the interconnect. Secondarily, in extreme case, accelerated corrosion can form a lump of electrically conductive Fe oxide and creates short-circuiting by connecting adjacent interconnect plates [10]. However, it appears that the corrosion is limited after 1800 h and didn't spread far towards the cathode, therefore it is unlikely that the growth of the oxide layer would affect the area-specific resistance of the interconnect. The most corroded locations were found in the air exhaust manifold on the 2 cm-thick end plate where accelerated corrosion has no consequence for the stack performance. Lastly, it is interesting to notice that corrosion took place near the three-phase boundary and not at the glass/metal (two-phase) interface, which is coherent with findings of several previous studies [10,11,13,14]. As mentioned, dry air was used during the test. In order to subject the materials on the cathode side to a more challenging atmosphere, pre-humidified air (e.g. 1 … 3%) could be used to see the effect of humid air on material corrosion.

3.2.3. Crofer/glass/humid hydrogen interface

A micrograph from the Crofer/glass/humid hydrogen interface is shown in Fig. 5. No significant material interaction could be seen at the interface between seal and humid hydrogen. The humidity of the fuel is also at its highest at this location, about 20%, due to water production from reaction at anode. The cracks in the glass are due to sample preparation.

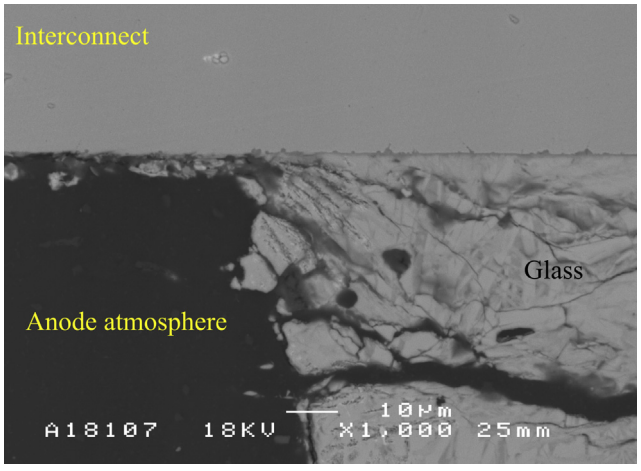

Fig. 5. SEM BSE cross-section at the Crofer/glass/humid hydrogen interface. The visible glass is part of the cell seal which is composed of glass without any Thermiculite 866.

3.2.4. Glass/electrolyte interface

The glass/electrolyte interface is illustrated in Fig. 6. The glass contains little porosity and exhibits a good adherence to the YSZ of the electrolyte. There is no evidence of corrosion between the electrolyte and the glass.

3.3. Corrosion of interconnects exposed to dual atmosphere

The post-experimental analysis of this stack also offers valuable insight into the corrosion of thin interconnects in dual atmosphere compared to exposure to single air atmosphere.

Fig. 7(a and b) show cross-sections from the interconnect plate exposed simultaneously to air and humid hydrogen. The location is near the fuel exhaust and the absolute humidity in the fuel atmosphere was about 20%. Fig. 7(c and d) show cross-sections from an interconnect exposed to air atmosphere on both side. On Fig. 7(a), a crack from sample preparation is present in the oxide layer, splitting it into two layers.

For the single air exposure case shown in Fig. 7(c and d), the oxide layers were 1.4 µm and 1.9 µm in thickness. In case of dual exposure, the oxide layers were found to be of 1.3 µm and 1.2 µm in thickness (Fig. 7(a and b)). The EDS scans suggest that the oxide layer formed in dual exposure is rich in Cr and Mn oxide at both sides. The morphology of the oxide layer depends on the conditions of exposure with a tendency for the oxide layer formed in air to be smoother than the one formed in fuel atmosphere. It was previously shown in the literature that the spinel crystals growing on the surface of ferritic Fe–Cr–Mn steel were dependant on the atmosphere composition [28]. Some limited inwards growth of surface oxide can be seen in Fig. 7(a, b and c) but limited to a depth of 5 µm from the metal surface. It is difficult to find comparable oxide layer thickness data from the literature due to the numerous conditions to be taken into account (temperature, time and atmosphere composition). Linder et al. found that Crofer 22 APU oxide layer thickness was about 5 µm for similar exposure time at 850 °C in air [25]. Sachitanand et al. found that Crofer 22 APU oxide layer thickness was about 12–16 µm at 850 °C in humidified air after 1000 h [29].

The results presented in Fig. 7 lead to three main findings. Firstly, the oxide layers are thin for interconnect without protective coating, showing that the selected interconnect alloy exhibits suitable corrosion-resistance at an operating temperature of 700 °C. Additionally, dual exposure had no detrimental effect on the corrosion rate of the interconnect and the oxide layers were actually thinner in the dual exposure case compared to exposure to air only. Lastly, the interconnect thickness used for this stack (0.2 mm) is relatively thin and therefore the reservoir of Cr in the bulk steel is limited. However, it appears that the low thickness of the interconnects had no significant detrimental effect on their corrosion rate.

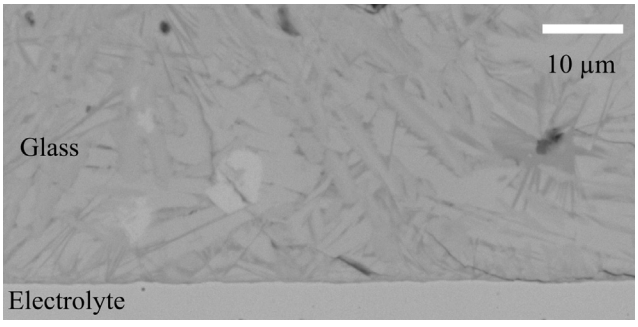

Fig. 6. SEM BSE cross-section at the interface between glass and electrolyte.

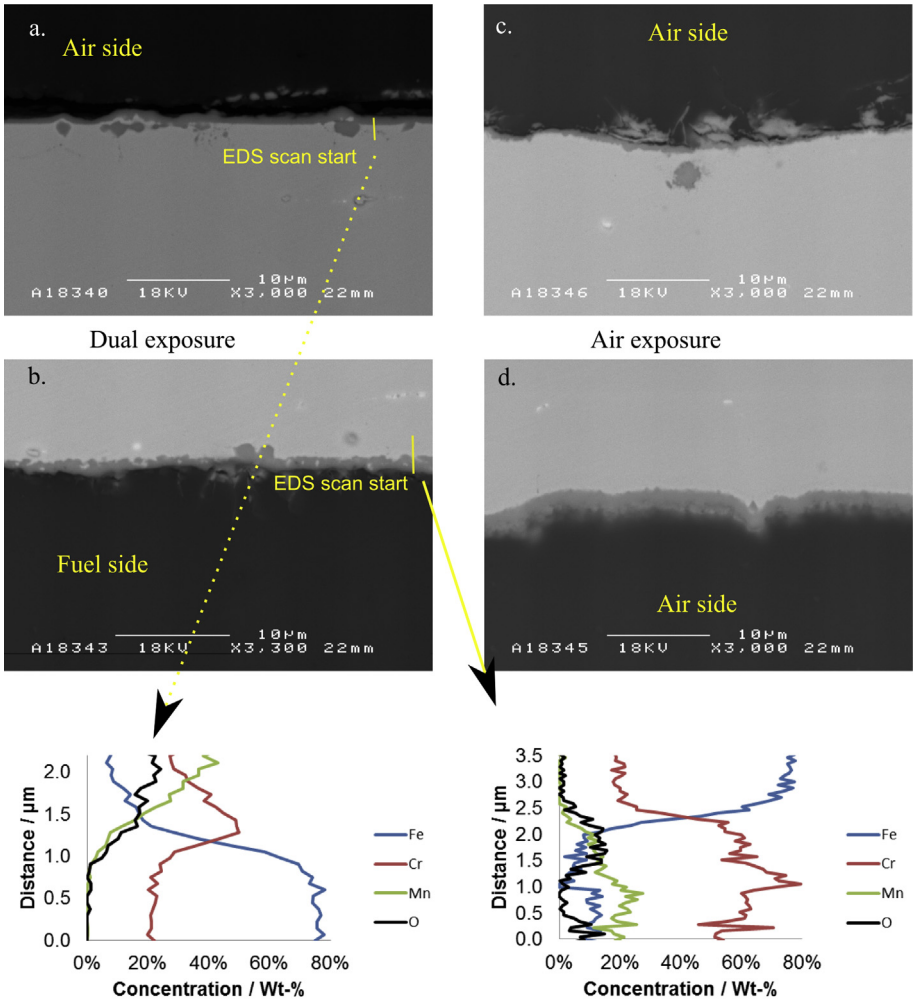

Fig. 7. SEM BSE cross-sections of a 0.2 mm thin interconnect plate exposed simultaneously to air and humid hydrogen (a and b) with two EDS scan. Another interconnect exposed to air on both side (c and d).

4. Conclusions

In this article, post-experimental analysis results of a single-cell stack containing hybrid seals are detailed. The hybrid seal solution was found to work well because it could successfully compensate for thickness variation of stack element of about 150 µm. In addition, the compliant glass layer could well accommodate the unevenness of the Thermiculite 866 caused by the die-cutting process. The hydrogen cross leak value corresponded to a loss of 0.9% of the inlet hydrogen flow, which is very low. Different interfaces and locations inside the stack were investigated for corrosion. Corrosion didn't take place at two-phase interfaces such as Crofer/glass, glass/electrolyte and glass/Thermiculite 866. The three-phase interface between Crofer/glass/hydrogen exhibited no corrosion, whereas some of the locations corresponding to the Crofer/glass/air interface exhibited some non-systematic corrosion. The possible reasons for the corrosion found were discussed and the most likely reason for corrosion is contamination from lubricant that was not properly removed before stack assembly. These results will be the basis of a future study on the corrosion of Crofer 22 APU in contact with sealing materials ex situ, which will aim at improving our understanding of this phenomenon. Lastly, dual exposure of thin Crofer 22 APU interconnect did not cause enhanced corrosion compared to air exposure and the oxide layer thickness was found to be limited below 2 µm. Overall the hybrid seals used in combination with the thin interconnects were found to be a promising solution due to low leak rate and its suitability for long-term operation will be examined further in stack operated for longer period of time.

Acknowledgements

Finnish Funding Agency for Technology and Innovation (TEKES) is acknowledged for financial support. Seija Kivi from VTT is acknowledged for sample preparation, Kai Nurminen, Kari Koskela from VTT and Jorma Stick from SataHitsaus are acknowledged for the experimental part of the work. Risto Parikka from VTT Expert Services Oy is acknowledged for SEM analysis.

References

[1] J.W. Fergus, J. Power Sources 147 (2005) 46–57.
[2] K. Weil, JOM 58 (2006) 37–44.
[3] Y.-S. Chou, J.W. Stevenson, L.A. Chick, J. Power Sources 112 (2002) 130–136.
[4] R.N. Singh, Int. J. Appl. Ceram. Technol. 4 (2007) 134–144.
[5] M. Rautanen, O. Himanen, V. Saarinen, J. Kiviaho, Fuel Cells 9 (2009) 753–759.

[6] Z. Wuillemin, N. Autissier, M. Nakajo, M. Luong, J. Van Herle, D. Favrat, J. Fuel Cell Sci. Technol. 5 (2008).
[7] S.P. Simner, J.W. Stevenson, J. Power Sources 102 (2001) 310–316.
[8] Y.-S. Chou, J.W. Stevenson, L.A. Chick, J. Am. Ceram. Soc. 86 (2003) 1003–1007.
[9] M. Rautanen, O. Thomann, O. Himanen, J. Tallgren, J. Kiviaho, J. Power Sources 247 (2014) 243–248.
[10] P. Batfalsky, V.A.C. Haanappel, J. Malzbender, N.H. Menzler, V. Shemet, I.C. Vinke, R.W. Steinbrech, J. Power Sources 155 (2006) 128–137.
[11] N.H. Menzler, P. Batfalsky, L. Blum, M. Bram, S.M. Groß, V.A.C. Haanappel, J. Malzbender, V. Shemet, R.W. Steinbrech, I. Vinke, Fuel Cells 7 (2007) 356–363.
[12] J.R. Hoyes, S. Bond, Sealing Technol. (2007) 11–14.
[13] F. Wiener, M. Bram, H. Buchkremer, D. Sebold, J. Mater. Sci. 42 (2007) 2643–2651.
[14] M. Bram, L. Niewolak, N. Shah, D. Sebold, H.P. Buchkremer, J. Power Sources 196 (2011) 5889–5896.
[15] Y.-S. Chou, J.W. Stevenson, J. Hardy, P. Singh, J. Power Sources 157 (2006) 260–270.
[16] Y.-S. Chou, J.W. Stevenson, J.-P. Choi, J. Power Sources 250 (2014) 166–173.
[17] Z. Yang, G. Xia, M.S. Walker, C. Wang, J.W. Stevenson, P. Singh, Int. J. Hydrogen Energy 32 (2007) 3770–3777.
[18] B. Skilbred, A. Werner, H. Reidar, Int. J. Hydrogen Energy 37 (2012) 8095–8101.
[19] Z. Yang, M.S. Walker, P. Singh, J.W. Stevenson, T. Norby, J. Electrochem.Soc. 151 (2004).
[20] G.R. Holcomb, M. Ziomek-Horoz, S.D. Cramer, B.S. Covino Jr., S.J. Bullard, J. Mater. Eng. Perform. 15 (2006) 404–409.
[21] P. Huczkowski, V. Shemet, J. Piron-Abellan, L. Singheiser, W.J. Quadakkers, N. Christiansen, Mater. Corros. 55 (2004) 825–830.
[22] C. Asensio-Jimenez, L. Niewolak, H. Hattendorf, B. Kuhn, P. Huczkowski, L. Singheiser, W.J. Quadakkers, Oxid. Met. 79 (2013) 15–28.
[23] D. Goedeke, J. Besinger, Y. Pfluegler, B. Ruedinger, ECS Trans. 25 (2009) 1483.
[24] M.D. Abràmoff, P.J. Magalhães, S.J. Ram, Biophoton. Int. 11 (2004) 36–42.
[25] M. Linder, T. Hocker, L. Holzer, K.A. Friedrich, B. Iwanschitz, A. Mai, J.A. Schuler, J. Power Sources 243 (2013) 508–518.
[26] C. Gindorf, L. Singheiser, K. Hilpert, J. Phys. Chem. Solids 66 (2005) 384–387.
[27] O. Thomann, M. Pihlatie, J.A. Schuler, O. Himanen, J. Kiviaho, Electrochem. Solid State Lett. 15 (2012) B35–B37.
[28] Z. Yang, J.S. Hardy, M.S. Walker, G. Xia, S.P. Simner, J.W. Stevenson, J.Electrochem.Soc. 151 (2004) A1825–A1831.
[29] R. Sachitanand, M. Sattari, J. Svensson, J. Froitzheim, Int. J. Hydrogen Energy 38 (2013) 15328–15334.

Series title and number

VTT Science 112

Title	**Improved durability and reduced system complexity of solid oxide fuel cell systems**
Author(s)	Olivier Thomann
Abstract	Solid oxide fuel cells (SOFCs) show great potential for clean and efficient power generation applications. However, their high cost is preventing their market entry. This dissertation focuses on solutions to increase the durability of SOFCs and to reduce the complexity of SOFC systems to drive their cost down. Chromium poisoning of the cathode is a major issue limiting the durability of SOFCs. This issue is addressed by the development of a protective manganese-cobalt spinel coating for steel interconnects. Coated interconnects were characterised in SOFC relevant conditions and the results showed that the coating fulfilled its main requirements, which are: limitation of chromium transport from the interconnect to the cathode, protection against oxidation of the steel and low and stable area-specific resistance. Evidence was found that another source of chromium is the balance-of-plant (BoP) components upstream of the cathode, an issue which did not receive much attention in the literature. Therefore, a method for measuring chromium evaporation from BoP components was developed and validated on a stainless steel pipe. SOFC systems based on natural gas commonly include a fuel processing subsystem for fuel steam reforming. The need for an external water source can be eliminating by recycling the steam-rich anode off-gas. Investigations were performed on a pre-reformer with a precious metal catalyst and it was found that adding an anode off-gas recycling loop had no detrimental effect on the activity of the catalyst and carbon formation could be avoided. Additionally, results showed the possibility to generate the hydrogen-containing gas needed to prevent the reoxidation of the anode catalyst during heat-up phase. The results permitted the implementation of an anode off-gas recycling loop in a 10 kW SOFC system. Additionally, the system was heated up without supplying any premixed hydrogen-containing gas, which enables to reduce the complexity of the system. Finally, the durability of a stack can be improved by seal solutions with limited material interactions. A hybrid seal solution was developed by coating a compressible core with glass layers. The developed seal reduced the leak rate compared to a purely compressible seal. Material interactions were studied with a post-experimental investigation of an SOFC stack. Interactions were limited with the exception of evidence of increased oxidation at the steel/seal/air interface. Overall, the solution was found to be promising and the obtained results led to the commercialisation of the developed seal solution by Flexitallic Ltd (UK).
ISBN, ISSN, URN	ISBN 978-951-38-8360-7 (Soft back ed.) ISBN 978-951-38-8361-4 (URL: http://www.vttresearch.com/impact/publications) ISSN-L 2242-119X ISSN 2242-119X (Print) ISSN 2242-1203 (Online) http://urn.fi/URN:ISBN:978-951-38-8361-4
Date	December 2015
Language	English
Pages	85 p. + app. 57 p.
Name of the project	
Commissioned by	
Keywords	Fuel cells, SOFC, chromium poisoning, anode off-gas recycling, system heat-up, seal, interconnect, material interactions
Publisher	VTT Technical Research Centre of Finland Ltd P.O. Box 1000, FI-02044 VTT, Finland, Tel. 020 722 111

Improved durability and reduced system complexity of solid oxide fuel cell systems

Solid oxide fuel cells (SOFCs) are electrochemical devices that produce electricity (and heat) from fuel and air. They are expected to play an important role in the power generation sector due to their advantages in terms of high electrical efficiency, modularity, fuel flexibility and very low emissions. However, their high cost remains a burden, delaying their market entry. In order to drive their cost down, their durability must be improved and the system complexity needs to be reduced. This dissertation addresses these challenges through the development of solutions to reduce the degradation of SOFCs because of chromium poisoning of the cathode. In addition, simplification of the fuel processing subsystem are investigated and demonstrated. Lastly, performant and durable sealing solutions were developed and tested in an operating SOFC stack.

ISBN 978-951-38-8360-7 (Soft back ed.)
ISBN 978-951-38-8361-4 (URL: http://www.vttresearch.com/impact/publications)
ISSN-L 2242-119X
ISSN 2242-119X (Print)
ISSN 2242-1203 (Online)
http://urn.fi/URN:ISBN:978-951-38-8361-4